

# Developing and Characterizing Novel Atom Interferometer Gyroscopes for Applications in Inertial Navigation

Marybeth Morris Beydler

Houston, Texas

BA Liberal Arts, St. John's College, 2017

*A Dissertation presented to the Graduate Faculty of the University of Virginia  
in Candidacy for the degree of Doctor of Philosophy*

Department of Physics

UNIVERSITY OF VIRGINIA

May 2024



*“Alright team, it’s the fourth quarter. The Lord gave us the atoms, and it’s up to us to make them dance.”*

Homer J. Simpson

# *Abstract*

The Global Positioning System (GPS) reliably determines a unique position on the Earth's surface if the receiver can communicate with at least four satellites in orbit around the earth simultaneously. However, the entire system breaks if the weak signal from the distant satellite fails to travel in a straight line from the satellite to the receiver. Due to difficulties operating GPS in every environment and circumstance, civilian and defense applications also rely on traditional position-finding methods using Inertial Navigation Systems (INS) that are uninterruptible. An INS replaces external references with internally-determined acceleration and rotation measurements to compute a platform's change in position. Precise location determination depends on exquisite accuracy in the inertial sensors as sensor errors integrate over time. Currently, the rotation sensing component of high-performance INS use classical, light-based gyroscopes that rely upon Sagnac interferometry. While these sensors offer practical precision, they experience drift leading to large inaccuracies in calculations if denied GPS for long periods of time.

Sagnac atom interferometers are a promising technique for high-performance rotation sensing because atoms offer intrinsic stability and precision for measurements of inertial forces. The use of trapped atoms for the interferometer avoids the need for long free-fall distances that would be incompatible with a navigation apparatus. Rotation sensing with a dual Sagnac atom interferometer gyroscope was achieved in a previous experimental apparatus. The measurement cycle begins by producing a Bose-Einstein condensate (BEC) in a cylindrically harmonic trap. The BEC is then split and recombined by standing-wave Bragg laser pulses, with the magnetic trap guiding the atoms to enclose a circle. A feature of this method is the use of two counterpropagating interferometers to cancel common-mode noise that can mask the rotation signal.

This dissertation documents the construction and characterization of a new instrument with improved performance. In the new apparatus, a Sagnac area of  $8.2 \text{ mm}^2$  was achieved using multiple orbits of the BEC wave packets, giving a calculated sixteen-fold improvement in sensitivity over the previous work. The interferometer operation is sufficiently stable to operate for a day or longer continuously. The Allan deviation was measured over a 26-hour period, and exhibited favorable  $1/\sqrt{\tau}$  scaling over averaging times  $\tau$  up to  $10^4$  s. At  $10^4$  s, the resulting rotation sensitivity is  $7 \times 10^{-6}$  rad/s, or about 0.1 revolutions per day.

While this new instrument is an improvement on the previous iteration, it is still an impractical device for rotation sensing in INS due to its size and complexity. The design and evaluation of a compact instrument that uses a volume of only 50 liters for all optics, vacuum chamber and magnetic coils is also reported. This system features an atom chip that promises to speed up the measurement cycle by a factor of ten by decreasing the BEC preparation time. A MOT with around  $10^7$  atoms was produced in the compact instrument and new techniques were developed for its operation. In initial experiments, this system bottlenecked at the MOT stage. Potential solutions to this problem will be presented along with a discussion of improving the short term stability of the laboratory-sized apparatus.

# *Acknowledgements*

The work documented in this dissertation couldn't have been possible without the many people who inspired and supported me throughout the process of pursuing a doctorate. First, I would like to thank my advisor Cass Sackett. I wouldn't be the physicist or person I am today without his patience, mentoring, and kindness. I always felt valued and appreciated working for Cass and he has helped me foster a healthy optimism and greater patience which has made me a much more pleasant person to be around, both inside and outside of the lab.

I would also like to thank my labmates over the years, especially, Eddie Moan. Eddie is the best hands on teacher in the lab anyone could have and I owe nearly all of my AMO experimental skills to his effective teaching and mentoring. I am so fortunate to have worked with him longer than I expected to when I joined our lab. He is a great person that I am so proud to call my friend.

The majority of the work in this dissertation was funded through the DARPA Atom-Photonics Integration (A-PhI) program. As part of this grant, our lab partnered with several contractors I would like to acknowledge here: Eric Imhof (Northrop Grumman), Evan Salim (Cold Quanta, Inc/Inflection), Jim Stickney (Space Dynamics Laboratory), and Brian Kasch (Air Force Research Laboratory). Without their partnership, hard work, and dedication this project would not have been possible.

I would like to acknowledge all of the physicists who took a chance on me and believed in me. John Kelley and Albrecht Karle (UW-Madison); Charlie Mueller, Geoff Smith, and Kevin Lannon (Notre Dame); and Jimmy Proudfoot, Jessica Metcalfe, and Sergei Chekanov (Argonne National Lab). I would like to thank my research committee members over the years and my dissertation committee. Your comments and questions have helped my understanding greatly and made this document the best it could be.

I would also like to especially thank Chris Neu for bringing me to UVA, being my research advisor for the first couple of years, and being my bridge advisor for the rest of graduate school. This opportunity has meant the world to me and would not have happened had we not met at CERN many years ago.

Swing C'ville, UVA Swing Club (c. 2017), and RVA Swing deserve special acknowledgement. I am going to miss Wednesday nights at the Front Porch with the best community anyone could have in Charlottesville. Some specific mentions: Jim Hughes, Stephen Johnson, Emma Bramer, Dana Schroeder, Aurora Nichols, Katie Dell, Erica Vess, and Ryan Lemar. I would also like to acknowledge the BalletSchool of Charlottesville and Atsuko Nakamoto for giving me a dance outlet during the pandemic.

I would like to show some love to all of my UVA and St. John's friends that haven't been mentioned already. My physics undergrad friends who helped me through the bridge program year, with special mention of Addie Pollard and Jesse Han. The Sad Grads: Anna Hall, Thomas Krahulik, Grace Cummings, Miller Eaton, Matt Wampler, Arthur Conover, and Akin Morrison. Johnnies: Frances Webb, Christine Rowaghani, Grace Athanas-Linden, David Conway, Patrick Kelly, and Joe Kensok.

Finally, I would like to thank my husband, Sean Jeffas, for his support and love throughout this whole process. I am so happy we did this whole grad school thing together; from taking classes and doing homework, to moving in and getting married. I love you wholeheartedly and I can't imagine going through life without you.

# Contents

<b>Abstract</b>	<b>iii</b>
<b>Acknowledgements</b>	<b>v</b>
<b>1 Introduction</b>	<b>1</b>
1.1 Overview of Dissertation . . . . .	1
1.2 Inertial Navigation and GPS . . . . .	2
1.2.1 Inertial Sensors and Forces . . . . .	4
1.3 Rotation Sensing and Gyroscopes . . . . .	4
1.3.1 Rotation Effects . . . . .	6
Coriolis Effect . . . . .	6
Sagnac Effect . . . . .	7
1.3.2 Classical Gyroscopes . . . . .	9
1.4 Errors . . . . .	11
1.4.1 Bias . . . . .	12
1.4.2 Random Noise . . . . .	13
1.4.3 Other Types of Error . . . . .	13

1.4.4	Position Error Example . . . . .	14
1.5	Allan Variation and Deviation . . . . .	16
1.5.1	Overview . . . . .	16
1.5.2	Noise Model . . . . .	18
1.5.3	Discrete Case . . . . .	21
1.5.4	Single Sensor Discussion . . . . .	23
<b>2</b>	<b>Techniques and Previous Work</b>	<b>24</b>
2.1	Bose-Einstein Condensation . . . . .	24
2.2	Atom Interferometry . . . . .	25
2.2.1	Bragg Splitting . . . . .	25
2.2.2	Atom Interferometer Rotation Sensors . . . . .	27
2.3	Time Orbiting Potential (TOP) Trap . . . . .	29
2.4	Method and Previous Work . . . . .	31
2.4.1	Experimental Method . . . . .	31
2.4.2	Rotation Measurement Summary . . . . .	34
2.4.3	Instrumentation and Difficulties . . . . .	35
<b>3</b>	<b>Lab-Scale Apparatus</b>	<b>38</b>
3.1	Instrumentation . . . . .	38
3.1.1	Assembling the Science Chamber . . . . .	39
3.1.2	Water Cooling System . . . . .	42
3.1.3	Imaging and Bragg Optics . . . . .	44

3.1.4	Drive Electronics . . . . .	46
3.2	Magnetic Field Characterization . . . . .	49
3.3	Thermal Characterization . . . . .	50
3.4	Interferometer Method . . . . .	52
3.4.1	Limiting Residual Oscillations . . . . .	52
3.4.2	Trap Symmetry . . . . .	54
3.4.3	Cross Term Precession . . . . .	55
3.4.4	Trajectories . . . . .	56
	Trajectories in the Horizontal Plane . . . . .	56
	Trajectories in the Vertical Planes . . . . .	58
3.4.5	Interferometer Characterization . . . . .	59
3.5	Results . . . . .	62
3.5.1	Multiple Orbits . . . . .	62
3.5.2	Phase Stability and Characterization . . . . .	64
3.5.3	Trap Frequency and Cross Term Noise Analysis . . . . .	70
<b>4</b>	<b>Compact System</b> . . . . .	<b>72</b>
4.1	Experimental Apparatus . . . . .	72
4.1.1	Overview . . . . .	72
4.1.2	Vacuum System . . . . .	74
4.1.3	Optics . . . . .	77
4.1.4	Atom Chips and Coils . . . . .	82

4.2	Results and Challenges . . . . .	84
4.2.1	Chip heating . . . . .	85
4.2.2	Beam polarization . . . . .	85
4.2.3	Beam alignment . . . . .	87
4.2.4	MOT Monitoring . . . . .	89
4.2.5	Magnetic Trapping . . . . .	91
<b>5</b>	<b>Conclusion and Future Work</b>	<b>93</b>
5.1	Hybrid Apparatus . . . . .	94
5.1.1	High Performance Amplifiers . . . . .	95
5.2	Comparison with Modern Day Gyroscopes . . . . .	96
5.3	Summary . . . . .	98
	<b>Bibliography</b>	<b>101</b>
<b>A</b>	<b>Feedthrough Schematic</b>	<b>106</b>
<b>B</b>	<b>Bias Coil Information</b>	<b>108</b>

# Chapter 1

## Introduction

### 1.1 Overview of Dissertation

The structure of this dissertation is as follows: Chapter 1 will motivate a compact atom-based gyroscope in the context of an inertial navigation system and the sensors currently used for navigation. An extensive discussion of gyroscope sensor errors and characterization of the stability and sensitivity of these sensors will also be discussed. Chapter 2 will present an overview of the atomic physics techniques employed in the rotation sensors built at UVA and a brief survey of atom interferometer gyroscopes. Previous work done in the lab at UVA will be presented. Chapter 3 will describe a new laboratory-based apparatus and a first-time measurement of the long-term stability with the interferometer method presented. Chapter 4 will describe the characterization, challenges, and results from experiments performed with a compact prototype sensor. Chapter 5 will conclude the dissertation with remarks about the future of this technique, the description of a new experimental apparatus, and will relate the results from Chapter 3 to typical gyroscope stability values and sensitivities.

## 1.2 Inertial Navigation and GPS

Inertial navigation is the process of navigating without the use of external references (i.e. stars, landmarks, GPS, etc.). Inertial Navigation Systems (INS)<sup>1</sup> are devices that calculate the user's position, orientation, and velocity using inertial sensors and a computer. Inertial sensors include accelerometers, for calculating linear accelerations, and gyroscopes, for calculating rotations. In 1907, Robert Goddard was the first to publish a theoretical paper with the idea of using a gyroscope to stabilize a plane [3] and continued to develop the technique for use in rockets. INS would go on to be used exclusively for military application until the 1980s when the Delco Carousel system would be used commercially on Boeing 747s [4]. Nowadays, INS are used in a variety of applications, from micro-electrical chips in your cellphone to state-of-the-art sensors in military vehicles.



FIGURE 1.1: **Transatlantic flight display INS.** Non-operational prototype made for display purposes by the Delco Division of General Motors. The Delco Carousel dimensions were  $25.4 \times 54.6 \times 20.3$  cm. [5]

Currently, the Global Positioning Services (GPS) is the main system that enables navigation around the Earth. GPS first became operational for navigation in 1993 and is a network of 31 satellites that orbit the earth. GPS uses a combination of satellites,

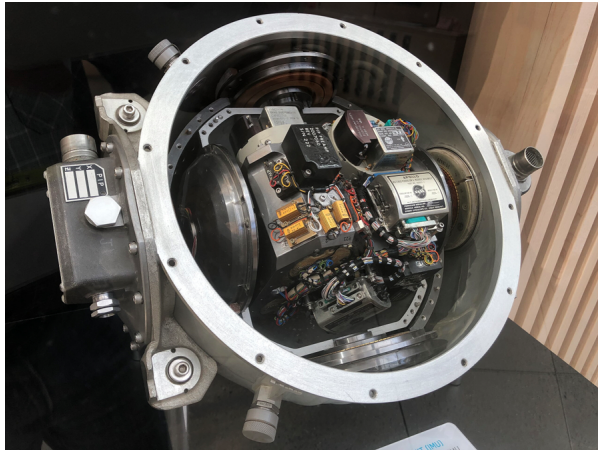
---

<sup>1</sup>Throughout chapter 1, I will be using [1] and [2] for information generally pertaining to inertial navigation and sensors. These are great resources for anyone interested in learning more on the topic.

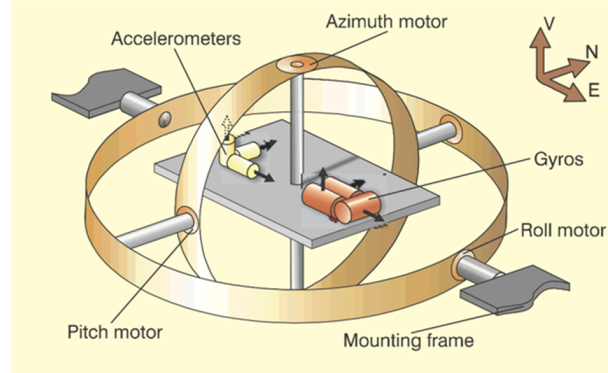
ground control locations, and the user's receiver to calculate the user's position, velocity, and time. GPS requires line of sight between four satellites and the receiver to accomplish this task. However, GPS signals are weak [6] and achieving line of sight in inclement weather or restricted environments can be nearly impossible. Furthermore, GPS is susceptible to bad actors, faking GPS signals from radio transmitters ("spoofing") [7] and blocking signals ("jamming") [8]. While none of these failures would be a problem for a trip to the store, these could result in serious loss of important infrastructure or life if GPS fails in certain circumstances.

Modern day vehicles rely on a combination of GPS and INS to navigate. However, inertial sensors are imperfect devices subject to drift. This drift occurs when the devices heat up, wear out due to continuous use, or the consequence of differences in manufacturing. Inertial sensor drift introduces errors that, over time, accumulate and lead to an incorrect calculation of the position, velocity, and orientation (see section 1.4). One possible solution to this problem in high-performance applications is to use atom-based sensors to measure accelerations and rotations. Atoms offer an intrinsically stable and precise platform for measuring inertial forces [9]. However, atom-based sensors are generally laboratory-sized apparatuses that are highly complex and not suitable for deployment in a vehicle.

The focus of this dissertation will be on the development of a compact, atom-based gyroscope through the research and development of both a new laboratory-sized system and a compact prototype. In this chapter, I will acquaint the reader with inertial sensing in the context of gyroscopes and discuss gyroscopic errors, finishing with a discussion of Allan deviation as a means to characterize the stability and performance of a gyroscope.



(A) Apollo program IMU. Displayed at Draper Labs in 2019 "Hack the Moon" exhibit in honor of the 50th anniversary of the Apollo 11 moon landing. [10]



(B) Diagram of gimbaled IMU. In a gimbaled IMU, the gyroscopes are used to measure a change in rotation rate and angle for the purpose of keeping the accelerometers aligned with the appropriate axis relative to the horizon or vehicle. [11]

FIGURE 1.2: Gimbaled IMU

### 1.2.1 Inertial Sensors and Forces

An Inertial Measurement Unit (IMU) contains three accelerometers and three gyroscopes placed orthogonally at the center of a rotating gimbaling device or in a strap-down configuration. Fig. 1.2 shows the gimbaled configuration. The inertial sensors can be placed on a gimbaling device to keep a fixed reference frame with respect to the horizon and for self-calibration and gyrocompassing. In the strap-down configuration, the IMU is fixed in place so that its axes align with the vehicle's axes. The types of measurements can be seen in Fig. 1.3.

## 1.3 Rotation Sensing and Gyroscopes

Both accelerometers and gyroscopes are important but IMUs are typically characterized by the gyroscope's in-run bias stability, which is a measure of the random drift in the bias over the course of operation, and the angle random walk, which is a measure of the gyroscope's short-term noise caused by random noise. The angle random walk

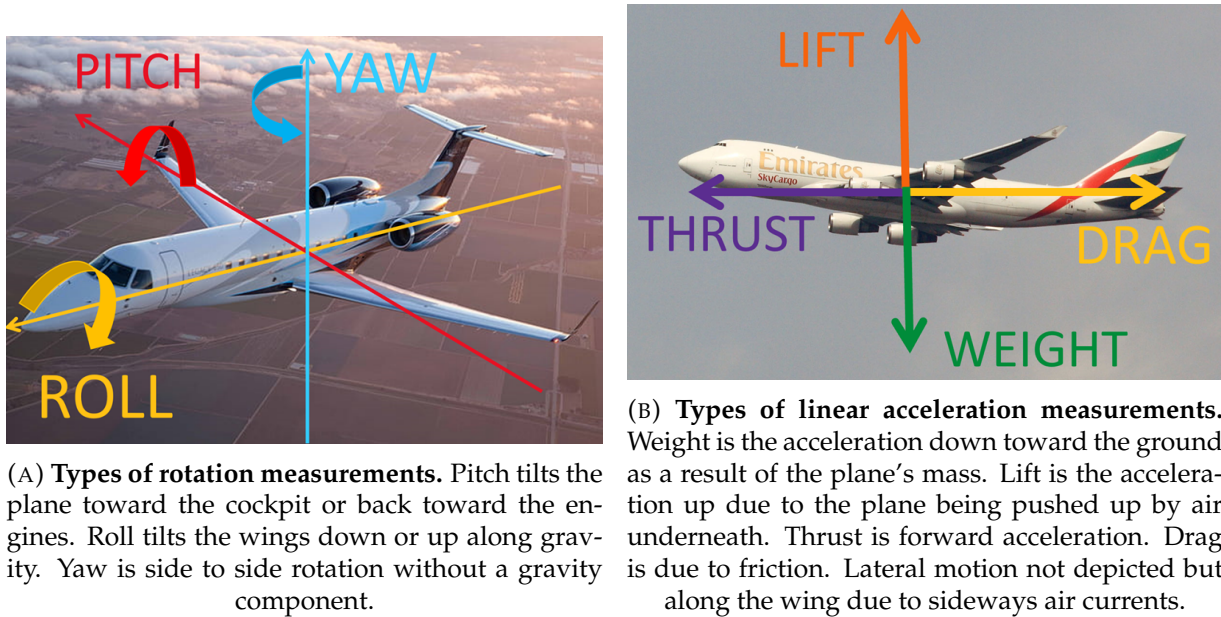


FIGURE 1.3: Types of inertial measurements

can also be thought of as a description of the sensitivity of the gyroscope (see Section 1.4). When a gyroscope is operated in conjunction with an accelerometer, the gyroscope performance typically dominates the performance of the whole IMU.

Grade	Strategic grade	Navigation grade	Tactical grade	Commercial grade <sup>a</sup>
Positional error	30–100 m/h	1 nmi <sup>b</sup> /h or 0.5 m/s	10–20 nmi/h	Large variation
Gyroscope drift	0.0001–0.001°/h	< 0.01°/h	1–10°/h	0.1°/s
Gyroscope random walk	–	< 0.002°/√h	0.05–< 0.02 °/√h	Several °/√h
Accelerometer bias	0.1–1 μg	< 100 μg	1–5 mg	100–1000 μg
Applications	Submarines Intercontinental ballistic missiles	General navigation High precision georeferencing Mapping	Integrated with GPS for mapping Weapons (Short time)	Research Low cost navigation Pedometers Anti-locking breaking Active Suspension Airbags
Cost	~\$1 million	~\$100,000	~\$2000–\$50,000	\$1 for accelerometers \$10 for gyroscopes

<sup>a</sup> Also called automotive grade

<sup>b</sup> 1 nautical mile (nmi) ≈ 6076 ft ≈ 1851 m

FIGURE 1.4: **Table with typical grades, costs, and performance for IMUs.** This table presents the standard descriptions of different IMUs with the least sensitive and stable being the commercial grade and the most sensitive and stable being the strategic grade. [12]

There are four main types of classical gyroscopes that I will discuss: Micro-Electric-Mechanical Systems (MEMS) gyros, Ring Laser Gyros (RLG), Interferometric Fiber Optic Gyros (IFOG or FOG), and mechanical gyros, both Hemispherical Resonator Gyros (HRG) and spinning top gyroscopes. The majority of the gyroscopes discussed will rely on the Sagnac effect to measure rotations which will be covered in the following section.

### 1.3.1 Rotation Effects

To understand gyroscopic operation and stability and sensitivity characterization, two different rotation effects will be discussed: the Coriolis and Sagnac effects.

#### Coriolis Effect

Consider sitting on a merry go round carousel as it spins counter-clockwise. If you roll a ball forward as the carousel spins, the ball will be deflected to the right. This deflection is the Coriolis effect as the ball experiences the Coriolis force. An efficient way to analyze the Coriolis force is using Lagrangian mechanics. A derivation of the rotating Lagrangian can be found in [13], here is a simplified Lagrangian with the Coriolis effect:

$$L = L_0 + V_{cf} + m\mathbf{v} \cdot (\boldsymbol{\Omega} \times \mathbf{r}) \quad (1.1)$$

where  $L_0$  is the Lagrangian in the inertial frame,  $V_{cf}$  is due to the centrifugal force, and the third term is the Coriolis term, where  $\mathbf{v}$  is the particle velocity in the rotating frame,  $\boldsymbol{\Omega}$  is the rotation rate of the frame, and  $\mathbf{r}$  is the position vector. The Coriolis force is thus:

$$\mathbf{F}_{cor} = \nabla L_{cor} = m\mathbf{v} \times \boldsymbol{\Omega} \quad (1.2)$$

### Sagnac Effect

The Sagnac interferometer is an effective way to measure rotations. A Sagnac interferometer [14] is comprised of two counter-propagating beam paths enclosing an area,  $A$ . If the system is not experiencing a rotation, the light path lengths are the same for each arm of the interferometer in both frames. However, if the system rotates, the light path lengths will become different in the inertial frame. This causes a phase shift between the light waves that is proportional to the rotation rate,  $\Omega$ .

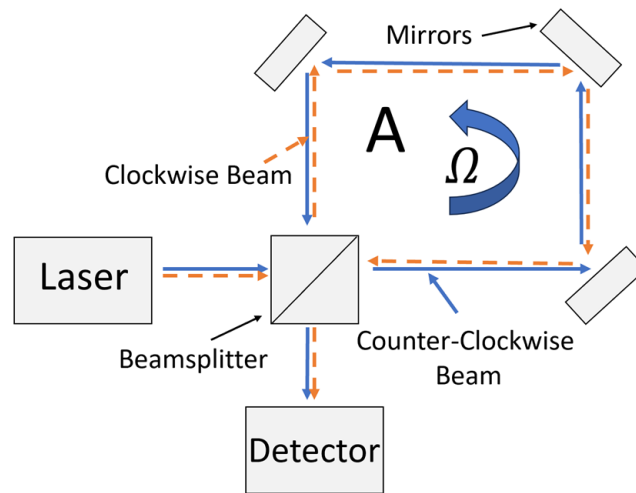


FIGURE 1.5: **Illustration of a Sagnac interferometer.** The blue beam is the counter-clockwise beam and the orange dashed line is the clockwise beam. Both beams come from the same laser but as they travel and enclose a rotating area, the path length for each beam changes. This induces a phase shift that is measurable on a detector.

We can derive this phase shift by integrating over the Coriolis term in the Lagrangian:

$$\phi_{Sagnac} = \frac{1}{\hbar} \oint L dt \quad (1.3)$$

$$= \frac{1}{\hbar} \oint (m\mathbf{v} \cdot \boldsymbol{\Omega} \times \mathbf{r}) dt \quad (1.4)$$

$$= \frac{m}{\hbar} \cdot \boldsymbol{\Omega} \oint (\mathbf{r} \times \mathbf{v}) dt \quad (1.5)$$

$$= \frac{m}{\hbar} \cdot \boldsymbol{\Omega} \oint (\mathbf{r} \times \frac{d\mathbf{r}}{dt}) dt \quad (1.6)$$

$$= \frac{m}{\hbar} \boldsymbol{\Omega} \cdot \oint \mathbf{r} \times d\mathbf{r} \quad (1.7)$$

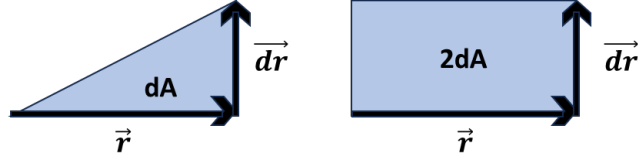


FIGURE 1.6: Cartoon picture for cross-product definition.

Now using  $\mathbf{r} \times d\mathbf{r} = 2dA$  (Fig. 1.6), we finally get:

$$\phi_{Sagnac} = \frac{2m}{\hbar} \boldsymbol{\Omega} \cdot A \quad (1.8)$$

$$= \frac{4\pi}{\lambda v} \boldsymbol{\Omega} \cdot A \quad (1.9)$$

where  $\boldsymbol{\Omega}$  is the rotation rate of the system,  $A$  is the area enclosed by the interferometer,  $\lambda$  is the wavelength and equal to  $\frac{2\pi\hbar}{mv}$ , and  $v$  is the phase velocity (for an optical interferometer  $v = c$ ). Eq. 1.9 holds for both matter-waves and massless waves. Atom interferometers present an advantage over light-based interferometers because their velocity is significantly smaller at a given wavelength. In comparison, an interferometer using light of frequency  $\omega_L$  has  $\frac{8\pi}{\lambda v} = \frac{4\omega_L}{c^2}$ , and it is the large ratio  $\frac{mc^2}{\hbar\omega_L} \sim 10^{11}$  that makes atomic Sagnac interferometers attractive. In addition, the area must be as large as possible to realize a high sensitivity.

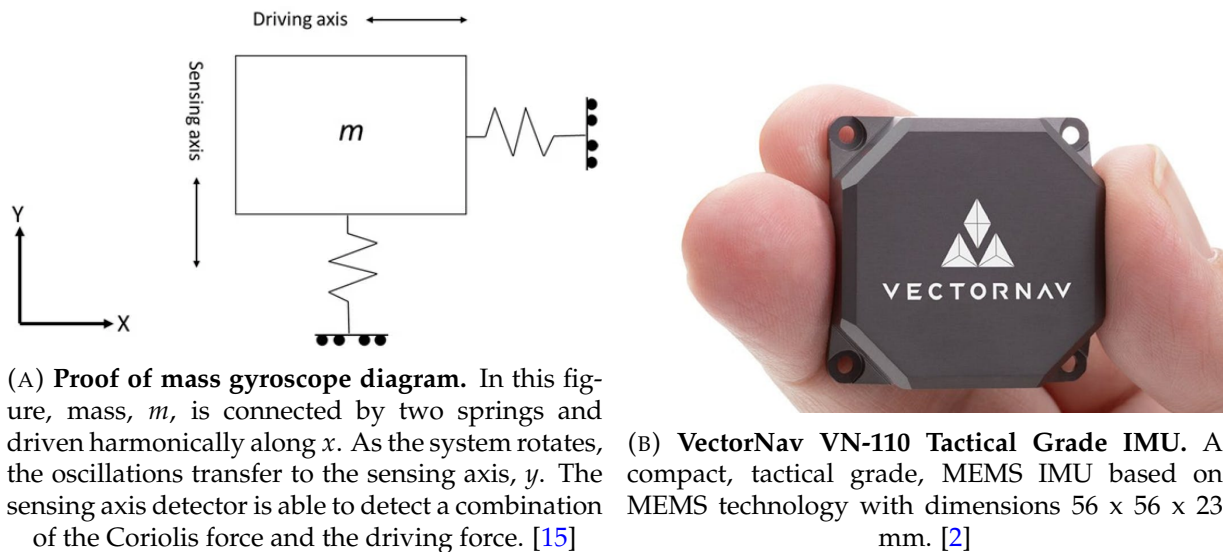
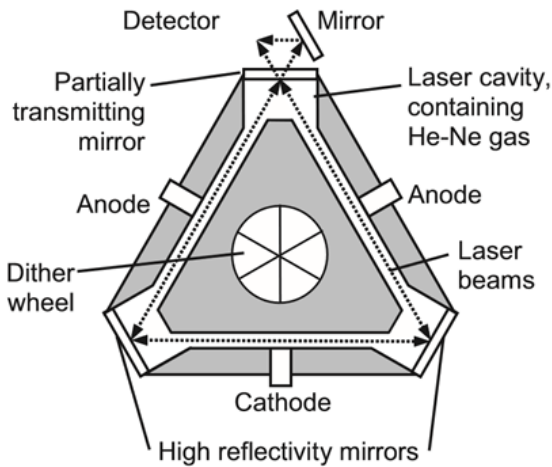


FIGURE 1.7: MEMS gyroscopes

### 1.3.2 Classical Gyroscopes

MEMS gyroscopes are the smallest but least precise and stable gyroscope available. These are small, chip scale devices that operate using the Coriolis effect to displace materials within the device to measure a change in capacitance proportional to the rotation rate. These are typically commercial grade devices (with some at the tactical grade, see 1.7b) and are found in smartphones and other low performance devices. These devices are configured in a variety of ways with a simple case being a proof mass concept (see 1.7a). This configuration can provide insensitivity to linear accelerations with the use of multiple masses because when the system is rotating, the Coriolis force acts upon each mass in the opposite direction with a capacitance change (if using capacitor plates as the proof masses) proportional to the rotation rate. If the system is moving linearly, then the two masses will move together resulting in no net change in capacitance.

RLG and IFOG gyroscopes (see Figs. 1.8 and 1.9) both operate using the Sagnac effect so they require counter-propagating beams enclosing the same area over the same path in order to measure rotations. The RLG uses a ring laser to accomplish this task



(A) **RLG diagram.** The laser cavity is a tube filled with Helium-Neon gas mixture with cathodes and anodes to provide a large potential difference producing an electric field. This electric field excites the atoms to emit photons of the same wavelength. However, if the RLG is rotating, the two counter-propagating, lasing modes will experience a measurable phase shift through the Sagnac Effect. [1]

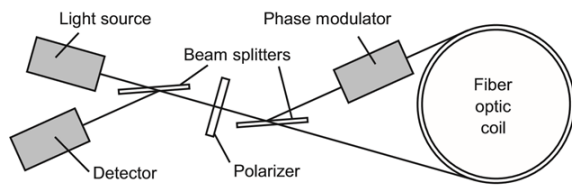


(B) **Honeywell RLG.** [16]

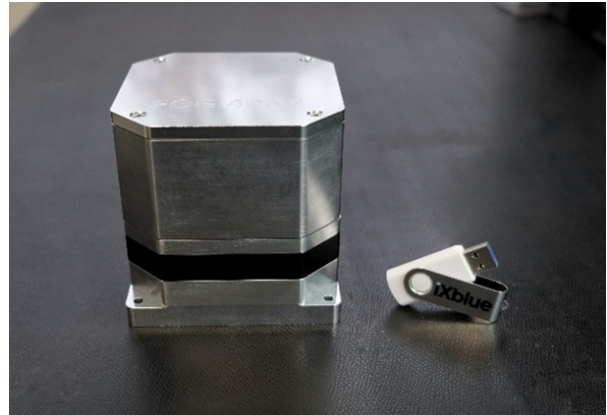
FIGURE 1.8: **RLG gyroscopes**

by using two different counter-propagating resonant modes in the same cavity. The IFOG uses light coupled into an optical fiber in opposite directions. Both RLG and IFOG gyroscopes measure a phase shift when the system is rotating that is proportional to the rotation rate. These devices have the widest application ranges and are able to achieve higher sensitivities by increasing the Sagnac area through multiple windings of the optical fiber in an IFOG or using highly reflective mirrors to direct the light around the RLG multiple times. The atom-based gyroscopes developed at UVA are heavily inspired by these gyroscopes.

Mechanical gyroscopes (see Fig. 1.10), particularly the hemispherical resonator gyroscope (HRG), are the most precise classical gyroscopes and are strategic grade. An HRG also uses wave effects but with sound waves induced on an inner shell anchored by a thick stem. Inertial forces cause a precession of the standing wave around the shell as the object rotates, causing a phase shift between the input wave and the detected



(A) **IFOG diagram.** Light is counter-propagated through a single fiber optic coil. As the system rotates, a phase shift is measured at the detector and through the Sagnac effect you can measure the rotation rate of the system. [1]



(B) **iXblue Astrix NS FOG.** Compact FOG gyroscope with dimensions 100 x 100 x 100 mm. [17]

FIGURE 1.9: **IFOG gyroscopes**

one. While a mechanical system, it has no moving parts and is incredibly compact, making it perfect for space based applications. The original gyroscopes are spinning mass gyroscopes that behave the same as a spinning top. These do not use the Sagnac effect and experience friction as a result of their moving parts but have been used as a level, to locate the horizon, and to demonstrate earth rotation.

## 1.4 Errors

All inertial sensors are imperfect. The consequence of these imperfections is that the measured value of the rotation or acceleration is not the same as the "true" value. This causes difficulties in position finding because these errors integrate and compound over time as the sensor uses previous measurements to make new measurements. In this section, the compounding errors in position measurements will be demonstrated, the meaning and importance of different error terms discussed, and the Allan variance behavior presented as the primary method for characterizing these errors in gyroscopes.



(A) Northrop Grumman HRG picture. [18]



(B) Replica of spinning gyroscope designed by **Leon Foucault**. A spinning gyroscope based on a Serson speculum gyroscope. This type of gyroscope was used in first detecting the rotation of the earth. [19]

FIGURE 1.10: Mechanical gyroscopes

### 1.4.1 Bias

The bias in an inertial sensor can be thought of as the long term, constant noise that is present in the system. The bias has both a static and dynamic term and can be written as:

$$b_{a,g} = b_0 + b'(t) \quad (1.10)$$

where  $b_0$  is the static term, also known as the run-to-run bias and  $b'(t)$  is time-dependent and known as the in-run bias. The static bias is not truly static and can vary day-to-day and over long times (see Section 1.5). The dynamic bias is typically much smaller than the static bias [1] in magnitude but can dominate at very long measurement times. For simplicity, we will take only the static bias into consideration. The units for the gyroscope bias are ordinarily given in units of deg/hr (or deg/s).

### 1.4.2 Random Noise

The random noise in an inertial sensor can be thought of as the short-term drift in the sensor caused by random white noise, defined as  $\eta_{a,g}$  below. If you integrate this white noise over some time,  $T$ :

$$\int_0^T \eta_{a,g} dt = R\sqrt{T} \quad (1.11)$$

This is the definition of a random walk,  $R$ . For a gyroscope output, we will denote it by  $ARW$  which stands for **Angle Random Walk** and, for an accelerometer output, we will denote it by  $VRW$  which stands for **Velocity Random Walk**. The units for  $ARW$  are ordinarily given in deg/ $\sqrt{\text{hr}}$ . Random noise can effect the static bias drift at longer times and will be addressed in Section 1.5.

### 1.4.3 Other Types of Error

The other notable type of error not addressed above is the scale factor error. It is related to the  $ARW$  and the bias stability through this intuitive cartoon graph (Fig. 1.11). The scale factor is a measure of the accuracy of the gyroscope in sensing the correct angular velocity. The scope of this dissertation will not include further discussion of the scale

factor error because the concern of our particular atom-based gyroscopes is in measuring small rotations (behavior around zero in Fig. 1.11). Another important set of errors are orthogonality errors. These are errors due to misalignment of the IMU axes with the vehicle axes. This error leads to a measurement where the devices designed to be sensitive to inertial forces along one axis are actually sensitive to inertial forces from other axes as well. The last error I will address is that gyroscopes can be sensitive to linear accelerations. However, these errors produce a bias shift in the gyroscope and can be calibrated and subtracted out. Furthermore, the atom-based gyroscopes at UVA are insensitive to these types of errors due to the symmetry of our design.

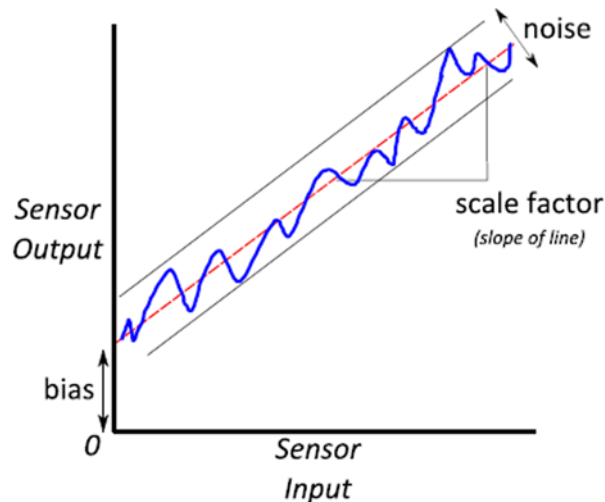


FIGURE 1.11: **Gyroscope Noise Cartoon.** The offset at zero shows the bias of the system. The blue line is a representation of the data and random noise. The dashed red line is the fit of the data to a line and the slope of that line represents the scale factor error. [12]

#### 1.4.4 Position Error Example

The simplified example in this section draws heavy inspiration from [2]. Let's begin with a system that is not rotating and is accelerating along one axis. We will consider

only one axis for this generalized example. The output from the gyroscope measuring a rotation orthogonal to the acceleration direction can be defined as:

$$\tilde{\omega} = \omega_t + b_g + \eta_g \quad (1.12)$$

where  $\tilde{\omega}$  is the measured rotation,  $\omega_t$  is the "true" rotation ( $\omega_t = 0$  in this example),  $b_g$  is the gyroscope bias, and  $\eta_g$  is the random noise on the rotation measurement. The output from the accelerometer can be defined as:

$$\tilde{\alpha} = \alpha_t + b_a + \eta_a + \begin{cases} g \sin \Theta_{err} & \text{[horizontal motion]} \\ g(1 - \cos \Theta_{err}) & \text{[vertical motion]} \end{cases} \quad (1.13)$$

where  $\tilde{\alpha}$  is the measured acceleration,  $\alpha_t$  is the "true" acceleration,  $b_a$  is the accelerometer bias,  $\eta_a$  is the random noise on the acceleration measurement,  $g$  is gravity, and  $\Theta_{err}$  is the angular error from the gyroscope measurement. The gravity terms are introduced because the accelerometer measures linear accelerations of the vehicle, *including* gravity and depends on the determined pitch or roll of the vehicle from the gyroscope output.

The angular error is:

$$\Theta_{err} = \int_0^T (\tilde{\omega} - \omega_t) dt \quad (1.14)$$

which simply says that the error in the rotation measurement is the difference between the measured and "true" rotation over some measurement time  $T$ . Plugging in equations 1.12, 1.10 (only the static part), 1.11 and integrating gives:

$$\Theta_{err} = b_{0g}T + ARW\sqrt{T} \quad (1.15)$$

Now, the process of finding the position error involves finding the velocity error from

the accelerometer and integrating over that. To find the velocity error, we perform a similar operation with the accelerometer output but we will assume that our system is moving in the horizontal plane and that  $\Theta_{err}$  is small. This simplifies equation 1.13 to:

$$\tilde{\alpha} = \alpha_t + b_a + \eta_a + g\Theta_{err} \quad (1.16)$$

Now performing a similar integration as equation 1.14, we get:

$$V_{err} = VRW\sqrt{T} + b_{0a}T + \frac{2}{3}g(ARW)T^{3/2} + \frac{1}{2}gb_{0g}T^2 \quad (1.17)$$

And finally, integrating again gives the position error:

$$P_{err} = \frac{2}{3}(VRW)T^{3/2} + \frac{1}{2}b_{0a}T^2 + \frac{4}{15}g(ARW)T^{5/2} + \frac{1}{6}gb_{0g}T^3 \quad (1.18)$$

The first two terms in equation are the error terms due to the accelerometer static bias and random noise and the last two, dominant terms, are the gyroscope bias and random noise. Of particular note, this example demonstrates that the static gyroscope bias (or run-to-run bias) is the dominant source of noise at large  $T$  in position finding and is therefore a *critical* value when evaluating the performance of an IMU.

## 1.5 Allan Variation and Deviation

### 1.5.1 Overview

In order to evaluate the sensitivity and stability of the gyroscope, the Allan variation method is commonly used. This method for analyzing noise was created by David W.

Allan in the 1960s for analyzing the frequency stability of atomic clocks. The Allan variation (and its square root, Allan deviation) is a measure of the stability of the system as it pertains to noise processes, not systematic errors. In an Allan deviation measurement, the gyroscope is in a non-rotating configuration and data is collected over a long time. This data is then binned according to different possible averaging times. Once all of the data is binned, then a standard deviation is calculated for the data binned for a specific averaging time. The standard deviation and averaging time is then plotted on a log-scale plot.

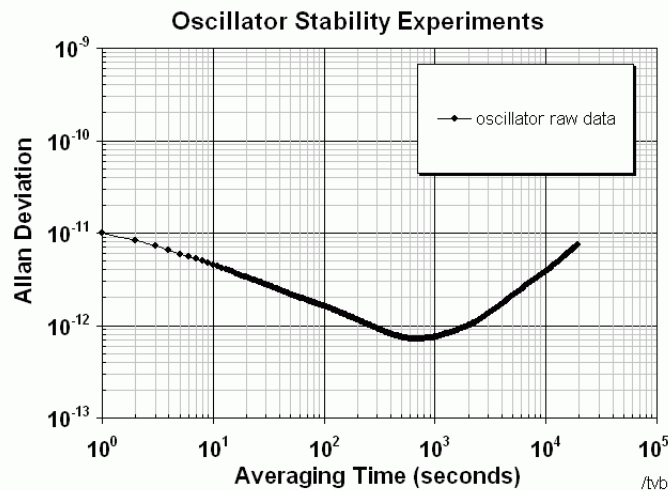


FIGURE 1.12: **Allan deviation example plot.** This plot shows a flat angle random walk approaching  $1/\sqrt{T}$  and demonstrating bias stability out to almost 1000 s where the slope equals zero. The graph turns around indicating that the bias has drifted past 1000 s so the system bias is unstable past that averaging time. [20]

As stated before, rotational sensitivity of a device is typically characterized by the angle random walk, where the orientation error grows as  $ARW\sqrt{T}$  (Eq. 1.15). The angle random walk is characterized by the Allan deviation plot in the region where the slope is equal to -0.5 and decreases according to  $1/\sqrt{T}$ . This slope characteristic indicates that the system is dominated by the angle random walk in this region and that the bias is stable. To calculate the sensitivity and total short term noise in the system, all one needs to do is extrapolate the angle random walk slope back to an averaging time of 1 s and

calculate the Allan deviation. The value of the Allan deviation at the location where the slope becomes zero can be used to estimate the bias stability and that averaging time indicates the maximum integration time that can be used. The turn around behavior after the bias indicates that the bias is not static and changes, demonstrating the drift behavior of the gyroscope. These features and behavior will be modeled in more detail now.

## 1.5.2 Noise Model

Returning to the non-rotating gyroscope example, the output can be written as:

$$\Omega(t) = A\eta(t) + \beta(t) \quad (1.19)$$

Here  $A$  is a constant amplitude and  $\eta, \beta$  are stochastic signals (these will be explained more fully briefly). In this derivation, we will consider a sensor with a continuous output over time, with a discrete derivation in the next section. Another assumption about this configuration is that the noise processes above have a zero mean:  $\langle \eta \rangle = \langle \beta \rangle = 0$ . For now, we can interpret these averages as ensemble averages. We will consider a large ensemble of nominally identical sensors that output different noise signals and average the noise over this ensemble. This method will be related to sequential measurements of a single sensor later.

The  $\eta(t)$  term describes rapidly fluctuating white noise in the sensor output. This term corresponds to the angle random walk process described previously and is due to white noise. The two-time correlation function of this term is the Dirac delta function:

$$\langle \eta(t)\eta(t') \rangle = \delta(t - t') \quad (1.20)$$

The  $\beta(t)$  term describes bias drifting due to a random walk process applied to the bias. In a random walk process, the output of an individual sensor will deviate in a diffusion-like process as:

$$\Omega(t') \approx \Omega(t) + k\sqrt{|t - t'|} \quad (1.21)$$

for nominally constant  $k$ . Therefore, averaging over the ensemble for this term gives:

$$\langle [\Omega(t') - \Omega(t)]^2 \rangle = \langle \Omega(t)^2 \rangle + \langle \Omega(t')^2 \rangle - 2\langle \Omega(t)\Omega(t') \rangle = \langle k^2 \rangle |t - t'| \quad (1.22)$$

The ensemble is also stationary with  $\langle \Omega(t)^2 \rangle$  constant. However, this is not consistent with a true random walk, since, as time goes to infinity, the spread of the output values would diverge. Instead, we assume the signals undergo a random walk over the time scale of interest, but over longer times the drifts are contained so that  $\langle \Omega(t)^2 \rangle$  remains constant. Using this assumption, Eq. 1.22 becomes:

$$\langle [\Omega(t') - \Omega(t)]^2 \rangle = 2[\langle \Omega(t)^2 \rangle - \langle \Omega(t)\Omega(t') \rangle] = \langle k^2 \rangle |t - t'| \quad (1.23)$$

which leads to

$$\langle \Omega(t)\Omega(t') \rangle = \langle \Omega(t)^2 \rangle + \frac{\langle k^2 \rangle}{2} |t - t'| \quad (1.24)$$

To model the bias drifting due to the random walk effect, we take:

$$\langle \beta(t)\beta(t') \rangle = B^2 + C^2 |t - t'| \quad (1.25)$$

with positive constants  $B, C$ . If  $C = 0$ , then this describes an ensemble with a range of sensor output values,  $\Omega$ , that are not drifting. Note that  $B = 0$  while  $C \neq 0$  cannot consistently happen because this would describe an ensemble of sensors whose biases are all zero and drifting. This situation is only possible if the sensors are calibrated at a given time, but the subsequent evolution will not be stationary.

To characterize all of the noise processes in the sensor output, the Allan variance is used and defined as:

$$\sigma_{\tau}^2 = \langle \Omega_{\tau}^2 \rangle - \langle \Omega_{\tau} \rangle^2 \quad (1.26)$$

where  $\Omega_{\tau}$  is the rotation signal obtained after averaging the output for time  $\tau$ :

$$\Omega_{\tau} \equiv \frac{1}{\tau} \int_0^{\tau} \Omega(t) dt \quad (1.27)$$

The angle brackets in Eq. 1.42 represent ensemble averages, while  $\Omega_{\tau}$  is a time average for an individual sensor. The Allan deviation,  $\sigma_{\tau}$ , is the square root of the Allan variance.

The ensemble average over a single sensor output is:

$$\langle \Omega_{\tau} \rangle = \frac{1}{\tau} \int_0^{\tau} \langle \Omega(t) \rangle dt = 0 \quad (1.28)$$

and

$$\langle \Omega_{\tau}^2 \rangle = \frac{1}{\tau^2} \int_0^{\tau} \int_0^{\tau} \langle \Omega(t) \Omega(t') \rangle dt dt' \quad (1.29)$$

This can be evaluated using the noise model described above and another assumption is that the different noise processes are uncorrelated (i.e.  $\langle \eta(t) \beta(t') \rangle = 0$ ) Eq. 1.29 becomes:

$$\langle \Omega_{\tau}^2 \rangle = \frac{1}{\tau^2} \int_0^{\tau} \int_0^{\tau} A^2 \langle \eta(t) \eta(t') \rangle + \langle \beta(t) \beta(t') \rangle dt dt' \quad (1.30)$$

Now each process can be evaluated individually.

Starting with the first term and using Eq. 1.20 in the previous equation:

$$\frac{A^2}{\tau^2} \int_0^{\tau} \int_0^{\tau} \langle \eta(t) \eta(t') \rangle dt dt' = \frac{A^2}{\tau^2} \int_0^{\tau} \int_0^{\tau} \delta(t - t') dt dt' = \frac{A^2}{\tau} \quad (1.31)$$

The second term gives two contributions:

$$\frac{B^2}{\tau^2} \int_0^\tau \int_0^\tau 1 dt dt' + \frac{C^2}{\tau^2} \int_0^\tau \int_0^\tau |t - t'| dt dt' = B^2 + \frac{C^2}{\tau^2} \int_0^\tau \int_0^\tau |t - t'| dt dt' \quad (1.32)$$

The second term can be analyzed by splitting the integral into two ranges where  $t' < t$  and the other where  $t' > t$ , thus removing the absolute values.

$$\frac{C^2}{\tau^2} \left[ \int_0^\tau \int_0^t (t - t') dt dt' + \int_0^\tau \int_t^\tau (t' - t) dt dt' \right] = \frac{C^2}{\tau^2} \left[ \frac{\tau^3}{6} + \frac{\tau^3}{6} \right] = \frac{C^2 \tau}{3} \quad (1.33)$$

Thus the total Allan variance in this model is:

$$\sigma_\tau^2 = \frac{A^2}{\tau} + B^2 + \frac{C^2 \tau}{3} \quad (1.34)$$

This diverges as  $\tau \rightarrow 0$  due to the short term white noise and as  $\tau \rightarrow \infty$  due to the bias drift. This explains the averaging down and turn around behavior seen in Fig. 1.12 above.

### 1.5.3 Discrete Case

In a realistic sensor, there will be some sample time,  $\Delta t$ , corresponding to the minimum time interval at which results can be measured. So the definition (Eq. 1.27) must be changed to:

$$\Omega_\tau \equiv \frac{1}{n} \sum_{j=1}^n \Omega(t + j\Delta t) \quad (1.35)$$

with  $\tau = n\Delta t$ . In addition, the white noise process correlation function (Eq. 1.20) becomes:

$$\langle \eta(t + i\Delta t) \eta(t + j\Delta t) \rangle = \delta_{ij} \quad (1.36)$$

The units and interpretation of the  $A$  coefficient change accordingly and the white noise result (Eq. 1.31) becomes:

$$\frac{A^2}{n^2} \sum_{i=1}^n \sum_{j=1}^n \langle \eta(t + i\Delta t) \eta(t + j\Delta t) \rangle = \frac{A^2}{n} = \frac{A^2 \Delta t}{\tau} \quad (1.37)$$

The bias stability and drift term correlation function (Eq. 1.25) becomes:

$$\langle \beta(t + i\Delta t) \beta(t + j\Delta t) \rangle = B + C|i - j| \quad (1.38)$$

This function leads to:

$$\frac{1}{n^2} \sum_{i=1}^n \sum_{j=1}^n \langle \beta(t + i\Delta t) \beta(t + j\Delta t) \rangle = \frac{1}{n^2} = \left[ n^2 B^2 + C^2 \sum_{i=1}^n \sum_{j=1}^n |i - j| \right] \quad (1.39)$$

Now the final sum can be evaluated over two regions to eliminate the absolute values (similar to Eq. 1.33):

$$\sum_{i=1}^n \sum_{j=1}^n |i - j| = \sum_{i=1}^n \sum_{j=1}^{i-1} (i - j) + \sum_{i=1}^n \sum_{j=i+1}^n (j - i) \quad (1.40)$$

These sums evaluate to a total of  $\frac{n^3 - n}{3}$  and Eq. 1.39 becomes:

$$\frac{1}{n^2} \sum_{i=1}^n \sum_{j=1}^n \langle \beta(t + i\Delta t) \beta(t + j\Delta t) \rangle = B^2 + \frac{C^2}{3} \left( \frac{\tau}{\Delta t} - \frac{\Delta t}{\tau} \right) \quad (1.41)$$

If  $\tau \gg \Delta t$  then a similar form for the Allan variance above is recovered:

$$\sigma_\tau^2 = \frac{A^2 \Delta t}{\tau} + B^2 + \frac{C^2 \tau}{3 \Delta t} \quad (1.42)$$

### 1.5.4 Single Sensor Discussion

In a real measurement of the Allan variance, there is typically not an ensemble of sensors to average over. Instead the Allan variance is evaluated by sampling a single sensor at different times. In this case, the definition of the Allan variance becomes:

$$\sigma_{\tau}(M)^2 = \frac{M}{M-1} \left[ \frac{1}{M} \sum_{i=1}^M \Omega_{\tau i}^2 - \left( \frac{1}{M} \sum_{i=1}^M \Omega_{\tau i} \right)^2 \right] \quad (1.43)$$

with

$$\Omega_{\tau i} = \frac{\Delta t}{\tau} \sum_{j=1}^{\tau/\Delta t} \Omega(t_i + j\Delta t) \quad (1.44)$$

where  $M$  is the number of samples used in  $\Omega_{\tau i}$ , which is the sample output measured for duration  $\tau$  at time  $t_i$ . The prefactor  $\frac{M}{M-1}$  accounts for the fact that subtracting the mean  $\bar{\Omega}_{\tau i}$  uses one degree of freedom. This is exactly equivalent to Bessel's correction for the unbiased sample standard deviation.

Using a time series rather than an ensemble average is potentially problematic for the case of bias drift noise. Discussed above is the assumption that the drift term is constrained over sufficiently long times. If the time interval between each of the  $M$  sample is long compared to this "drift reset" time, then it is reasonable to assume that the drift noise is uncorrelated and the time series is equivalent to an ensemble average. However, if the times are not so long, then the interpretation of the drift signal becomes less clear since noise may be correlated between samples. It is worth noting the time-series method of Allan variance remains a useful experimental characterization of drift effects and is conventionally used this way.

In the next chapter, I will introduce the atomic physics techniques used in the UVA atom-based gyroscopes, survey influential and current atom interferometer gyroscopes, and summarize the interferometer methodology and rotation measurement.

## Chapter 2

# Techniques and Previous Work

In this chapter, the atomic physics techniques, experimental method, and proof of concept rotation measurement will be presented. This chapter aims to give the reader enough information to understand the techniques and challenges presented later.

### 2.1 Bose-Einstein Condensation

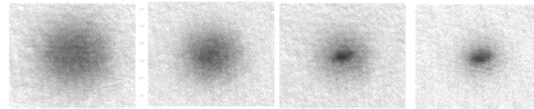


FIGURE 2.1: **Absorption images of the final stages of BEC condensation.** The photos demonstrate the final stages of radio frequency (RF) evaporation in BEC production.

In 2001, Carl Wieman, Eric Cornell, and Wolfgang Ketterle received the Nobel Prize in Physics for producing a new phase of matter: the Bose-Einstein Condensate (BEC). A BEC is formed from a low density gas of bosons when they are cooled (at UVA, around 100 nK) close to absolute zero. These conditions cause nearly all of the bosons to occupy the lowest available energy state, resulting in a macroscopic occupation of the corresponding wavefunction. This allows us to probe quantum mechanical behavior macroscopically through atom interferometry using a BEC. Although atom interactions

can have significant effects, the BEC used in this work is in a low-density regime where interactions can be ignored with reasonable accuracy. BEC production for the work in this dissertation is identical to previous work in [21–23].

## 2.2 Atom Interferometry

Atom interferometry, similar to optical interferometry, uses the wave-like properties of matter to measure phase shifts along different paths. For applications in inertial navigation, these phase shifts allow us to calculate important inertial quantities, such as accelerations and rotations. This technique requires the coherent splitting and recombination of the matter-waves. I will focus on the broadly used Bragg splitting technique that serves as the optical analog of mirrors and beam splitters for matter-waves in the instruments described in the rest of this dissertation.

### 2.2.1 Bragg Splitting

Bragg splitting (see Figs. 2.2 and 2.3) requires an off-resonant laser aligned on a matter-wave packet with a mirror retro-reflecting the light back. The laser light can be tuned such that the packet simultaneously absorbs and emits a photon in the same direction, giving it a momentum kick. Each photon gives the packet an  $\hbar k$  kick, totaling a  $2\hbar k$  kick in along the Bragg laser field in our experiment. By symmetry, the opposite is equally likely so our wave packet separates into two packets each with a momentum of  $2\hbar k$  [24, 25]. Higher momentum kicks (i.e.  $4\hbar k$ ,  $6\hbar k$ , etc.) can be induced by increasing the intensity of the Bragg beam. A further explanation of this method in the context of the rotation sensors discussed in this dissertation is in section 2.4.

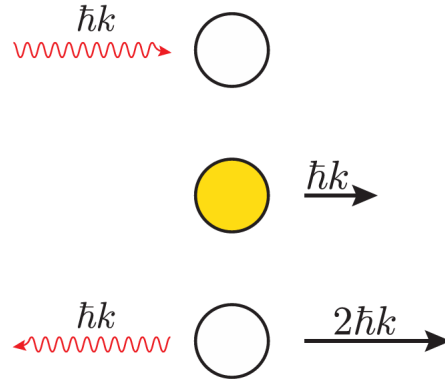


FIGURE 2.2: **Cartoon of Bragg splitting.** An off resonant standing wave laser comes in from the left and our atom wave packet absorbs a photon. Simultaneously, a mirror placed on the right retroreflects the initial light back on to the wave packet and causes the spontaneous emission of a photon in the direction of the absorbed photon. This gives the wave packet a  $2\hbar k$  kick toward the right. Figure taken from [23]

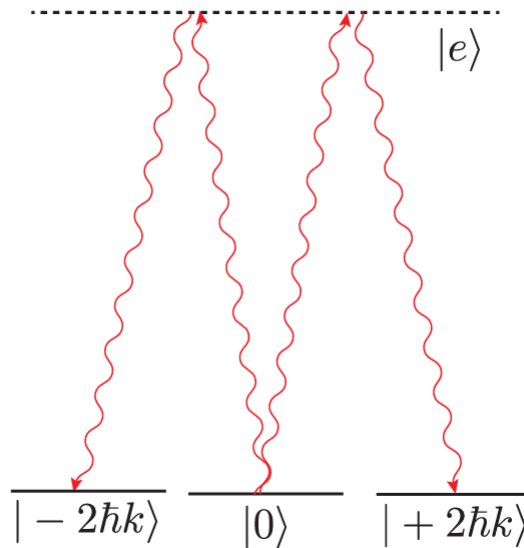


FIGURE 2.3: **Bragg splitting state diagram.** Shining an off-resonant beam on to atoms in the rest state,  $|0\rangle$ , causes a two-photon transition where a photon is simultaneously absorbed and emitted, causing the atoms to move through a virtual excited state,  $|e\rangle$ , and populate  $|\pm 2\hbar k\rangle$  states equally. Figure taken from [23]

### 2.2.2 Atom Interferometer Rotation Sensors

For over two decades now, physicists have been creating laboratory-scale Sagnac atom interferometer sensors. The first was an experiment performed at Stanford University and has set the sensitivity standard for future experiments [26, 27]. This experiment used two Cesium thermal beams launched horizontally and counter-propagating, to cancel common mode noise and reduce sensitivity to linear accelerations. In addition, this sensor used a different atom interferometry technique: two-photon stimulated Raman transitions to transfer momentum between the Cs ground states and perform the dividing, reflecting, and recombining needed for interference. They reported a short-term sensitivity of  $6 \times 10^{-10}$  rad/s at 1s integration times. A few years after this measurement, long term stability was measured for this experimental apparatus using an area reversal technique to cancel systematic effects. They report a bias stability of less than  $96 \mu\text{deg/hr}$  with a  $T^{-1/2}$  stability to 4 hours [28].

Currently, both in industry and academia, researchers are continuing to make progress on fieldable sensors using free space approaches. Imperial College London is making strides toward fieldable atom interferometer accelerometers [29] and applying those techniques to rotation sensing. They plan to use a two-axis accelerometer, with ultra cold atoms launched in a moving molasses to produce a gyroscope that can measure rotations in all three cardinal axes [30]. Results have not been published on this work or the field test of the atom accelerometer. In [12], the SYRTE 2018 gyroscope has a reported sensitivity of  $3 \times 10^{-8}$  rad/s at 1s integration times and bias stability of  $3 \times 10^{-10}$  rad/s with an interrogation time of 167 minutes. This is considered at the time of that report to be the leading industry atom based gyroscope. There have been major advancements since [12] was published in 2020. One company making ripples in the field is VectorAtomic. Over the past few years since their founding, they have been creating compact, atom based, devices that can build out an entire IMU. Recently, they

tested the accelerometer component and measured local gravity to a performance comparable with strategic grade accelerometers ( $0.1\text{-}1 \mu\text{g}$ ). [31] VectorAtomic, in collaboration with Honeywell Aerospace, submitted their gyroscope to the Defense Innovation Unit (DIU) for launch to test its capabilities in space. [32] Data from this test launch has not been published yet.

While free space approaches have been tested in the field and can demonstrate enhanced stability and sensitivity compared to classical sensors, these devices are still too large and complex for use in an inertial navigation system. These devices rely on measurements while the atoms are in free fall, so to increase the sensitivity further (i.e. Sagnac area), the atoms must be allowed to fall further, thus creating a bigger apparatus. This difficulty ushered in a wave of new ideas using trapped atoms.

Sagnac atom interferometers using trapped atoms have been demonstrated using an atom chip [33], optical trapping [34], and magnetic trapping [35–38]. The apparatuses at UVA use magnetically trapped atoms and this method will be described in the next section. An experiment at Los Alamos National Laboratory (LANL) deserves special mention. As part of the DARPA Atom-Photonic Integration (A-PhI) program, LANL developed a Sagnac interferometer using a moving optical trap to support the atoms against gravity and Bragg splitting of a BEC. They have been able to achieve long term stability out to 10,000 s and a Sagnac area of  $0.8 \text{ mm}^2$  [34]. The LANL and UVA trapped atom instruments have demonstrated successful control atom trajectories. This has yielded future compact apparatus designs and that can implement techniques to improve the stability [39]. However, these trapped atom experiments have not surpassed the sensitivity of the Stanford Cs beam experiment.

## 2.3 Time Orbiting Potential (TOP) Trap

The gyroscopes developed at UVA use a magnetic trap to confine the BEC weakly to allow the atoms to move and enclose an area and support them against gravity. This trap is produced using six coils with AC currents. The TOP trap is composed of a rotating bias field in all three cardinal directions and a spherical quadrupole field. The rotation of the bias field is faster than the atoms can move spatially, but slow enough compared to the Larmor frequency so the atomic spins follow the field adiabatically. The atoms maintain their spin state and experience a time averaged potential from the TOP fields,  $U_B = \mu \langle |\mathbf{B}| \rangle$ . In the UVA instruments, the quadrupole field oscillates synchronously with the bias field which produces a constant force at the center of the trap to support the atoms against gravity [40]. The rotating bias field has the following form:

$$\mathbf{B}_0 = B_0(\sin \Omega_1 t \sin \Omega_2 t \hat{\mathbf{x}} + \cos \Omega_1 t \sin \Omega_2 t \hat{\mathbf{y}} + \sin \Omega_1 t \hat{\mathbf{z}}) \quad (2.1)$$

The spherical quadrupole field has the following form:

$$\mathbf{B}_q = B'_1 \left( -\frac{1}{2} x \hat{\mathbf{x}} - \frac{1}{2} y \hat{\mathbf{y}} + z \hat{\mathbf{z}} \right) \sin \Omega_1 t \quad (2.2)$$

These fields are produced by function generators set such that  $\Omega_1 = 10$  kHz and  $\Omega_2 = 1$  kHz. The signals are amplified by commercial audio amplifiers and sent to the coils to produce the fields in vacuum.

The total potential is:

$$U_{tot} = \mu \langle |\mathbf{B}| \rangle + mgz \quad (2.3)$$

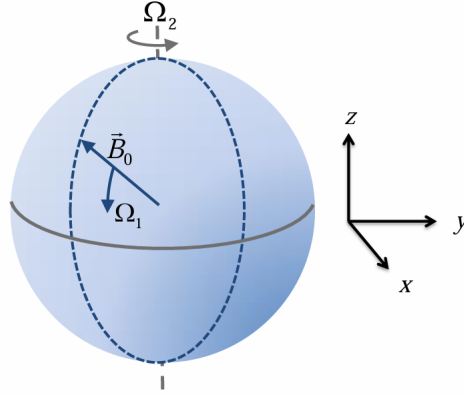


FIGURE 2.4: **AC bias field cartoon.** The bias field rotates along  $z$  at  $\Omega_1$  and the dashed plane rotates about  $z$  at  $\Omega_2$ . Figure taken from [21]

and after time averaging [21, 23]:

$$U_{tot} = \mu B_0 + mgz - \frac{1}{2}\mu B'_1 z + \frac{1}{2}m\omega^2(\rho^2 + \lambda z^2 + 2\gamma xy) + \text{higher order terms} \quad (2.4)$$

with

$$\rho^2 = x^2 + y^2 \quad (2.5)$$

$$\omega = \omega_x = \omega_y \quad (2.6)$$

$$\lambda = \frac{\omega_z^2}{\omega^2} \quad (2.7)$$

We can tune our fields such that  $mgz = \frac{1}{2}\mu B'_1 z$  causing these terms to cancel. This has the physical effect of supporting the atoms against gravity and not allowing them to sag or fall. We can control the phase between the X and Y function generators so that  $\gamma \approx 0$  (see section 3.4.3 for more information on this term and its physical effect). With these terms eliminated and ignoring higher order terms, we have the form of a cylindrically harmonic potential with a bias field term  $\mu B_0$ .

## 2.4 Method and Previous Work

### 2.4.1 Experimental Method

Our atom interferometer approach was presented in [23, 37], and is summarized here. A Bose condensate of  $10^4$   $^{87}\text{Rb}$  atoms is produced in a cylindrically symmetric magnetic trap with harmonic oscillation frequency  $\omega$  in the horizontal  $xy$  plane. An off-resonant standing-wave laser with wave number  $k$  is applied to the condensate and, via the Bragg effect, splits it into two packets traveling with velocities  $\pm v_B \hat{x}$  for  $v_B = 2\hbar k/m$  [24, 25]. The packets move in the trap until they come to rest at radius  $R = v_B/\omega$  and time  $t_1$ . An orthogonal standing wave then splits the atoms into four packets with velocities  $\pm v_B \hat{y}$ . Using these first two splits, we create a coupled two-level system where all of the atoms go from a rest state  $|0\rangle$ , to an equally likely symmetric state  $|+\rangle$ , with velocities  $|\pm v_B\rangle$ :

$$|0\rangle \rightarrow \frac{1}{\sqrt{2}} [ | +v_B\rangle + | -v_B\rangle ] \equiv |+\rangle \quad (2.8)$$

The harmonic potential causes all four packets to move in circular orbits; the atom density is low enough that the packets can pass through each other with negligible effect. If there are rotations in the system, there will be a phase shift,  $\phi$ , and the wavefunction,  $|\psi\rangle$ , will time evolve, up to some overall phase:

$$|\psi\rangle = \frac{1}{\sqrt{2}} ( | +v_B\rangle + | -v_B\rangle ) \rightarrow \frac{1}{\sqrt{2}} ( | +v_B\rangle + e^{i\phi} | -v_B\rangle ) = \cos(\phi/2) |+\rangle + \sin(\phi/2) |-\rangle \quad (2.9)$$

where the anti-symmetric state,  $|-\rangle$ , is defined as:

$$\frac{1}{\sqrt{2}} [ | +v_B\rangle - | -v_B\rangle ] \equiv |-\rangle \quad (2.10)$$

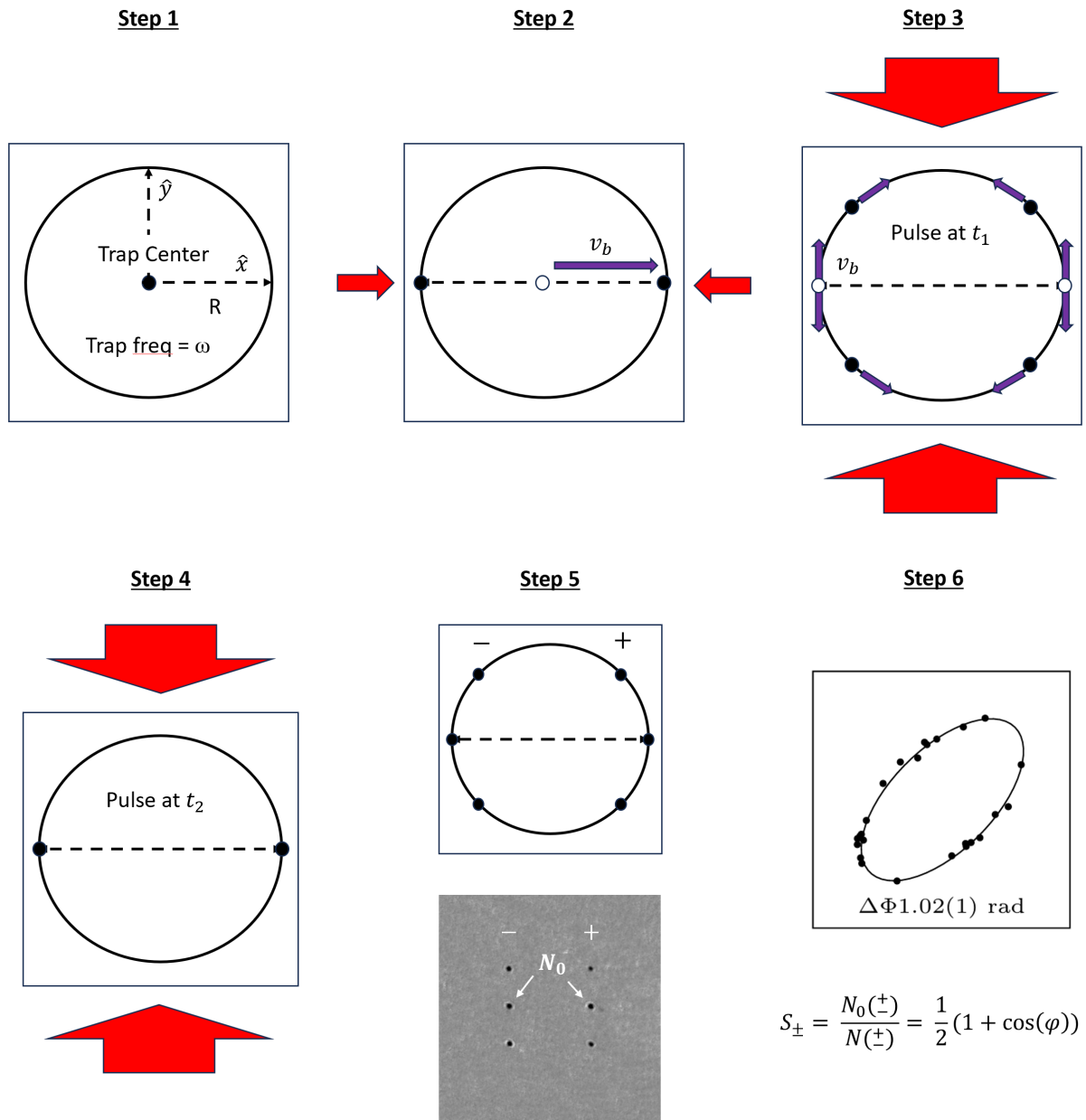


**FIGURE 2.5: Cartoon detailing interferometer experimental method and the Sagnac phase relationship to the interferometer signals.** In the case of the proof of concept experiment presented in this chapter,  $R = 0.2$  mm,  $\omega = 10$  Hz, the Sagnac area is  $A = 0.5$  mm<sup>2</sup>, and the atoms only orbit one time. The simulated interferometer data is in [23] and image taken by E. Moan. Furthermore, a video of the experimental procedure can be found in the supplementary materials of [37]

After one or more full orbits, at time  $t_2$ , the  $y$  Bragg beam is applied again, which produces two interferometer outputs at  $x = \pm R$ . The recombination pulse transforms  $|\psi\rangle$  to:

$$|\psi\rangle \rightarrow \cos(\phi/2) |0\rangle + \sin(\phi/2) |-\rangle \quad (2.11)$$

We can relate the phase shift (due to both noise and rotations),  $\phi$ , to the interferometer outputs by counting the number of atoms in  $|0\rangle$  (this is  $N_0$  in Fig. 2.5) and the total number of atoms in both  $|0\rangle$  and  $|-\rangle$  (this is  $N$  in Fig. 2.5). The interferometer outputs,  $S_{\pm}$ , are defined and related to the phase by:

$$S_{\pm} = \frac{N_0(\pm)}{N(\pm)} = \cos^2(\phi/2) = \frac{1}{2} [1 + \cos \phi] \quad (2.12)$$

We observe both outputs, via absorption imaging after a short time-of-flight delay. Fitting each packet to a Gaussian function allows us to obtain the number of atoms. We extract the differential phase by plotting  $S_{\pm}$  against each other and fitting the points to an ellipse [41].

It is worth noting here that the measurement is a differential phase, not an absolute phase. In Chapter 1, the Sagnac phase was derived as:

$$\phi_{Sagnac} = \frac{2m}{\hbar} \Omega \cdot A \quad (2.13)$$

However, this phase describes a single packet traveling around a circle with an area,  $A = \pi R^2$ . In our system, we have two interferometers each with two packets. In order to analyze the results of our experiment, we rely on measuring a differential phase between both interferometers because we are using two interferometers. This allows us to cancel common mode noise present in both interferometers that would mask the signal of just one of the interferometers. The Sagnac phase above is for a single wave

packet but each of our interferometers uses two packets. That can be denoted by its own differential phase,  $\Delta\phi$ :

$$\Delta\phi_{-,+} = \phi_1 - \phi_2 = \frac{4m}{\hbar}\mathbf{\Omega} \cdot \mathbf{A} \quad (2.14)$$

Where  $-, +$  refers to the interferometer (see Step 5 in 2.5) and  $\phi_{1,2}$  refers to the phase from the two individual packets for a single interferometer. A factor of two is included because the phase induced by traveling in the opposite direction will be negative so, after taking a difference, the phases will add. This differential phase for a single interferometer is not what we measure. To characterize a dual interferometer, we need to take an additional differential phase for the entire system,  $\Delta\Phi$ :

$$\Delta\Phi = \Delta\phi_- - \Delta\phi_+ = \frac{8m}{\hbar}\mathbf{\Omega} \cdot \mathbf{A} = \frac{2m}{\hbar}\mathbf{\Omega} \cdot \mathbf{A}_{eff} \quad (2.15)$$

This introduces yet another factor of two and now accounts for all four packets. The Sagnac areas cited later will be an effective area,  $A_{eff} = 4An$ , where  $A$  is the area of the circle the clouds enclose and  $n$  is the number of full orbits. This description accounts for the four packets and multiple orbits.

## 2.4.2 Rotation Measurement Summary

The results summarized in this section can be found in [23, 37]. The experiment required being able to rotate a 10 ft. by 5 ft. optics table while performing the interferometer measurement. This was accomplished by floating the optics table so it could move a small amount freely while being pushed on by a linear actuator. The actuator was activated before the first Bragg pulse and continued at a constant rate until after the interference measurement. The results of the experiment in Fig. 2.6, demonstrate a rotation measurement with the error bars corresponding to a sensitivity of  $8 \times 10^{-5}$  rad/s

which is on the order of the Earth's rotation rate of  $7.3 \times 10^{-5}$  rad/s or 15 deg/hr. These may seem small to our senses but the sensitivities achieved by modern optical gyroscopes are several orders of magnitude smaller than this sensitivity. Furthermore, the important bias stability was not evaluated in this experiment.

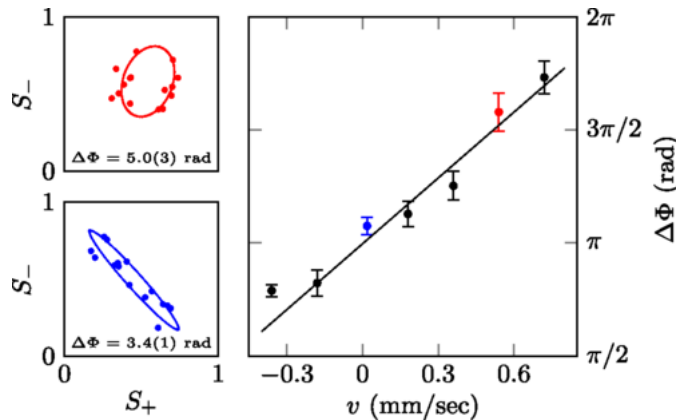


FIGURE 2.6: **Rotation sensing data plot.** **Left:** are characteristic data points for the graph on the right. These consist of no less than 10 individual interferometer signal measurements plotted against each other and then fitted to an ellipse to extract the differential phase  $\Delta\Phi$  between the interferometers. **Right:** Linear dependence of the differential phase on the rotation rate of the table. Figure taken from [37]

### 2.4.3 Instrumentation and Difficulties

The apparatus used in the rotation measurement was detailed in [42], and it forms the basis for the new work here. It consists of a vacuum system with two chambers connected by a differential pumping tube. The first chamber is a cylindrical glass cell where a magneto-optical trap (MOT) of  $10^9$   $^{87}\text{Rb}$  atoms is produced. The atoms are then loaded into a spherical DC quadrupole trap produced by an anti-Helmholtz coil pair. This coil pair is mechanically translated to carry the atoms into the second chamber. [43] There, they are positioned at the center of a magnetic coil structure producing a time-orbiting potential (TOP) trap [44]. A Bose-Einstein condensate (BEC) is produced

using the RF evaporation cooling technique. After the atoms are loaded into a weak TOP trap, the interferometer sequence is performed.

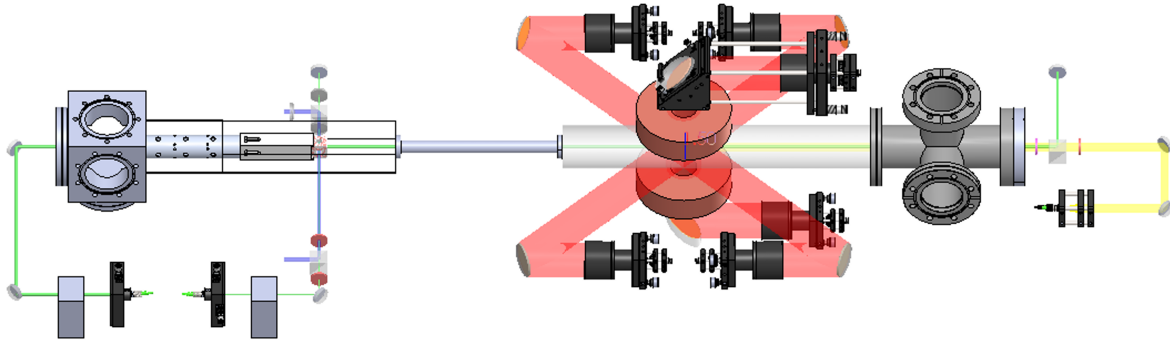


FIGURE 2.7: **3D CAD drawing of previous vacuum system.** The atoms are confined in a MOT and undergo optical pumping in the right most glass chamber. The atoms are then translated to the glass chamber with the cube coil structure where they will be Bose condensed and Sagnac interferometry will take place. The yellow beam is for optical pumping, the green beam is the y Bragg beam, and the blue beam is the x Bragg beam. Figure from [23]

The original apparatus had some shortcomings that limited the interferometer performance and reliability. First, the six trap coils were mounted on the faces of a 2-cm boron nitride cube, which was fixed to the end of a 25-cm arm attached to a vacuum flange. The entire assembly was in vacuum, and the long arm provided a thermal conductance of about 80 mW/K. [21] The coils dissipated power of about 10 W, leading to temperature variations of a few tens of K. These variations degraded the stability of the trap, resulting in phase noise for the interferometer [45] and requiring experimental adjustments on the 1-hr time scale. Second, optical access for one of the Bragg lasers was achieved by passing the beam along the axis of the 2-m long vacuum system, including through a 9-mm diameter hole in the coil-mounting arm and the 12-mm diameter tube connecting the two chambers. This severely restricted the adjustability of the beam alignment. Third, the coil geometry introduced tilts and anharmonicity to the trap potential, which resulted in the wave packets failing to overlap after more

than one orbit. In the next chapter, I will detail a new, laboratory sized instrument that addresses these challenges and the accompanying results.

## Chapter 3

# Lab-Scale Apparatus

### 3.1 Instrumentation

The challenges from the previous apparatus were thermal instability, optical access for Bragg splitting, and anharmonicities due to the coil geometry. The new apparatus discussed in this chapter uses the same configuration as [42] but with an updated science cell to compensate for these problems. The experimental method for atom interferometry and rotation sensing is unchanged from [23, 37] and this apparatus has better heat sinking, quality windows for Bragg beam access, bigger coils for reduced anharmonicity, and can support an atom chip (discussed in greater detail in section 4.1.4).

In Fig. 3.1, the gray component at the top of the image is a six inch conflat flange with water-cooling connectors. The white components are Shapal forms for the coils, which are represented in copper color. There are six coils altogether, of which five are visible. The sixth is enclosed by the rectangular Shapal base above the blue plate, which is a 1-mm-thick silicon wafer used as a mirror for imaging. This Shapal base can also serve as a holder for an atom chip. The four horizontal coils have 64 turns of AWG 20 copper wire with Kapton insulation. The average radius is 14 mm, and the average distance from the fixture center is 26 mm. The two vertical coils have 26 turns of AWG

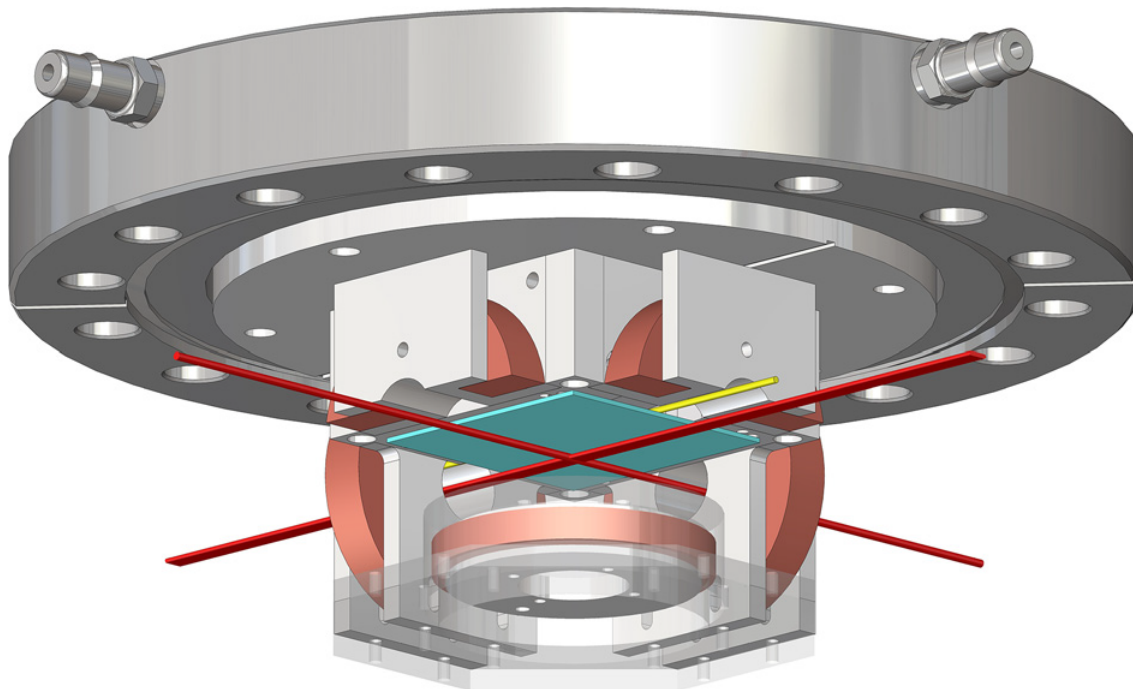


FIGURE 3.1: Cutaway view of coil fixture and cooling flange in the updated science chamber.

20 wire, an average radius of 15 mm, and average distance of 14 mm. The yellow wire is an antenna for RF evaporative cooling. The red beams show the paths of the two Bragg lasers. Atoms are trapped at the center of the fixture, about 2 mm from the mirror surface.

### 3.1.1 Assembling the Science Chamber

In the process of assembling the science chamber as designed, there were a number of technical challenges that were overcome. Initially, ceramic screws were used to assemble the entire Shapal coil structure. However, ceramic screws are very fragile and broke easily even while using a torque screwdriver to control the force on the screw during the assembly. Metal screws with spring washers were implemented in the assembly of the system. Next, winding the coils individually and then attempting to assemble the entire structure did not work. Once the horizontal coils were fully wound, access

to the holes for one of the two screws used to secure the coil to the mirror base was obscured. This problem meant that all four of the coils would need to be wound while the horizontal coil structures are already attached by screws to the mirror base. However, when winding the coils whilst attached by screws to the base, the metal screws would loosen as a result of the force applied to the coil structure during the process of winding the coils. In order to prevent this loosening, all four horizontal coil structures were screwed and epoxied to the mirror base before being wound.

Vacuum-safe Epo-Tek epoxies were used and cured using heat. To glue the horizontal coils structures to the base, Epo-Tek H77 epoxy was used due to its thermal conductivity of  $0.7 \text{ W/mK}$ . The epoxy was mixed according to the weight ratio of the two different parts and the mix was placed under vacuum. The vacuum was strong enough to pull air bubbles out of the epoxy mixture, creating a bubbly foam that reduced to a smooth mixture. While under vacuum, any air bubbles trapped are pulled to the surface and escape the epoxy mixture, ensuring minimum outgassing of trapped air during the vacuum bake. Extra caution was required when applying the epoxy because of its low viscosity. Each horizontal coil mount was individually glued to the base after screwing the mount down just far enough to be able to insert a small syringe in between the mount and the chip base. Once the epoxy was in place, the rest of the mount was screwed down and caution was taken so that no excess epoxy leaked from the sides or bottom of the horizontal structure and mirror base. Using a stainless steel Black and Decker convection countertop oven, the entire structure was baked for  $150^\circ\text{C}$  for 1 hour to cure the epoxy and whole process repeated for each horizontal coil. The cure temperature was monitored using a thermocouple.

Once all of the mounts were fully epoxied to the mirror base, the coils were wound with Accu-Glass Kapton wire and epoxied in place with Epo-Tek 353ND. This epoxy was much easier to work with but still required pulling vacuum on the mixture

to remove air bubbles. During coil winding, a small amount of epoxy was applied in between wire layers. At the end of winding the coil, the exterior of the coil was coated with epoxy and excess wire and a weight acted as a plumb bob to hold the wire in place while the epoxy cured. In order to cure the epoxy, current was applied through the coils and the temperature was monitored using a thermocouple. The same process was completed for the vertical coils. Small amounts of this epoxy were also applied to the tops of the screws holding the Shapal pieces together. Once the entire system was assembled and epoxied, it was washed in an ultrasonic bath.

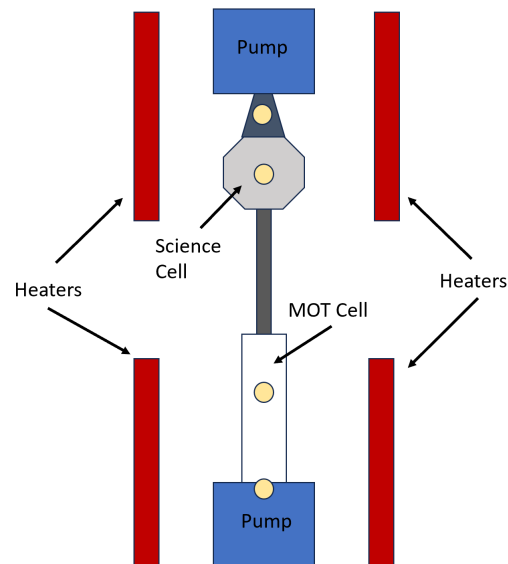


FIGURE 3.2: **Top down view of vacuum bake set up.** Yellow dots represent areas where thermocouples were applied.

Once the entire instrument was assembled, a vacuum bake out was done to ensure an ultra high vacuum for our experiment. In the process of producing steel, hydrocarbons are produced and trapped in the steel. Heating the steel to high temperatures while under vacuum allows us to remove contaminants from the steel production, in addition to water and other elements as a result of the system being exposed to our laboratory environment. Fig. 3.2 shows the general set up inside of a home-built oven with the vacuum pump out system, positioned near the MOT cell, and ion pumps located

on each end of the system. The vacuum pump out system consists of a multi-stage vacuum pumping system that consists of a roughing pump and a turbo pump. The heaters are long coils that current is cycled through on a duty cycle set by a function generator to ensure even heating. The experiment baked continuously for 30 days, reaching a maximum temperature of  $180^{\circ}\text{C}$  and a final pressure of  $10^{-8}$  torr. The epoxy limited the maximum temperature that could be used during baking. Once installed on the optical table with the ion pumps and titanium sublimation pump (TSP) running, a typical operation pressure is  $1.3 \times 10^{-10}$  torr on the MOT side and  $2.3 \times 10^{-11}$  torr on the science side. This difference in vacuum pressure between two sides is due to the Rb getters running constantly throughout data taking.

### 3.1.2 Water Cooling System

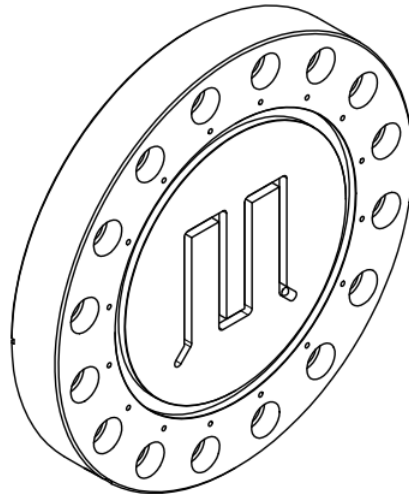


FIGURE 3.3: **CAD drawing of cooling flange.** The serpentine groove is the path for water cooling. There are tiny screw holes along the outside of a circular gland that contains a rubber O-ring to prevent water leaking.

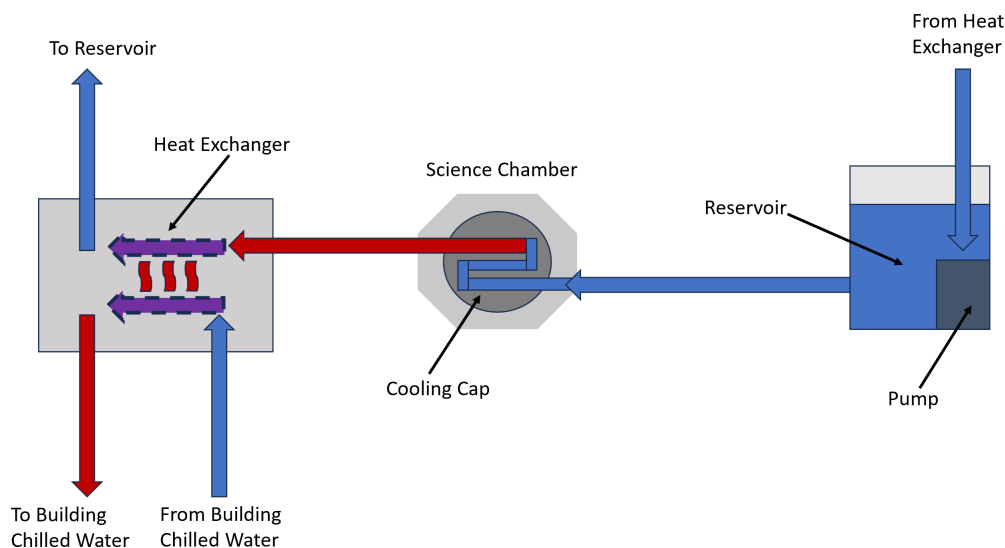


FIGURE 3.4: **Illustration of water cooling system.** Cold water is transported to the science chamber cooling flange from a submersible pump and reservoir. The water heats up as it passes through the flange, drawing heat away from the system. This warmer water goes through a heat exchanger where, in parallel, cold building water carries the heat away from the system, leaving cold water to return to the reservoir.

One critical improvement was the introduction of a water cooling system via a cooling flange and cap to draw heat away from the in vacuum coil structure. The cooling flange contains grooves to transport water through the flange with a cooling cap secured to the top of the flange. The cap is stainless steel, with a flat surface on both sides, and is secured to the flange via screws. Much work went into leak proofing the cap using an O-ring and silicone sealant. The entire system is closed from the building water cooling loop and uses a heat exchanger to cool the water. To prevent growth of unwanted microbes, over-the-counter distilled water and 99% Isopropyl alcohol are used.

### 3.1.3 Imaging and Bragg Optics

Another major improvement on the previous instrument is the Bragg optical access. The previous system used a glass science cell with only one horizontal pair of windows. The new apparatus uses an octagonal chamber with four windows providing optical access for two horizontal beams to cross the inside of the chamber. The windows have an anti-reflective coating and custom copper gaskets that provide a  $3^\circ$  tilt so the small amount of reflection does not disrupt the Bragg splitting fidelity. The laser diagram for producing and distributing the light required for the apparatus can be found in Chapter 4, Fig. 4.7. This system omits the use of a push beam found in the referenced figure.

All of the light required for the instrument on the science side is fiber-coupled using a network (see Fig. 3.5) of polarization-maintaining optical fibers (Thorlabs PN780R5A2). This network is designed with the ability to image and Bragg split along both horizontal directions to check wave packet overlap at different times when assessing the packet trajectories. The probe fiber has a single input and provides two outputs: the Z imaging (vertical imaging) system and the XY imaging (horizontal) system. The X Bragg fiber (green) has two inputs: one for the Bragg light and the other input for the probe light or, if aligning the retro-reflection of the Bragg beam, one can use the extra input to check the beam overlap by measuring the optical power using a power meter. The Y Bragg fiber (yellow) is analogous to the X Bragg fiber. Control to ensure the probe light and Bragg light are not on at the same time is handled by shutters and AOMs on the inputs of all of the fibers. The probe power is  $\sim 3$  mW per output. The X and Y Bragg power is  $\sim 1.5$  mW per output. The outputs of the X and Y Bragg fibers can be seen in a simple use case in Fig. 3.6.

Once the appropriate light is coupled into the fiber network, then the fibers are plugged in to their respective mounts. Starting with the horizontal imaging, we can image and Bragg split using the same beam collimation packages. The collimation

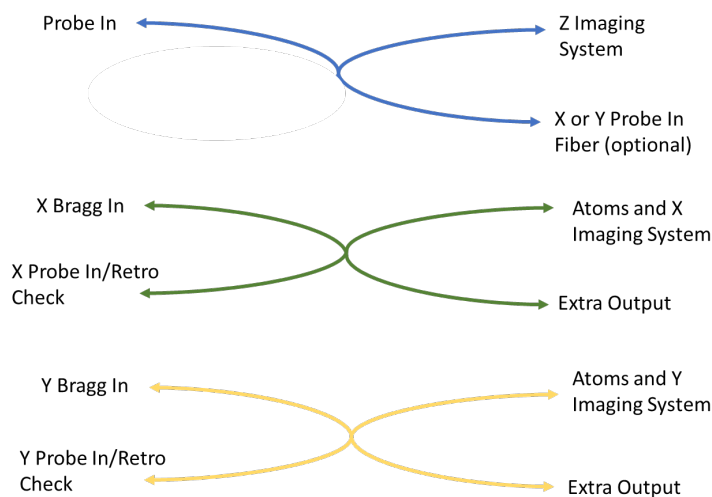


FIGURE 3.5: **Optical fiber map for the probe and Bragg beams.** The blue fiber is the probe fiber used for imaging the atoms in the vertical imaging axis and horizontal imaging axes. The green fiber is the X Bragg fiber. The yellow fiber is the Y Bragg fiber. Both the X and Y Bragg fibers can be configured to image and split along that direction.

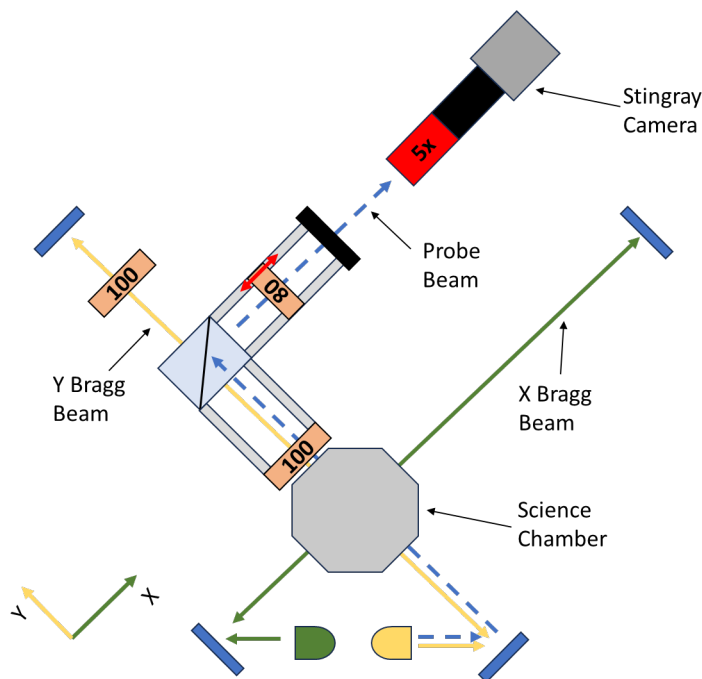


FIGURE 3.6: **Top down view of the horizontal imaging and Bragg splitting systems.** The orange boxes are lenses with the focal length in mm marked. The 80 mm lens is on a translation stage to aid in focusing for imaging. Not pictured: 60 mm lens in a 2 in lens tube placed behind 5x objective on the camera.

packages are mounted on a translation stage and the beams first encounter mirrors that have micrometers to repeatably adjust the angle of the beam. In Fig. 3.6, the instrument is set up to Bragg split and image along the Y direction and to Bragg split along X. This illustration is for simplicity and there is a separate identical cage system for the X direction that the Bragg beam can travel through. This system is modular and can be swapped in and out as needed for checking the the cloud overlap or imaging along the side. The camera used for side imaging is an Allied Vision Stingray F1-45 CCD camera.

The vertical imaging system (Fig. 3.7) only requires the probe light input. The light is fiber coupled in to a cage system that directs the light to the atoms and then back out to an Andor Zyla sCMOS camera. This is accomplished with the use of a window placed on the underside of the vacuum chamber and a mirror glued to the Shapal chip mirror base mounted vertically above the atoms. This imaging system is responsible for all of the interference data presented later in this chapter.

### 3.1.4 Drive Electronics

The magnetic fields in Eqs. 2.2 and 2.1, that lead to the harmonic potential (Eq. 2.4) begin as simple sinusoidal waves produced by function generators (Agilent 33210A). For the horizontal coils, the waveform required is a combination of  $\Omega_1 = 10$  kHz and  $\Omega_2 = 1$  kHz waveforms. In order to facilitate this complex waveform, analog multiplying chips (Analog Devices AD633) take the input from the function generators and multiplies the signals together to form the fields needed for the horizontal components of Eq. 2.1. The vertical coils do not have this same requirement and can be directly sent to the control box.

The waveforms arrive at the control box (see Fig. 3.8) where the amplitudes of the waveforms can be adjusted using the experiment software (Twitch) and a control

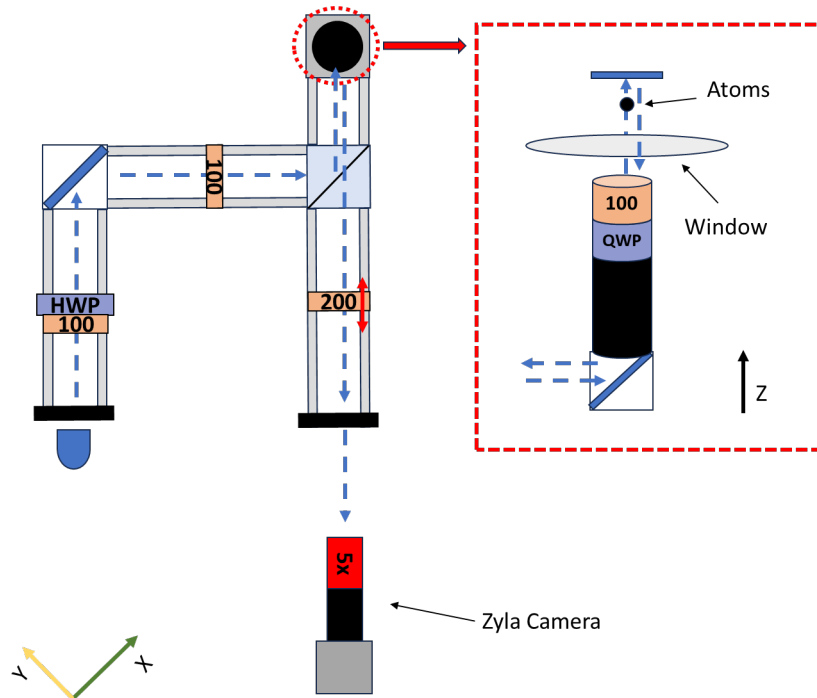


FIGURE 3.7: Top down view of vertical imaging system with cutaway in the z direction.

The light travels from the blue input on the left part of the cage through to a beam splitter where light is sent to the atoms through a lens tube mounted vertically (red dashed box) and the image of the atoms is reflected back out through the beam splitter to the camera. Not pictured: 90 mm lens in a 3.5 in lens tube placed behind 5x objective on the camera.

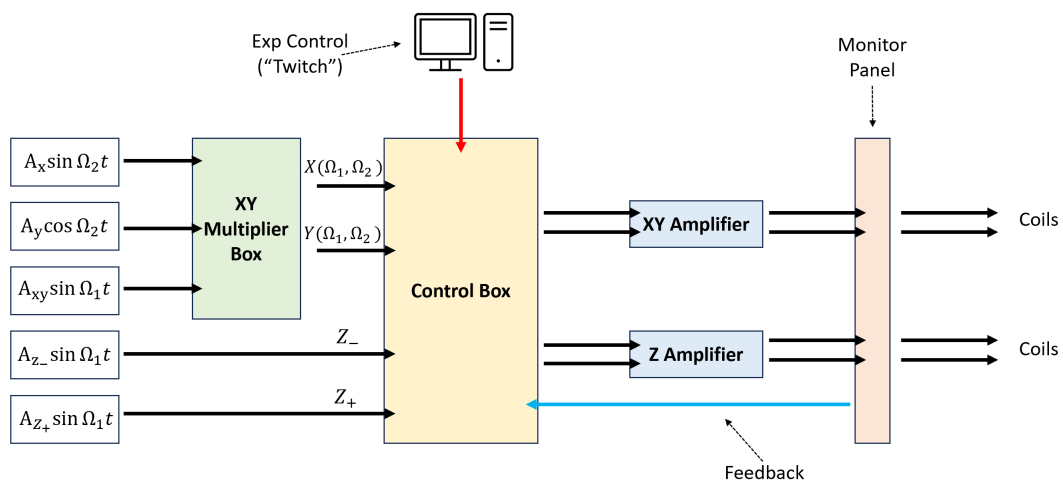


FIGURE 3.8: Block diagram of drive electronics system.

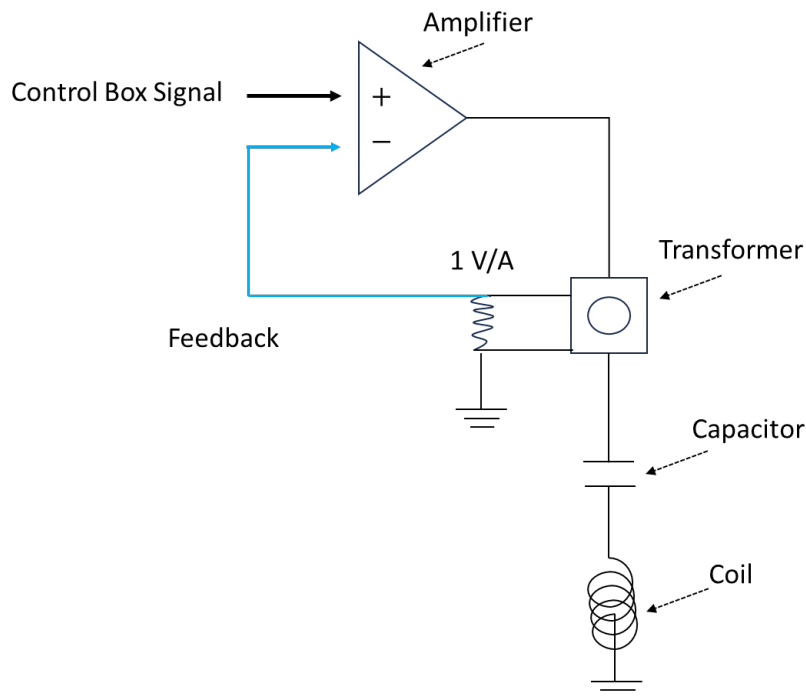


FIGURE 3.9: **Monitor panel electronics for one coil.** The current goes from the amplifier to a current sense transformer, that allows monitoring of the current and provides feedback to the amplifier. The current then goes to a capacitor that is part of an LC circuit with the capacitor selected to offset the inductance of the coil for the drive frequency.

system (ADWin) with several analog and digital channels. To change the amplitudes of the waveforms, they are multiplied by an analog voltage from ADWin using the same multiplier chips as above. The control box also contains analog switches to rapidly turn the signals on and off, controlled by a digital signal from ADWin.

This configuration has a feedback system [46] that passes the signal back through to the amplifiers. This design is to mitigate any changes to the waveform current and phase as these systems can experience drift. Once the signals leave the control box, they go to a pair of commercial audio amplifiers (QSC Audio RMX 850) that amplify the current amplitude of the waveforms from the control box. These amplified signals go to a monitoring panel (see details in Fig. 3.9) where they can be monitored using current sense transformers from Triad Electronics. This panel also serves as a throughput for

the feedback to go back to the control box, sends the current through a capacitor, and then on to the coil. The capacitor is selected to offset the inductance of the coil for the selected drive frequency.

## 3.2 Magnetic Field Characterization

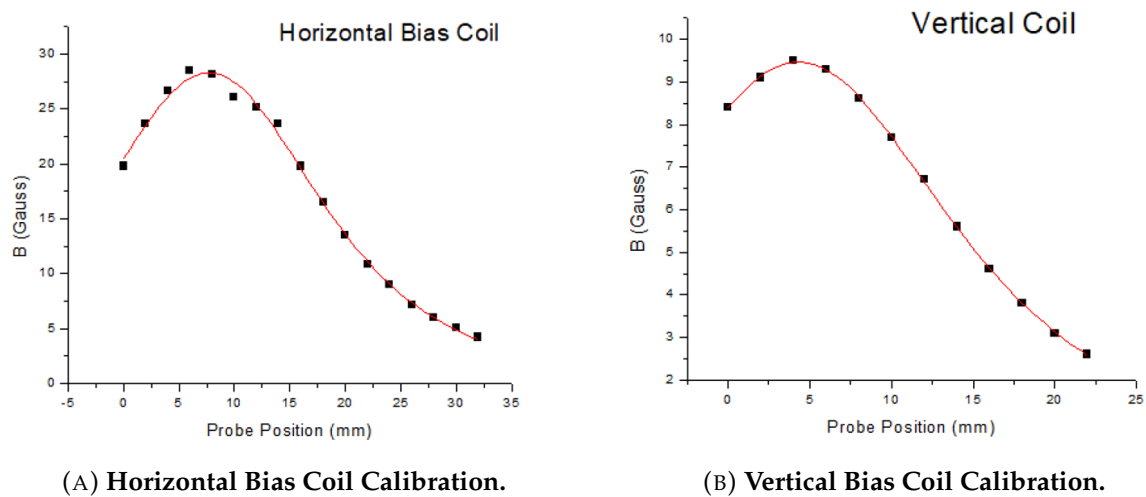


FIGURE 3.10: Magnetic Field Calibrations

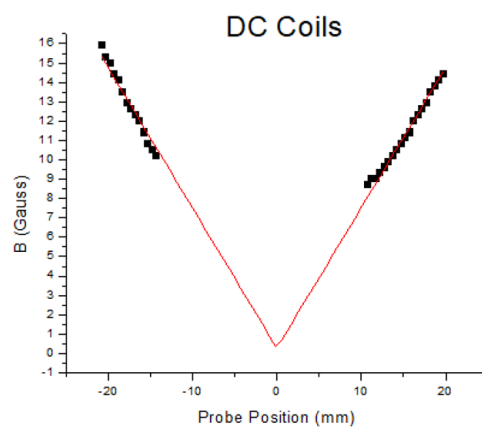


FIGURE 3.11: DC Coil Magnetic Field vs. Probe Position. The magnetic field was measured along the vertical axis as a function of the distance from the translation axis of the atoms (center of the bellows that connects the MOT chamber to the science chamber).

The bias fields were characterized before baking using a F.W. Bell 610 gaussmeter to measure the fields produced by the horizontal and vertical coils with 1 A of current. The probe is mounted on a translation stage with the position measured by a micrometer (shown in Fig. 3.10). The probe was pushed from outside of the coil, through the center of the coil (where the magnetic field is maximal), toward the location of the atoms. The field was measured in Gauss and recorded as a function of the position of the probe. In the location approximately where the atoms should be located while in vacuum for a horizontal coil pair,  $B_{xy} = 6.5 \text{ G/A}$  and for each single vertical coil  $B_z = 3.8 \text{ G/A}$ . The final guide bias amplitude is 15 G. In addition to the coils on the science side, the translating DC coil field that moves the atoms from the MOT to the science side was calibrated (shown in Fig. 3.11). Using both coils in an anti-Helmholtz configuration a magnetic field gradient,  $B'_{DC} = 270 \text{ G/cm}$ , is produced.

### 3.3 Thermal Characterization

Characterizing the thermal stability of the coil structure responsible for producing the TOP trap is important because changes in temperature affect the trapping potential. Thermal fluctuations can affect the trap in two ways. First, thermal expansion causes the coil geometry to change, which alters the magnetic fields and, therefore, the trapping potential. Since the magnetic field from a source varies inversely with distance,  $|(dB/dT)/B| \approx |(dl/dT)/l|$ , where  $B$  is the field magnitude,  $T$  is the temperature, and  $l$  is the fixture size scale. The relative size variation  $(dl/dT)/l$  is determined by the coefficients of thermal expansion for copper and Shapal, which are  $2 \times 10^{-5}$  and  $5 \times 10^{-6} \text{ K}^{-1}$ , respectively. The second effect is the change with temperature of the resistance of the copper wires, which alters the driving current. The trap drive electronics use a current-stabilization feedback loop to counter such effects, but the loop gain of

about 30 dB provides only a factor of 33 reduction [46]. The temperature coefficient for copper is  $4 \times 10^{-3} \text{ K}^{-1}$ , so the expected relative current variations are about  $10^{-4} \text{ K}^{-1}$ . The relative field variation is the same, so this resistance effect is expected to dominate over the thermal expansion effect.

Tests were performed to characterize the thermal conductance of the Shapal coil structure and cooling system. An initial set of tests were performed before the system was placed in vacuum. These were designed to test what torque should be used on the screws responsible for connecting the Shapal structure to the flange and if placing small sheets of indium between the Shapal structure base and the flange had any positive effect. This test was done using the flange attached to the water cooling loop, the Shapal base (that connects the coils and mirror holder to the flange), and a large resistor clamped to the base. The temperature was measured at each interface using a thermocouple and was monitored for several minutes. For a torque of 30 in-Lbs and no indium between the base and the flange, the measured thermal conductivity was 4.34 W/K between the base and the flange. For a torque of 30 in-Lbs and a 100 micron thick, 2 in<sup>2</sup> piece of Indium foil placed between the base and the flange, the thermal conductivity was measured to be 5.76 W/K, leading to a total estimated temperature change of about 2 K. Therefore, the trap potential is expected to be stable to approximately 1 part in  $10^4$ , which is similar to the amplitude stability of the function generators from which the current signals are sourced. A reminder that the previous instrument had a thermal conductivity of 80 mW/K leading to temperature variations of a few tens of K.

Once the coil assembly was installed and operating, in situ test was performed to measure the trap stability. The data in Fig. 3.12 shows coherent oscillations of a BEC along the vertical direction for almost 2 minutes indicating minimal heating that would induce changes to the TOP trap. These oscillations developed about 0.2 rad of phase noise after 100 s. This corresponds to a relative stability of  $10^{-4}$ , in agreement with

expectations based on the thermal analysis above. Atoms in the previous apparatus could only oscillate coherently for 25 s.

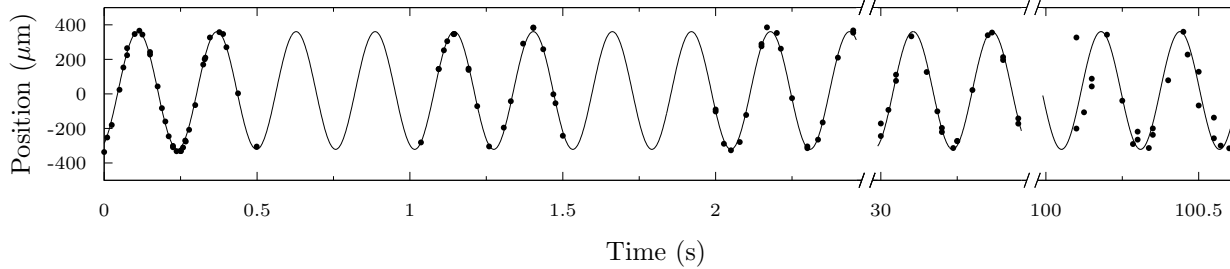


FIGURE 3.12: **Long Oscillations.** Data points show the central position of a single condensate as it oscillates vertically in the TOP trap. The curve is a single sinusoidal fit to the full data set, including points not shown at intermediate times. It can be seen that the atomic oscillations remain coherent up to a time of 100 s. The fitted frequency is 3.87 Hz.

## 3.4 Interferometer Method

There are several important steps in making an interferometer, most with the goal of obtaining circular trajectories and good overlapping of the atom packets during the course of moving through the trap. The important steps are listed below in detail, however it is worth noting that this process is not simple or linear. Meaning, some of the parameters are shared for these different sections and require tuning while considering several of these stages at once.

### 3.4.1 Limiting Residual Oscillations

Residual oscillations are collective oscillations that are caused by a small amount of momentum imparted on the atoms. These oscillations can come from a few different parts of the experimental process but the focus of this section will be on residual oscillations induced as a result of transferring the BEC from a tight DC quadrupole trap into the

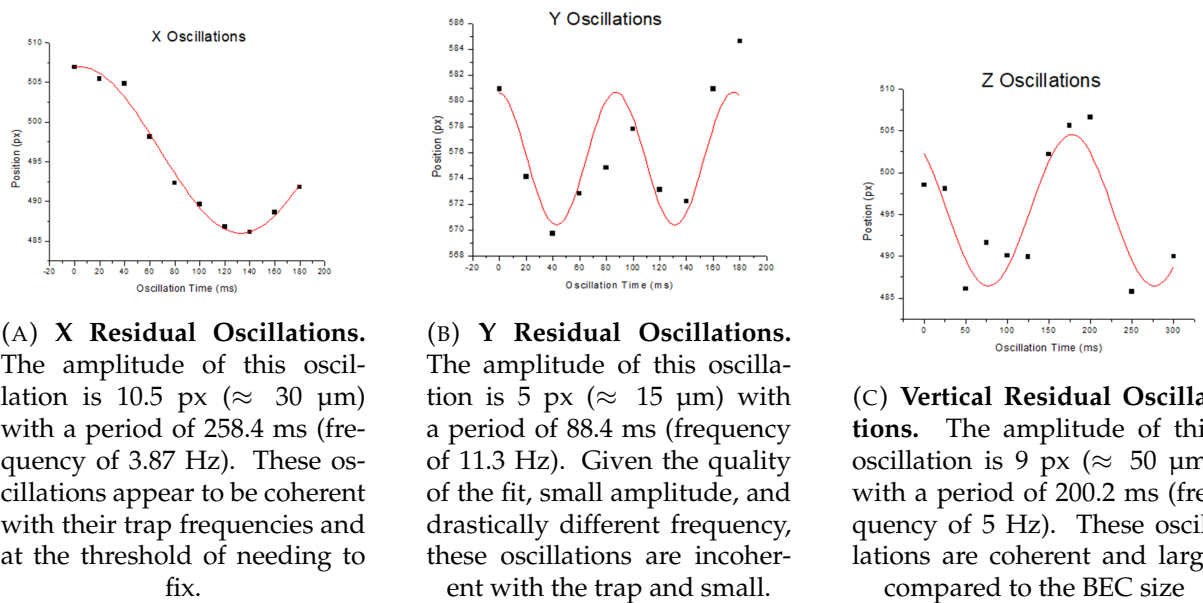


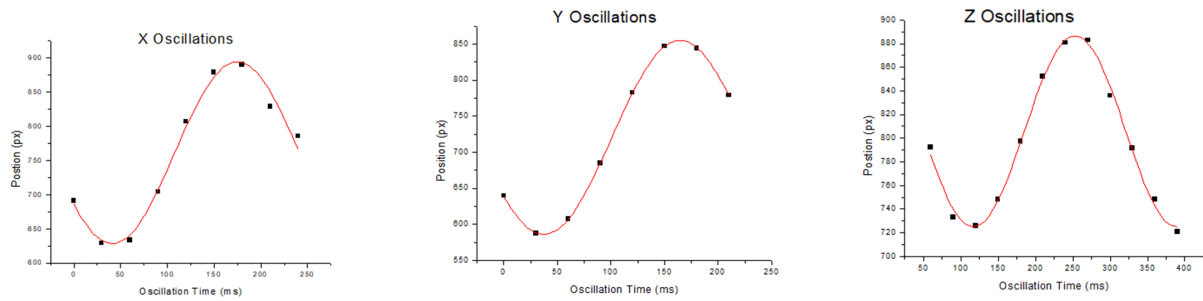
FIGURE 3.13: **Residual Oscillations.** The position of the BEC in camera pixels vs. oscillation time for a BEC in the weak trap.

weak, AC trap. It is necessary to evaluate residual oscillations because they can cause Bragg splitting to be inconsistent and difficulties evaluating trajectories for cancelling the cross term in the time averaged potential (see section 3.4.3). The procedure for loading the atoms into the weak trap has several stages, most of which are several seconds long. Several features at each stage must be checked. Residual oscillations are evaluated in all three cardinal axes by loading the atoms into one of the stages and adding a hold time before the pictures are taken on each axis. This hold time varies at each stage due to the span of the trap frequencies (for example, the first stage of the procedure, the atoms are in a 100 Hz trap and by the end they are in a much weaker trap around 3 Hz). In addition, residual oscillations can be coherent with the trap frequency, meaning they are approximately equal to the trap frequency, or incoherent with the trap frequency, meaning the atoms exhibit oscillatory behavior but not at the same frequency as the trap. Trap frequencies can be determined more precisely by the procedure outlined in 3.4.2.

Oscillations larger than about  $40 \mu\text{m}$  (about 2 times the BEC diameter) require correction. This correction is accomplished by minimizing oscillations at each stage of loading the atoms into the the final weak trap. This is done by adjusting the timing of the different procedure stages, reducing the time spent in a 60 Hz trap, and adjusting the current amplitudes during evaporation. In addition, careful attention is paid to aligning the tight trap with the weak trap. Initially, once the atoms are loaded into the weak trap and residual oscillations characterized, often the center of the weak trap is not in the same place as the tight trap. Traveling this distance can induce residual oscillations on the atoms. In order to reduce these types of oscillations, the translated DC quadrupole coils must be aligned with the weak trap center. This procedure involves changing the position of the translation track on which the large DC quadrupole coils are mounted, in addition to changing the distance between the DC coils. Typically, tight and weak trap alignment can be achieved within  $200 \mu\text{m}$ . Furthermore, vertical residual oscillations can be improved and managed when initially loading the atoms into the weak trap by paying close attention to their location and not allowing them to sag as a result of gravity from stage to stage. This sag is controlled by the AC quadrupole field produced by the vertical coils.

### 3.4.2 Trap Symmetry

Once the atoms are initially evaluated for residual oscillations and steps are taken to mitigate them, the horizontal field symmetry must be evaluated and symmeterized. The atoms must be loaded into a cylindrically symmetric waveguide in order to enclose a circular area. To evaluate the trap frequencies, Bragg splitting is done along X and Y respectively and the position of the BECs are recorded as a function of time and fit to a sinusoidal function (see Fig. 3.14). In order to change the frequency of the trap, the AC current amplitudes can be tuned to set  $\omega_x = \omega_y$ . To evaluate  $\omega_z$ , the atoms can be given



(A) **X Kicked Oscillations.** The amplitude of this oscillation is 133 px ( $\approx 0.5$  mm) with a period of 267.4 ms (frequency of 3.74 Hz).

(B) **Y Kicked Oscillations.** The amplitude of this oscillation is 135 px ( $\approx 0.5$  mm) with a period of 254.3 ms (frequency of 3.93 Hz).

(C) **Vertical Kicked Oscillations.** The amplitude of this oscillation is 81 px ( $\approx 0.45$  mm) with a period of 271.8 ms (frequency of 3.68 Hz).

FIGURE 3.14: **Kicked Oscillations.** The position of the BEC in camera pixels vs. oscillation time for a BEC in the weak trap.

a kick along the vertical direction by abruptly changing the AC quadrupole (similar to Fig. 3.12).

### 3.4.3 Cross Term Precession

Once the atoms are in a symmetric trap and not experiencing problematic residual oscillations at the trap center, one can notice the effect of the  $\gamma_{xy}$  term in Eq. 2.4. This cross term causes the principle axes of the trap to deviate from the X and Y axes determined by the Bragg beams. As a result, when atoms continue to oscillate after several periods, the direction of the oscillation eventually moves away from the Bragg axis. This behavior is referred to as precession and it is characterized by measuring the angle of the oscillations away from the original axis.

One method for reducing this term is to simply take pictures of Bragg split packets at their turning points close to the initial split and after three periods of oscillation. If this cross-term is large enough, the atom packets will not be co-located after three full periods. One can fit the BEC locations to a line and measure the angle between the initial split packets and the packets that have sloshed for about three periods. To

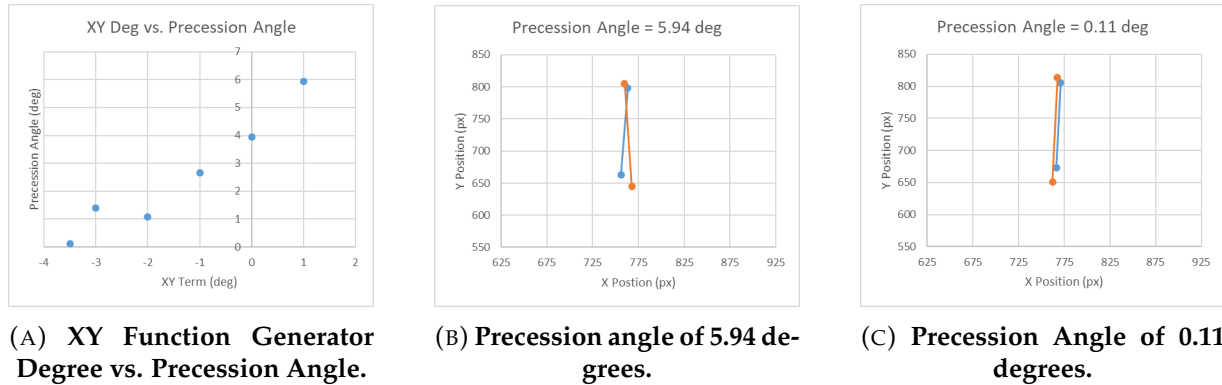


FIGURE 3.15: **Precession Figures.** Fig. 3.15a is a summary graph showing that changing the XY phase on the function generator decreases the precession angle. Figs. 3.15b and 3.15c have points represent the positions of the two separate packets (in pixels) for splitting close to the initial splitting time (blue) and after three periods (orange). A precession angle of 0.11 deg is as close to zero precession as we can get due to the accuracy of this method.

reduce this term, and thereby the angle between the two linear trajectories, the function generator that controls the phase between the X and Y rotating bias fields is adjusted. The precession angle in the following figures is defined by the angle between the linear trajectories of the split atoms from close to the initial split vs. three periods.

### 3.4.4 Trajectories

The most difficult part of optimizing the experimental process is obtaining symmetric horizontal trajectories with atom packets that overlap vertically as the packets travel throughout the trap. Adjusting the symmetries for the horizontal and vertical components require tuning different parameters that are coupled.

#### Trajectories in the Horizontal Plane

In the horizontal plane, the trajectories are determined by the trap frequencies, Bragg yaw angle, and the Y Bragg pulse time,  $t_1$ . Before arriving at the stage of analyzing the

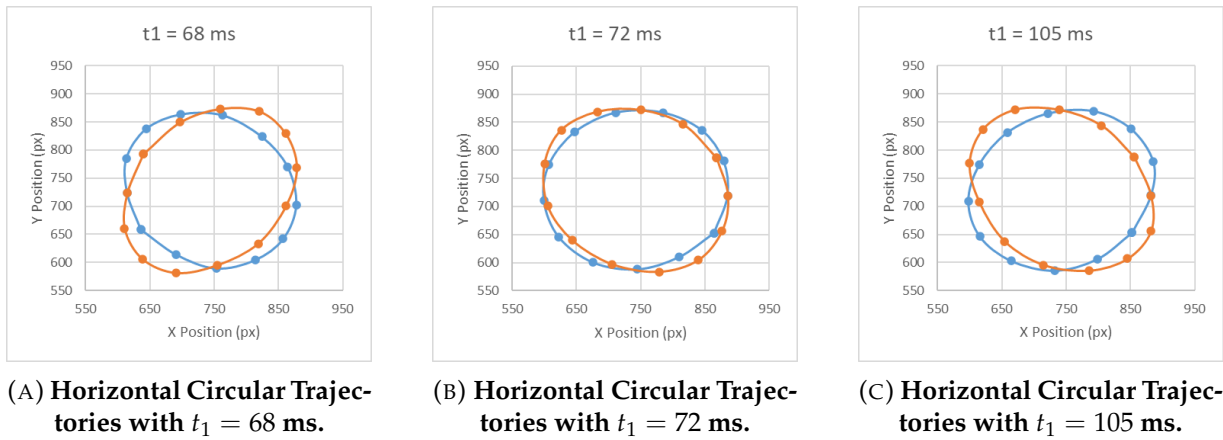
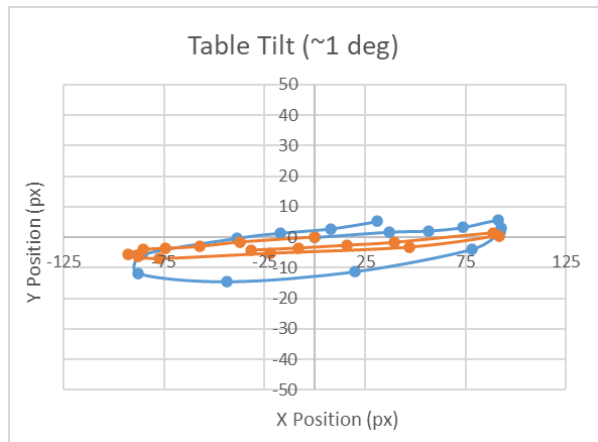


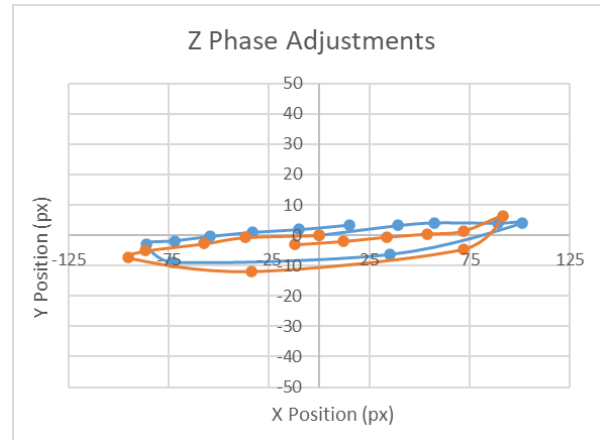
FIGURE 3.16: **Precession Figures.** The blue points are the position fit of one of the wavepackets in the  $S_-$  interferometer side (travels toward  $-X$  first) and the orange points belong to the corresponding wavepacket in the  $S_+$  interferometer (travels to  $+X$  first).

full circle trajectories, much work goes in to making sure the trap frequencies are equal (see 3.4.2) and that the Bragg beams are perpendicular to each other. The Bragg beams are made perpendicular by Bragg splitting along each horizontal direction respectively and fitting the Bragg split packets at their turning point close to the initial split. These packets form a line (similar to the method in section 3.4.3) and the angle between the lines measured. If this deviates from 90 degrees, then the Bragg yaw of one of the beams is adjusted until the lines are perpendicular. Also, if the experiment is tilted in the vertical plane (see section below) that can cause elliptical, non-overlapping trajectories.

A key parameter that can cause elliptical, non-overlapping trajectories is the Y Bragg pulse time,  $t_1$ . In Fig. 2.5,  $t_1$  is the time it takes for the packets to reach their turning point along X in Step 2 before the Y Bragg pulse is applied in Step 3. If the pulse is applied too early or late, the atoms deviate from the intended circular path, becoming elliptical and non-overlapping. In order to correctly ascertain this time, fine data points taken around the turning point must be analyzed since there is typically a large error on the period timing fit. Additionally, full trajectories of a singular wavepacket from each interferometer must be mapped out as a function of  $t_1$  (see Fig. 3.16).



(A) **XZ linear trajectories after table tilt.** Demonstrates improved tilting, however small asymmetry still persists.



(B) **XZ linear trajectories after adjusting vertical coil phases.** Demonstrates improved tilting and symmetry after adjusting the phases on the function generators that generate the vertical coil fields.

FIGURE 3.17: **Asymmetry Figures.** The blue points represent the packet location that moves in the  $-X$  direction after the initial Bragg pulse. The orange points represent the respective  $+X$  moving packet. The origin of this plot is the trap center.

### Trajectories in the Vertical Planes

The trap can experience tilting and trajectory asymmetry with respect to the  $Z$  axis. The tilting effect can be caused by a variety of issues but the simplest is that the trap geometry is tilted with respect to gravity due to the leveling of the apparatus. A worse complication is trajectory asymmetry in the vertical planes. Eddy currents are the leading explanation for trajectory asymmetry due to the imbalance of metal in the steel vacuum chamber since there is a full steel flange near the top  $Z$  coil and a window near the bottom  $Z$  coil.

Several methods were attempted to fix the asymmetry, including, tilting the table, changing the Bragg pitch, and changing the magnetic objects near or around the experiment. These methods had minimal to no effect on the trajectories. It was discovered that adjusting the phases on the function generators between the vertical coils that produce the AC quadrupole impacts and improves the asymmetry (see Fig. 3.17b).

This method ended up working well enough that once circle splitting was achieved, adjusting these Z phases as a function of cloud overlap waist became a main method for improving the trajectories and the interferometer was sensitive to these parameters. This result is surprising since there is not a clear explanation of why adjusting these phases alone improves the cloud overlap. This method is currently being tested and modeled in the context of a trap tilt electronics box and requires more research.



FIGURE 3.18: **Top Z coil function generator phase vs. overlap waist.** This plot shows the overlap of the BEC waist vertically as a function of changing the top Z function generator phase while keeping the bottom Z phase constant. This data is taken when the atoms have made one full circular period and are imaged at  $t_2$ . The blue points represent the  $S_-$  interferometer packet and the orange points represent the  $S_+$  packet. This method is used for fine tuning the wavepacket overlap leading up to checking and characterizing an interferometer.

### 3.4.5 Interferometer Characterization

Once each stage of the interferometer method (see Fig. 2.5) has been analyzed and circular trajectories are present with good overlap on every axis at different milestones in the circular trajectory, the recombine pulse is ready to be applied. The recombine pulse is applied at time,  $t_2$ . In the case of a single orbit this is the full period,  $T$ . This time can be precisely found by minimizing the waist of the overlapped clouds as a function of  $t_2$ . Typically a rough estimate is obtained from trap frequency fits first.

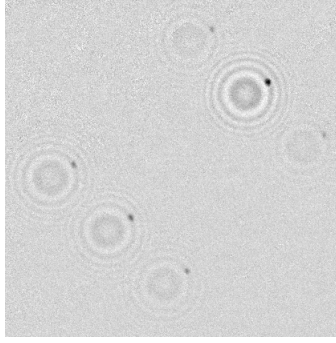


FIGURE 3.19: **Example interferometer output image.** The three absorption features in the lower left are the atoms from interferometer 1 or  $-$  with a signal of  $S_{1,-} = 0.74$  and the three features in the upper right are from interferometer 2 or  $+$  with a signal of  $S_{2,+} = 0.43$ . Each atomic wave packet produces two images, one in focus and seen as a compact spot, and the other out of focus and seen as a set of rings. These arise because the absorption probe beam passes through the atoms twice. The field of view shown is 1.56 mm across.

After a reasonable  $t_2$  is obtained, it is then possible to try interference. As a reminder, images of the packets in both interferometers are taken (see Fig. 3.19) and fitted to a Gaussian. This fit gives the signals for each interferometer by calculating and populating  $N_0/N$  for each interferometer into a spreadsheet. (Step 5 of Fig. 2.5). This signal is related to the phase by:

$$S_{\pm} = \frac{N_0(\pm)}{N(\pm)} = \frac{1}{2}(1 + \cos \phi) \quad (3.1)$$

where  $N_0$  is the number of atoms that return to the center cloud,  $N$  is the total number of atoms in the interferometer, and  $\phi$  contains the phase due to common mode noise, trap noise, and rotation phase. When  $S_+$  and  $S_-$  are plotted against each other (Step 6 of Fig. 2.5), they form an ellipse that cancels the common mode noise and after fitting gives the differential phase,  $\Delta\Phi$ .

For testing interference, several ellipse plots are made for different  $t_2$  values. The signals,  $S_{\pm}$ , the standard deviations of each signal,  $\sigma_{\pm}$ , and the visibility,  $V$ , are recorded for each ellipse plot.  $\sigma_{\pm}$  is simply the spread in  $S_{\pm}$ . The visibility of the interferometer

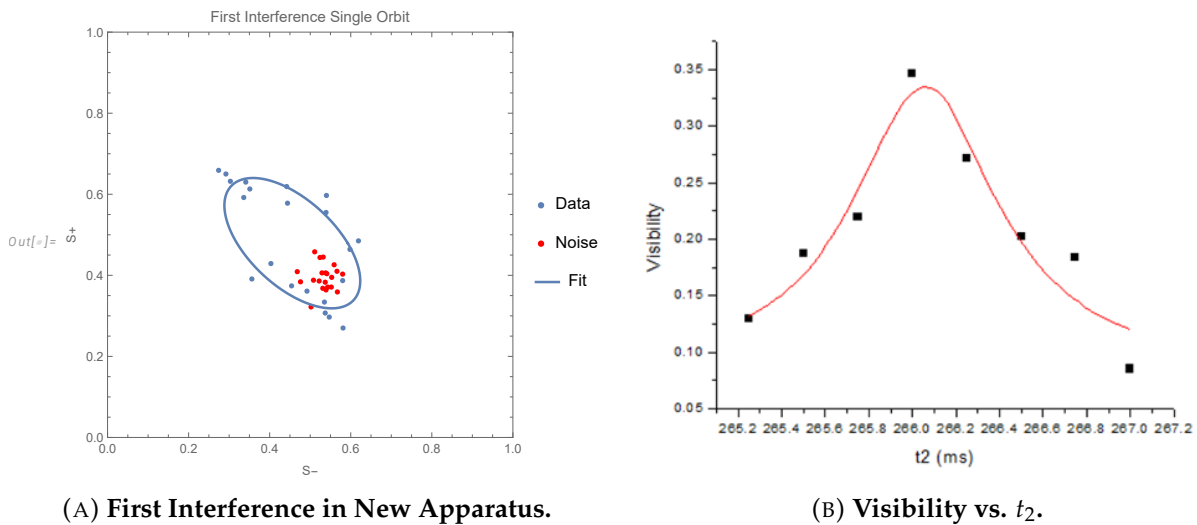


FIGURE 3.20: **Initial Single Orbit Interference Characterization.** These initial plots demonstrate a single orbit interferometer with  $V = 34\%$  and a  $\Delta\Phi = 120.1^\circ$ . In Fig. 3.20a, the red data points correspond to the wing data point in 3.20b at  $t_2 = 267$  ms which gives the noise threshold for the interferometer.

is a measure of the interferometer contrast and is a typical value for determining how prominent the interference signal is. It is related to the average of the two interferometer standard deviations by [23]:

$$V = \sqrt{8 \times \langle \sigma \rangle^2} \quad (3.2)$$

where  $\langle \sigma \rangle$  is the average of the two interferometer standard deviations,  $\sigma_{\pm}$ . After making the plots in 3.20, one can walk through parts of the parameter space to optimize the interferometer further. The parameters optimized were  $t_1$ , XY function generator phase, and the vertical coil phases. In this initial dataset, these parameter spaces were searched individually without consideration of trajectories, cloud overlap, or a change in the trap frequency. The parameters  $t_1$  and the XY function generator phase did not impact the visibility of the interferometer significantly but has been shown to impact the Sagnac phase of the interferometer.

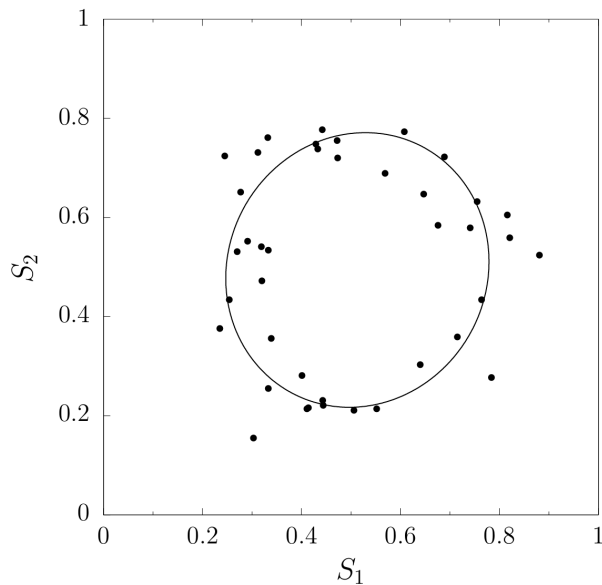
The parameters that impacted the visibility and interference the most were the Z function generator phases. Adjusting the top Z phase at the 0.25 deg step size broke the interferometer completely and adjusting the bottom Z phase by 0.25 deg saw a visibility reduction from 34% to 20%. A parameter not tested but is worth mentioning is the Bragg pitch. In [23], it was found that the Bragg pitch had an impact on the atom interferometer and changing the overlap of the atoms. In this new system with the trap frequencies being relatively close, the Bragg pitch did not significantly effect the trajectories or overlap of the atoms and so were not tested as a way to improve the interference.

To improve interference, this method was iterated over the course of several weeks with specific attention paid to trajectories, overlap, and making small improvements for both a single orbit and a double orbit interferometer. Using this parameter space and approach, a high visibility, single orbit interferometer (see Fig. 3.21a) was produced that remained stable on a daily basis and only required minimal adjustments the Bragg beam power to maintain. It is in this configuration that data from section 3.5.2 was taken.

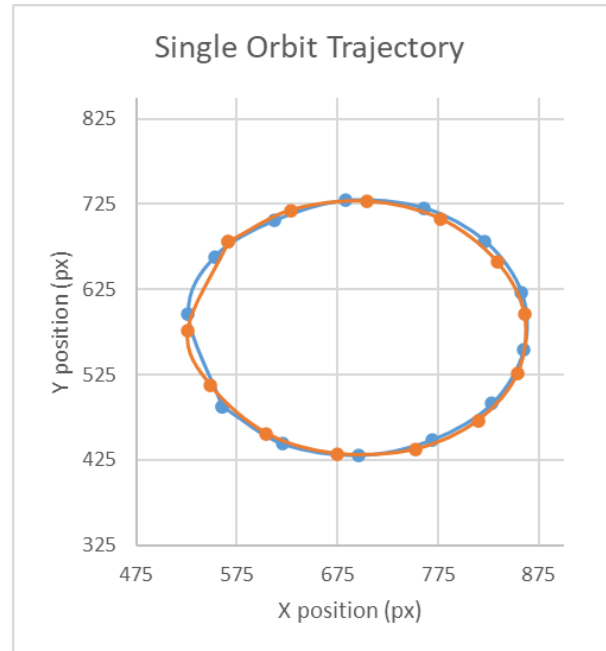
## 3.5 Results

### 3.5.1 Multiple Orbits

To enhance the sensitivity of a Sagnac interferometer, the Sagnac area must be increased. There are several approaches to increasing the Sagnac area. For instance, the orbit radius,  $R$ , can be increased by making the trap weaker, so that the atoms have a larger oscillation amplitude for a given kick momentum. Alternatively, the kick momentum itself can be increased using a higher order Bragg process. Finally, the effective



(A) **High visibility single orbit interferometer ellipse.** Data points are signal  $(S_1, S_2)$  pairs obtained in  $N = 40$  sequential runs of the experiment. The curve is a fitted ellipse yielding a differential phase of  $\Delta\Phi = 1.5$  rad and a visibility of  $V = 0.54$ .



(B) **Single orbit trajectory.** The blue and orange data points are the fitted positions of a single cloud from interferometer 1 and 2 respectively in the horizontal plane. The trajectories were fitted to an ellipse with interferometer 1 axes  $a = 168.2$  px and  $b = 156.1$  px and interferometer 2 axes  $a = 168.8$  px and  $b = 148.8$  px. These trajectories are nearly circular and have a radius,  $R = 0.57$  mm.

FIGURE 3.21: **High Visibility Single Orbit Interferometer with Trajectory**

area can be increased by allow the atoms to make multiple orbits in a given trap. The reported single orbit interferometer in this dissertation is already a large improvement on the previous apparatus because we were able to weaken the trap from  $\omega_{xy} = 10$  Hz to  $\omega_{xy} = 3.5$  Hz allowing the atoms to travel further away from the trap center with a Bragg kick of  $2\hbar k$ . This decrease in trap frequency increased the effective Sagnac area from  $0.5 \text{ mm}^2$  to  $4.1 \text{ mm}^2$  for a single orbit. An additional increase in the Sagnac area was achieved by allowing the atoms to travel around multiple times (see Figs. 3.22 and 3.23a). Using a higher order momentum kick (such as  $4\hbar k$ ) for interferometry has not been explicitly tested in this system yet and could be a future direction, particularly if atom-atom interactions become problematic in multiple orbits. The double orbit interference is a  $16\times$  improvement in the area of the previous apparatus Sagnac area which leads to an order of magnitude in the calculated sensitivity. While a triple orbit interferometer was attempted, the data in Fig. 3.23 is indistinguishable from detection noise.

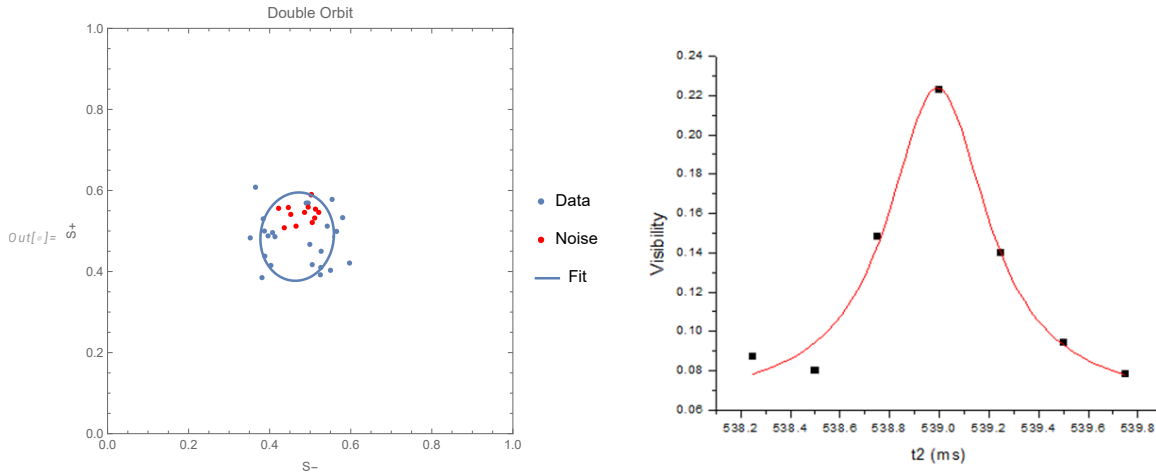
### 3.5.2 Phase Stability and Characterization

To characterize the short-term and long-term stability of this system in the context of an inertial sensor, it is worth reviewing the errors that matter and how those relate to the measured differential Sagnac phase. A reminder that  $\Delta\Phi$  is measured by fitting the interferometer signals to an ellipse:

$$\Delta\Phi = \frac{2m}{\hbar}\Omega \cdot A_{eff} \quad (3.3)$$

The phase noise that can be measured,  $\delta\phi$ , is related to the noise on the rotation measurement,  $\delta\Omega$ , by:

$$\delta\phi = \frac{2m}{\hbar}\delta\Omega A_{eff} \quad (3.4)$$



(A) **Double Orbit Interferometer.** The solid blue points are the signal data points, the red points demonstrate the detection noise, and the blue line is the ellipse fit measuring  $\Delta\Phi = 1.3$  rad with a  $V = 0.22$ .

(B) **Double Orbit Interferometer Visibility.** The black points are different visibilities for different double orbit interferometers as a function of recombine time,  $t_2$ . The red line is a Lorentzian fit and is centered on  $t_2 = 539$  ms.

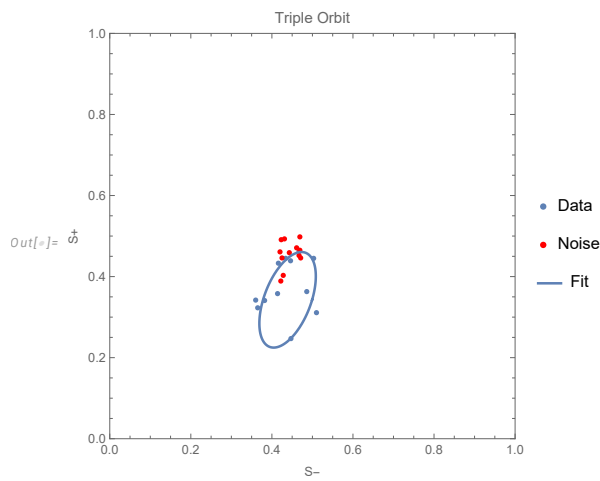
FIGURE 3.22: **Double Orbit Interferometer Characterization.** When considering the double orbit ellipse fit, spread of the data, and the visibility plot, this is sufficient evidence that a double orbit atom interferometer has been observed [47].

Rearranging the equation gives:

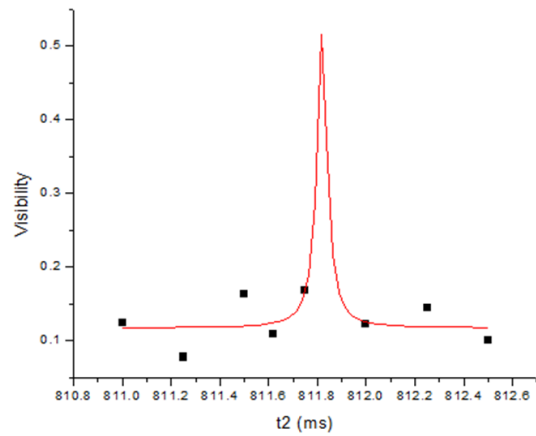
$$\delta\Omega = \frac{\hbar\delta\phi}{2mA_{eff}} = \delta\phi \times 10^{-4} \quad (3.5)$$

with the constants for a single orbit interferometer,  $\frac{\hbar}{2mA_{eff}} \approx 10^{-4} \text{ s}^{-1}$ .

If  $\delta\phi$  is a long-term phase noise measurement (one example is when the Allan deviation slope becomes zero, see section 1.5), then the calculated  $\delta\Omega$  is the bias stability of the system. The units here, rad/s can be converted to deg/hr for easy comparison to traditional values given in Fig. 1.4. A reminder that this is a critical value for characterizing a gyroscope for inertial navigation applications because that term has cubic growth as a function of integration time,  $T$  (see Eq. 1.18) when calculating a user's position.  $T$  and  $\tau$  will be used interchangeably for the rest of this dissertation to mean the integration time.



(A) **Triple Orbit Interferometer.** The solid blue points are the signal data points, the red points demonstrate the detection noise, and the blue line is the ellipse fit measuring  $\Delta\Phi = 1.1$  rad with a  $V = 0.16$ .



(B) **Triple Orbit Visibility.** The black points are different visibilities for different triple orbit interferometers as a function of recombine time,  $t_2$ . The red line is a Lorentzian fit and is centered narrowly on  $t_2 = 811.8$  ms. This plot is nonsensical but is here to demonstrate that both a good visibility plot and ellipse are needed to verify interference.

FIGURE 3.23: **Triple Orbit Characterization.** While from 3.23a, it appears that interference has been observed given the fit, shape, and spread compared to the noise datum. In Fig. 3.23b, it is clear that this is not distinguishable from other noise points.

From this relationship, one can also see how the short-term phase noise impacts the rotation measurement noise. Another reminder that the Angle Random Walk (ARW) is the other important value for a gyroscope as it gives a measure of the sensitivity of the gyroscope with a specified integration time and, as a noise term, is the second highest growth in position error. The ARW can also be evaluated by the Allan deviation. The relationship between the rotation measurement noise and ARW is given by:

$$\delta\Omega = \frac{\hbar\delta\phi}{2mA_{eff}} = \frac{ARW}{\sqrt{T}} \quad (3.6)$$

This relationship leads to:

$$ARW = \sqrt{T} \frac{\hbar\delta\phi}{2mA_{eff}} \quad (3.7)$$

This apparatus demonstrated much stability compared to the previous apparatus and could run continuously for more than one day. A critical measurement for any gyroscope is the Allan deviation (see section 1.5) because it provides one with the short term and long term stability of noise processes in the system. The Allan deviation was taken for the atom interferometer presented above by running the experiment on a continuous cycle for over 26 hours. Figure 3.24a shows the results of all 931 experimental runs. To characterize the impact of the noise on the phase determination, the Allan deviation, defined as the square root of the Allan variation is used. From Chapter 1, the formula used for the Allan variation of a single sensor is:

$$\sigma_{\tau}(M)^2 = \frac{M}{M-1} \left[ \frac{1}{M} \sum_{i=1}^M \Omega_{\tau i}^2 - \left( \frac{1}{M} \sum_{i=1}^M \Omega_{\tau i} \right)^2 \right] \quad (3.8)$$

with

$$\Omega_{\tau i} = \frac{\Delta t}{\tau} \sum_{j=1}^{\tau/\Delta t} \Omega(t_i + j\Delta t) \quad (3.9)$$

In the experiment performed,  $\Delta t = 80$  s because that is the length of time to take a

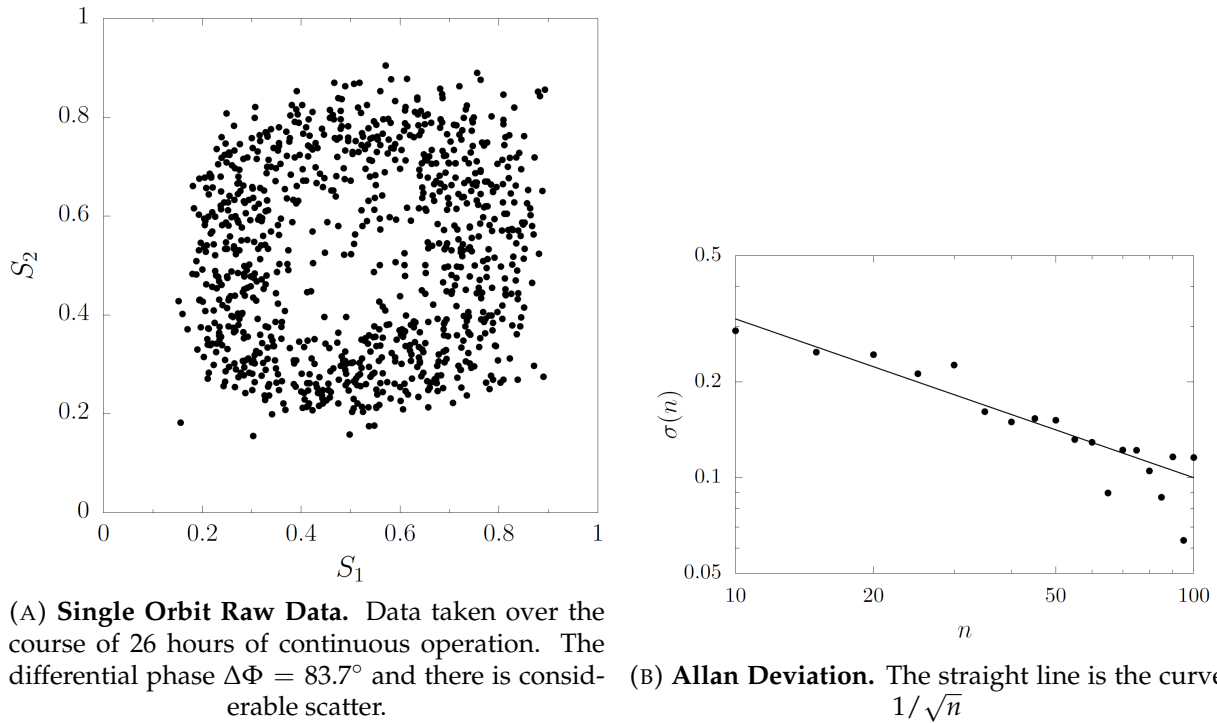


FIGURE 3.24: Allan Deviation Dataset

single interferometer measurement.  $\tau = n\Delta t$ , where  $n$  is the number of points used for each phase measurement (i.e. number of points in an ellipse and is  $n \geq 10$  points.  $\tau$  is therefore the averaging time for different numbers of points used in the phase measurements,  $\Omega_{\tau i}$ . Finally,  $M$  is the number of phases each averaging time used. To take a concrete example, in Fig. 3.24b, the first data point is positioned on  $n = 10$ . This means that 10 data points were used in each phase measurement, with a total number of phases,  $M = 93$ . This corresponds to an averaging time,  $\tau = 800$  s. Given this information and all of the phase measurements, one can calculate the Allan deviation from Eq. 3.8 by taking the square root. This can then be plotted for different values of  $n$  and consequently  $\tau$ .

Two characteristics stand out in the the Allan deviation plot. First,  $\sigma(n)$  averages down as  $1/\sqrt{n}$  all the way to  $n = 100$ , or  $\tau = 8000$  s. This indicates that the apparatus exhibits no drifts on this time scale, which can be compared to typical drift times of

1 to 100 s for conventional rotation sensors such as ring laser gyroscopes, fiber optic gyros, or MEMS gyros. On the other hand, the overall scale of the noise is quite high. This can be seen by extrapolating back to  $n = 1$ , which yields a total phase noise,  $\delta\phi$ , of 1 rad per run. The  $1/\sqrt{n}$  scaling in the Allan deviation indicates that this noise is uncorrelated between runs. Using Eq. 3.7 and  $T = 80$  s for a single run, this gives an  $ARW = 3.1 \text{ deg}/\sqrt{hr}$  and, using Eq. 3.6,  $\delta\Omega = 10 \text{ }\mu\text{rad/s}$ .

Another characterization of the short-term noise can be seen using the single orbit interferometer in Fig. 3.21a. This dataset has  $n = 40$  sequential points and was fit to an ellipse. The ellipse fit gave a  $\delta\phi = 0.1$  rad. With 40 points, each 80 s long, the total integration time is  $T = 3200$  s. Using these numbers and the same equations above, we see an  $ARW = 2 \text{ deg}/\sqrt{hr}$  and  $\delta\Omega = 10 \text{ }\mu\text{rad/s}$  which is reasonably consistent with the Allan deviation measurement.

While this Allan deviation does not allow for a full characterization of the bias stability since it does not present a flat slope region, it allows one to place an upper limit on it and can be characterized and cross-checked by two methods. One method consists of looking at the total change in the phase over the course of continuously running for 26 hours (i.e. comparing the first dataset and the last dataset in the Allan deviation measurement). This method yielded a  $\delta\phi = 0.2$  rad and using Eq. 3.5, this leads to a run-to-run bias stability,  $b = 4 \text{ deg/hr}$ . The second method involves a test where the interferometer is observed and then the experiment shut down and restarted 24 hours later and an interference measurement taken and compared. In this second test, the lasers, trap currents, and Rb source were turned off, while vacuum pumps and other control equipment were left on. After restarting, the apparatus was allowed to warm up for 1 hr before interferometer measurements were taken. This second method gave a similar value for  $\delta\phi$  so these methods are consistent. Of special note, since the Allan deviation region is still dominated by the ARW where the data points were taken,

so the bias stability is actually better than 4 deg/hr because the plot is still averaging down.

### 3.5.3 Trap Frequency and Cross Term Noise Analysis

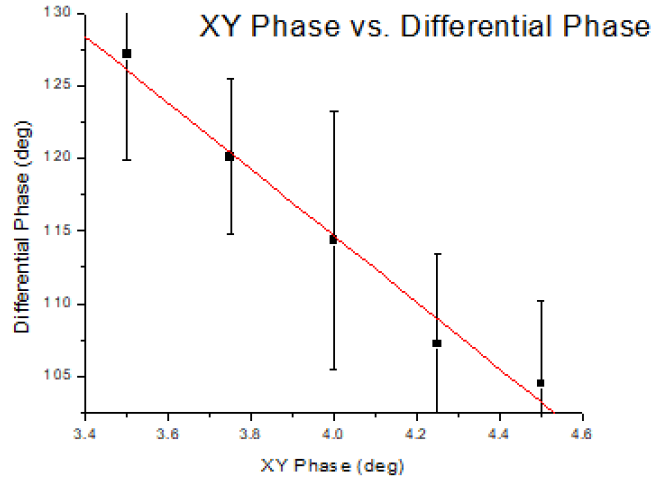


FIGURE 3.25: **XY Phase vs. Differential Phase.** This dataset was taken with the data in Fig. 3.20. Error bars correspond to the phase error from the ellipse fit for each interference point with minimal changes to the visibility throughout the measurement. The red line is a linear fit giving a slope = -22.

One candidate for the large short-term phase noise is fluctuations in the trap frequency,  $\delta\omega$ , induced by the trapping fields. These fields are subject to drifts and  $\delta\omega$  coupled with a non-zero cross term,  $\gamma_{xy}$  in Eq. 2.4, leads to phase fluctuations [45]:

$$\delta\phi = 2\pi^2 k R \gamma (n + 2n^2) \frac{\delta\omega}{\omega} \quad (3.10)$$

where  $R$  is the radius of the trajectory,  $n$  is the number of orbits,  $k$  is the wave number, and  $\omega$  is the trap frequency.

The experiment can be used to estimate the level of control over the trap frequency on a short-term scale. In Fig. 3.25, this demonstrates the relationship between

the phase noise and the XY function generator phase,  $\delta\phi/\beta$ , where  $\beta$  is the function generator phase and is related to  $\gamma$  by  $\gamma = \frac{2\beta}{7}$  [37]. Rearranging the formula above for  $n = 1$  and  $k = \frac{2\pi}{\lambda}$ , where  $\lambda$  is the wavelength of the laser:

$$\frac{\delta\phi}{\beta} = \frac{24\pi^3 R}{7\lambda} \frac{\delta\omega}{\omega} \quad (3.11)$$

Plugging in the slope measured in Fig. 3.25 and solving for  $\frac{\delta\omega}{\omega}$  yields a fluctuation noise ratio  $\approx 10^{-4}$ . This result combined with the ability to control  $\gamma$  at the  $10^{-2}$  level leads to a phase fluctuation of  $\delta\phi = 0.27$  rad which is consistent with the noise that was observed in the Allan deviation dataset and the 24 hr turn off test.

In this chapter, the building and characterization of a lab-scale apparatus that demonstrates long term-stability, even while it is hindered by short-term noise due to trap fluctuations, has been discussed. The main motivation for pursuing a trapped-atom interferometer is the potential for a compact apparatus, as size requirements are in practice critical for inertial navigation applications. The current apparatus is 2 m long but Bose condensation can be achieved in much smaller systems using atom-chip or laser-trap technologies. The next chapter will discuss a prototype compact apparatus that has the technological capabilities to meet the above requirements to improve the sensitivity and bias stability of the lab-scale apparatus. The final chapter of the dissertation will discuss these stability results in the context of modern gyroscopes and technical improvements that must be implemented to achieve strategic grade accuracy.

## Chapter 4

# Compact System

### 4.1 Experimental Apparatus

#### 4.1.1 Overview

In the previous chapter, a dual Sagnac atom interferometer was presented using a BEC in a TOP trap with an effective Sagnac area of around  $8 \text{ mm}^2$  and with a rotation sensitivity of order  $10 \mu\text{rad/s}$ . However, this demonstration apparatus is too large and complex to be a viable solution for field applications, such as inertial navigation, and is poorly suited even for laboratory-based environmental testing. In addition, the system operates at a relatively low duty cycle, which limits the achievable sensitivity at short integration times.

A new compact apparatus that aims to address these shortcomings is described in this chapter. The apparatus was developed as part of the Atomic-Photonic Integration (A-PhI) program at DARPA. Under this program, UVA subcontracted Northrop Grumman Missile Systems (NGMS), ColdQuanta, Inc. (CQ) <sup>1</sup>, Air Force Research Laboratory (AFRL), and Space Dynamics Laboratory (SDL). CQ developed the compact

---

<sup>1</sup>now doing business as Infleqtion c. 2022

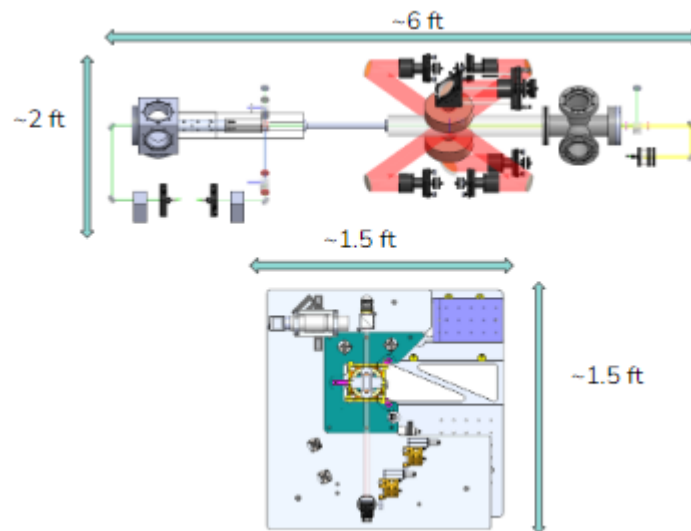


FIGURE 4.1: **3D CAD Models of Lab Apparatus vs. Compact Apparatus.**  
A size comparison between the proof of concept experiment and the CQ apparatus

system and relevant vacuum technology; NGMS developed the trap coil system and drive electronics; AFRL produced microfabricated atom chips; and SDL provided theory and numerical modeling support.

This apparatus is designed to produce the same magnetic fields and to provide the same optical access as the operational lab-scale system, but miniaturized to a total volume of about 50L, not including laser sources and electronics. All of the free space optics are mounted on the assembly, with light entering through optical fiber ports. The platform is moderately portable to support environmental testing, and is designed to use an atom chip, which can speed up the production rate for BEC and provides finer control over the TOP trap potential. The magnet coils and atom chip are all in air. This configuration facilitates modifications to the magnetic elements in order to fix problems and test new designs.

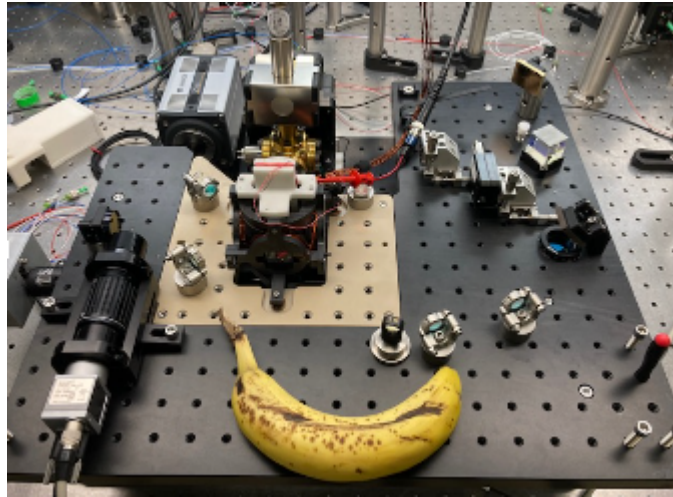


FIGURE 4.2: **Top View Picture of Compact System.** A top view of the compact system with a banana for scale (chip tower not pictured; surrogate MOT wire tower in its place)

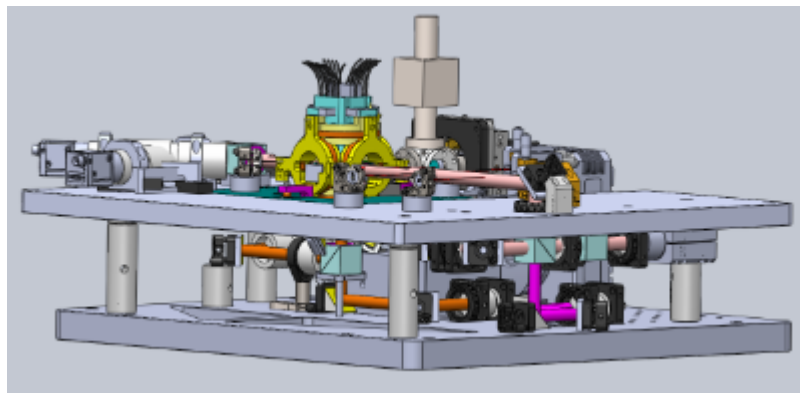


FIGURE 4.3: **CAD drawing of the compact system showing the atom chip tower and coil assembly.**

### 4.1.2 Vacuum System

A key element for the compact apparatus is the miniaturization of the vacuum system. In the lab-scale instrument described previously, the vacuum system has two main chambers: the MOT chamber and the science chamber. The MOT chamber contains a Rb getter source and laser beams to collect about  $10^9$  atoms in a magneto-optical trap (MOT). These atoms are loaded into a quadrupole magnetic trap produced by a high-current coil pair, and the coil pair is then mechanically translated to carry the atoms

through a thin differential pumping tube into the science chamber. The science chamber contains trapping coils and provides optical access to produce a BEC and implement the Sagnac interferometer. The entire chamber is about 2.5 m long and about 0.5 m wide and high, at maximum extents (see Fig. B.3).

The new compact system is a customized version of the CQ RuBECi product [48]. It also consists of two chambers (see Fig. 4.4) where the first now contains Rb dispensers and a two-dimensional (2D) MOT. This MOT generates a slow atomic beam which is directed through a pinhole aperture into a science chamber. In this case, both chambers are small glass cells, about 10 cm long and 2 cm square. The entire assembly is about 40 cm long and 20 cm wide and high at maximum extents. The 2D MOT cell is part of the CQ Fixed Photonically Integrated Cold Atom Source (PICAS) system [49]. This system consists of three optical fiber inputs and two permanent magnets that produce the 2D MOT and launch the cold atom beam through the pinhole see Fig. 4.5).

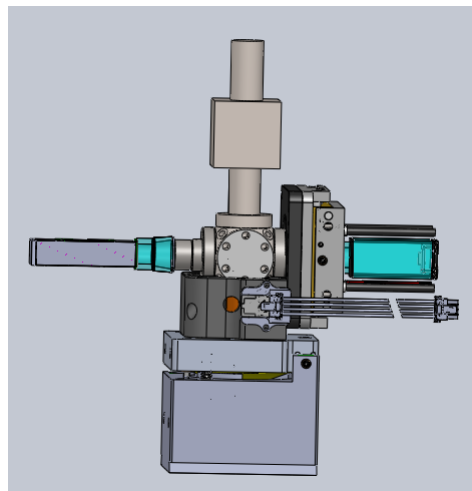


FIGURE 4.4: A CAD drawing of the vacuum system and mounting stage. The cell on the left is the science cell; the cell on the right is the 2D MOT cell. The miniature ion pump is on top of the steel vacuum part connecting the chambers.

In the science chamber, a 3D mirror MOT collects atoms from the PICAS beam, which can then be loaded into a magnetic trap. The upper cell wall is a 1-mm thick

silicon membrane. The vacuum side of the membrane is reflection coated and it serves as the mirror for the mirror MOT. The atom chip is positioned adjacent to (above) the air side of the membrane. The science cell is also surrounded by a set of six bias coils that produce fields needed for both the surface MOT and the magnetic trap.



FIGURE 4.5: **PICAS system.** The push beam couples in to the central fiber jack in the rear, the 2D MOT beams couple in to the other two fiber inputs (one pictured). This system contains permanent magnets within and optics used to produce the 2D MOT beam. When mounted, it fully encloses the 2D MOT cell.

Similar technology has been previously deployed by CQ in both off-the-shelf and custom products. However, their standard products yield a vacuum-limited cold atom lifetime of 5 to 10 s, while our interferometer would require a lifetime of 10 to 20 s. To accommodate this requirement, CQ implemented two novel techniques. First, all interior steel surfaces were coated with a passivating material to reduce hydrogen outgassing. Second, a cleaner rubidium source was installed, consisting of a chemically inactive material which could absorb large quantities of alkali metal. The sorber is loaded by running a conventional rubidium dispenser, which produces significant quantities of hydrogen and other contaminants. The conventional dispenser is then shut off and

for science operation the sorber is heated, which releases the rubidium with few contaminants. Using these methods, CQ observed a factor-of-two increase in the lifetime of atoms in an optical trap, although this is unconfirmed in the delivered compact system.



FIGURE 4.6: A photograph of the 3D MOT vacuum cell. The cell by itself with the Bragg mirrors attached and silicon membrane featured prominently.

### 4.1.3 Optics

The light required for the experiment is produced by two 780 nm diode lasers. One of the lasers provides the Bragg laser beams required for atom interferometry, and is tuned typically to 10 GHz off of the  $5S_{1/2}$  to  $5P_{3/2}$  atomic resonance. The other laser is locked near resonance and generates the 2D MOT beams, the 3D MOT beams, the push beam, optical pumping beams, and absorption probe beams. Light is delivered to the optics platform via single-mode optical fibers, and then directed to the atoms via free space optics. The beam path layout is analogous to that used in the lab-scale apparatus with the addition of the push beam.

Figure 4.7 features a laser diagram for the compact system. The MOT light is produced by a Toptica DL Pro laser. A portion of the output is double-passed through an acousto-optic modulator (AOM), and then delivered to a saturated absorption lock.

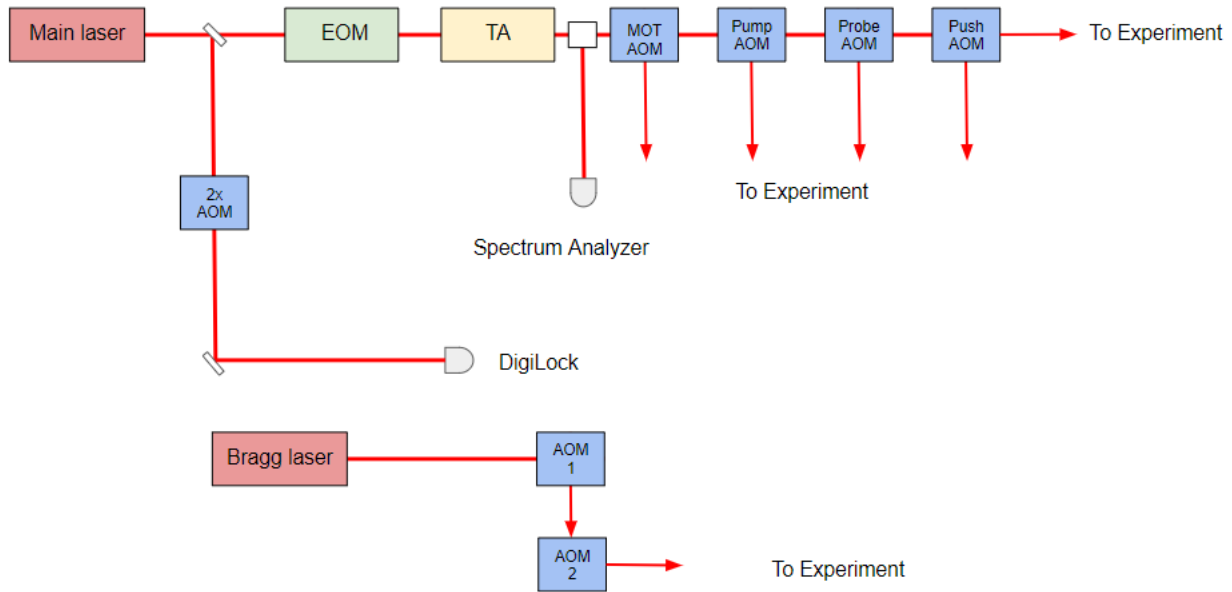


FIGURE 4.7: **Block diagram of laser pathways for the compact system.**

The frequency of the laser can thus be fine-tuned by adjusting the frequency of this lock AOM. The remainder of the output light is coupled to a fiber electro-optic phase modulator (EOM), where modulation at 6.6 GHz produces a sideband used for optical pumping the  $F = 1$  atomic ground state. The EOM output is amplified by a Toptica BoostTA (TA) tapered amplifier, to a total power of approximately 1.5 W. The light then passes through a series of AOMs and beam splitters that distribute light to the various parts of the experiment. The Bragg beams are produced by a Vescent DFB laser which can be phase locked to the MOT laser. A pair of AOMs are used to modulate the beam before it is delivered to the atoms in an effort to reduce leakage light that can cause problems with Bragg splitting fidelity. Bragg splitting has not been tested in the CQ system yet.

The optics platform itself consists of a stack of two 50 cm breadboards with optics mounted on three layers. The vacuum chamber and coils are mounted to the bottom breadboard and enclosed by a cutout in the upper breadboard. The breadboards

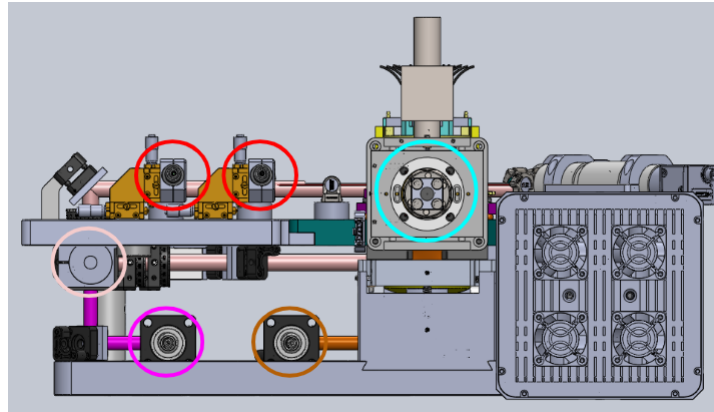


FIGURE 4.8: **CAD drawing showing fiber inputs for the entire system.** Red circles show the Bragg beam and side imaging probe beam inputs. The light pink circle shows the 3D MOT input. The light blue circle shows the PICAS area where the 2D MOT and push beam inputs are. The hot pink circle shows the pumping beam input. The orange circle shows the bottom imaging probe beam input.

are aluminum, but the inner section of the upper breadboard is replaced by a non-conducting plastic material to minimize eddy currents from the oscillating TOP fields. The platform provides absorption imaging capabilities in the horizontal directions, using the same beam paths as for the Bragg beams. The horizontal imaging axes need to accurately align the Bragg beams and to ensure that the atomic wave packet trajectories close properly. A vertical imaging direction is also available, in which a probe beam is launched vertically upward into the vacuum cell, reflects at normal incidence from the silicon membrane mirror, and then exits the cell and is directed by a polarizing beam splitter onto the imaging camera. This imaging system is used to monitor the atom interferometer output.

An aspect of the compact system which differs from the lab-scale system is the use of a 3D mirror MOT. The optical layout for this MOT is complicated by the constraints of the coil structure needed for the TOP trap. One of the MOT beams is relatively simple, with a horizontal beam passing parallel to the silicon mirror surface and then retro-reflected from a free-space mirror. The other beams are incident on the silicon

mirror at 45 deg angles (see Fig. 4.13). The delivery optics for these beams consist of two gold fold mirrors and two thin sapphire mirrors which are mounted to the magnetic coil assembly as illustrated. In the initial design, all four of these mirrors were fixed in place, with no alignment adjustment possible.

The coil structure also impedes optical access for the two required Bragg beams. To overcome this, four mirrors are epoxied to the sides of the glass cell (see Fig. 4.12). The same beam paths are used for the horizontal imaging. Although this does provide the required access, the mirrors are small and nonadjustable, which places constraints on both the Bragg and imaging alignments.

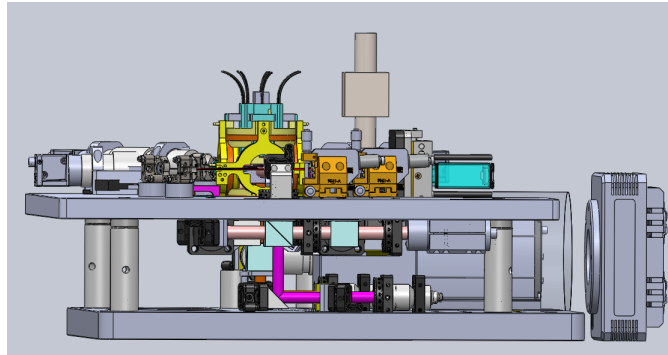


FIGURE 4.9: **CAD drawing of the compact system, side view.** The 3D MOT beam is represented as light pink, and the optical pumping beam as hot pink.

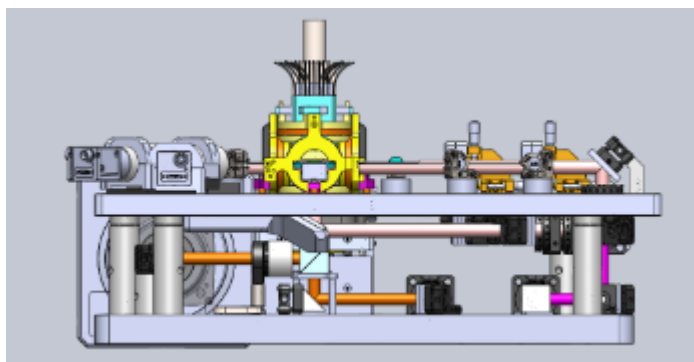


FIGURE 4.10: **CAD drawing of the compact system, front view.** The vertical imaging probe beam is represented as orange.

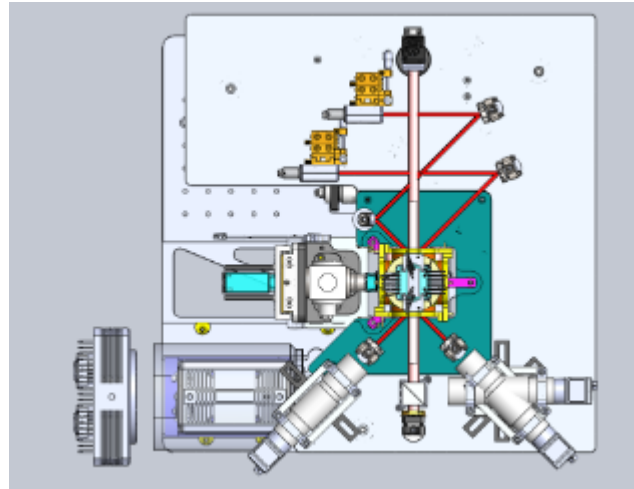


FIGURE 4.11: **CAD drawing of the compact system, top view.** Bragg beams and side imaging probe beams represented as red. This figure also demonstrates the possible horizontal imaging camera locations.

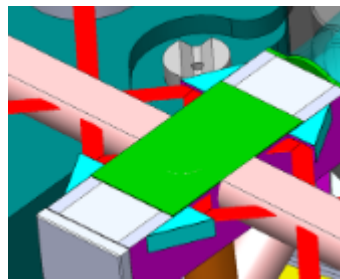


FIGURE 4.12: **CAD detail of cell and Bragg beam layout.** The blue prisms are mirrors epoxied to the external cell wall.

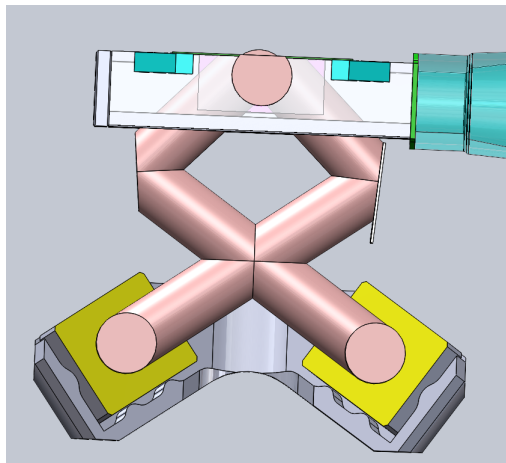


FIGURE 4.13: **CAD detail of mirror MOT optics and beams.**

#### 4.1.4 Atom Chips and Coils

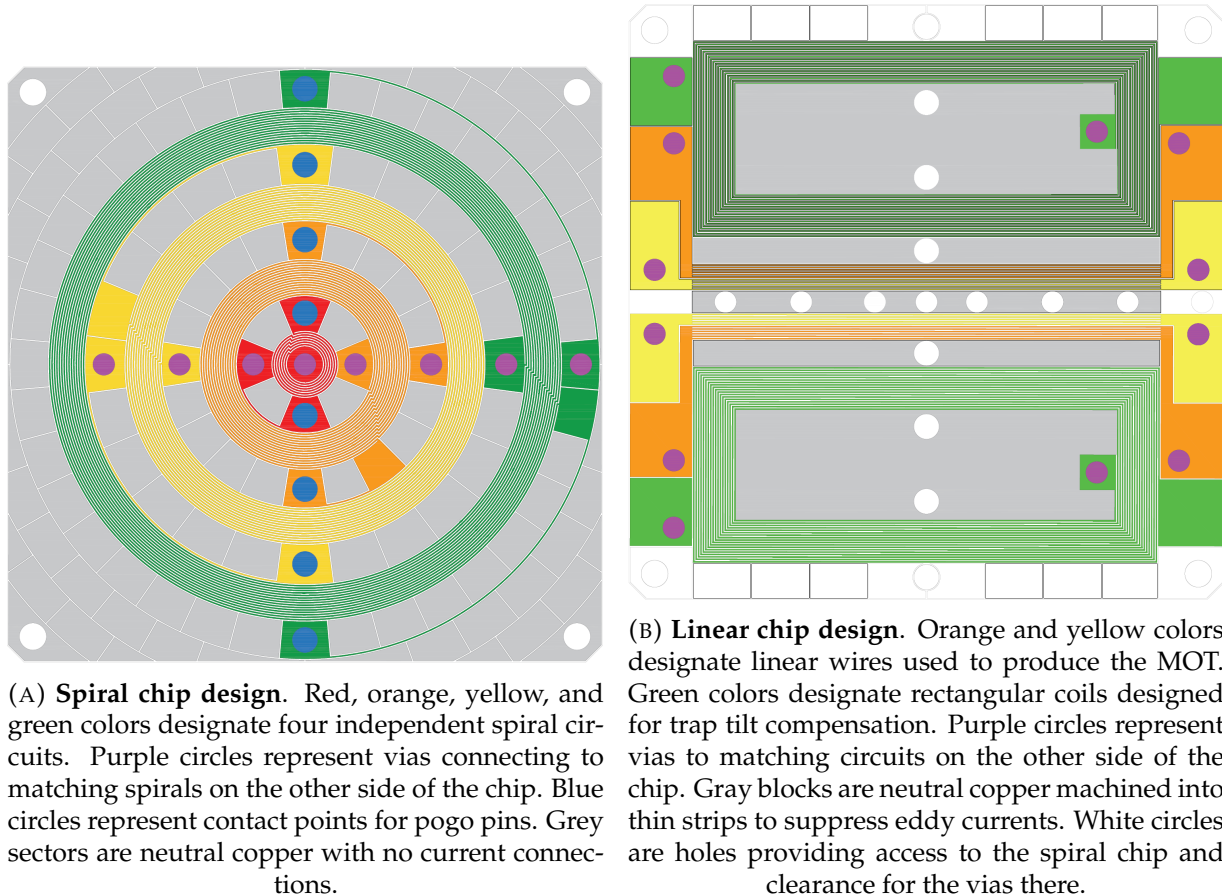


FIGURE 4.14: **Atom chips**

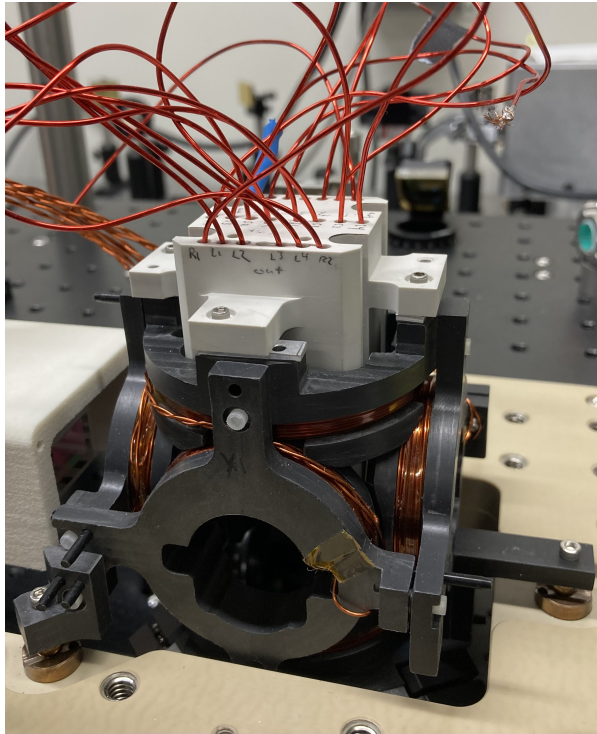
Although atom chips are by now a well-developed technique, the present effort is the first attempt to produce a TOP trap using an atom chip, and as such it has several novel requirements. The compact apparatus uses a stack of two double-sided chips: the chip closest to the atoms features spiral coils that are used to produce the magnetic trap for evaporative cooling and atom interferometry, while the more distant chip features linear wires that are used to produce the mirror MOT and to compensate for tilts of the apparatus with respect to gravity. The two chips are separated by thin Kapton film, and then mounted onto a heat sink block machined from Shapal ceramic. Shapal is an

electrical insulator with good thermal conductivity (as discussed previously in Chapter 3), so that the chip heat can be managed while avoiding eddy currents. Electrical contact to the chips is made via solderless pogo-pin spring connections. The pogo pins are mounted in the heat sink block, and access to the spiral chip is provided by holes in the linear chip. Lead wires to the pogo pins are delivered through holes in the top surface of the block.

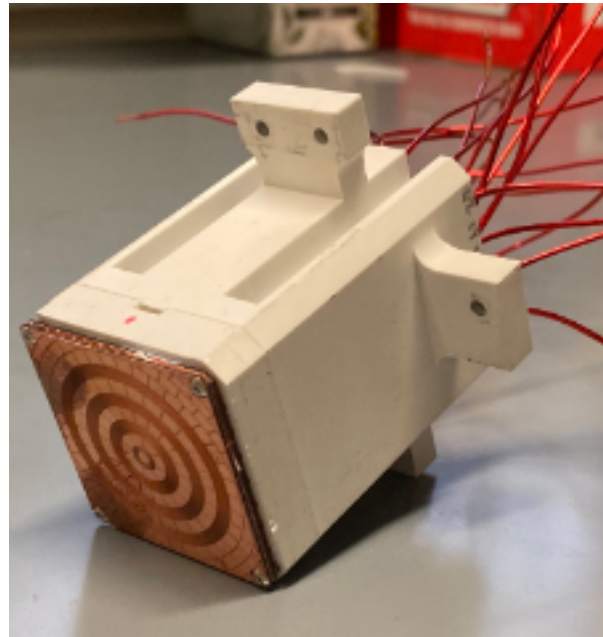
Both atom chips were fabricated at AFRL, by laser machining of direct-bonded copper on aluminium nitride [50]. The chip features 72- $\mu\text{m}$  wide traces laser-cut into 0.12 mm thick copper layers and the aluminum nitride substrate is 0.76 mm thick. Each chip is 35 mm square. Both chips have areas containing conducting wires for producing trap fields, and other areas with no current carrying elements. To suppress eddy current effects, the passive areas are machined into small non-contiguous elements; on the spiral chip these are trapezoidal regions about 3 mm across, while the linear chip uses wire-like patterns.

The spiral chip (see Fig. 4.14a) features four coils with average radii ranging from 1.5 mm to 14 mm. The smallest coil can produce a magnetic gradient of 600 G/cm at the atom location with a power dissipation of 7 W. A version of the spiral chip that lacked the eddy current remediation was initially incorporated into the lab-scale vacuum chamber for testing, but we found that the eddy currents were sufficiently asymmetric to prevent the interferometer from working and the chip was removed.

The TOP trap bias fields are produced by six orthogonal coils mounted on a Delrin frame. The frame itself is mounted to the upper optical breadboard. The configuration allows the vacuum chamber to slide in and out of the assembly so that either the chamber or coils can be accessed independently when needed. The mounting points for the coil structure and chip heat sink block are designed such that the position of the current elements does not change, to first order, under the modeled heat load of the trap.



(A) Photograph of the full coil assembly with chip tower. The vacuum cell is not in place.



(B) Photograph of assembled chip tower showing spiral chip.

FIGURE 4.15: Chip tower and coil photos

## 4.2 Results and Challenges

The initial goal for the compact apparatus was to produce a BEC in the spiral chip trap. Based on comparisons to other atom-chip systems, expected BEC cooling times of 5 s or less should have been possible. Unfortunately, this goal was not achieved during the A-Phi project. Although a MOT was implemented, the number of atoms trapped was inconsistent, and the best numbers achieved, of order  $10^7$  atoms, was a factor of ten lower than what is the estimated requirement to produce a BEC.

Discussed here are the challenges encountered, with the fundamental issue being the difficulty of modifying the compact system to diagnose and correct problems encountered. In retrospect, it would have been better to implement an intermediate system using the compact cell and chip with a lab-scale optics platform that permitted

easier modification and testing (such a hybrid system is discussed in Chapter 5).

### 4.2.1 Chip heating

One source of MOT inconsistencies was heating of the chip. The MOT magnetic field configuration requires a DC linear gradient field of about 10 G/cm, which can be generated by wires on the linear chip. The chip has a total of four independent linear traces that were wired in series with a total resistance of 1.6 Ohms. A current of 6.0 A was required to achieve the MOT gradient. During steady operation, the heat load of 10 W caused significant temperature increase in the heat sink block. The chip temperature itself was measured by monitoring the resistance of one of the spiral chip coils and assuming the normal copper temperature coefficient of 0.4%/K. Over the course of 30 minutes, the chip temperature increased by about 50 K (see Fig. 4.16), and as this occurred, the MOT was observed to diminish or disappear altogether. To mitigate this problem, a small electric fan was installed on the apparatus to improve air cooling of the block. This reduced the temperature increase to about 15 K, and eliminated obvious effects on the MOT performance. However, forced air cooling typically degrades the stability of nearby laser beam paths, making this undesirable as a permanent solution.

### 4.2.2 Beam polarization

Another source of instability was polarization drift of the 3D MOT beams. This occurs because it is difficult to precisely couple input light to the correct mode of a polarization-maintaining fiber, and then temperature changes can cause the polarization of the fiber output to vary. Although small, these variations had a significant effect

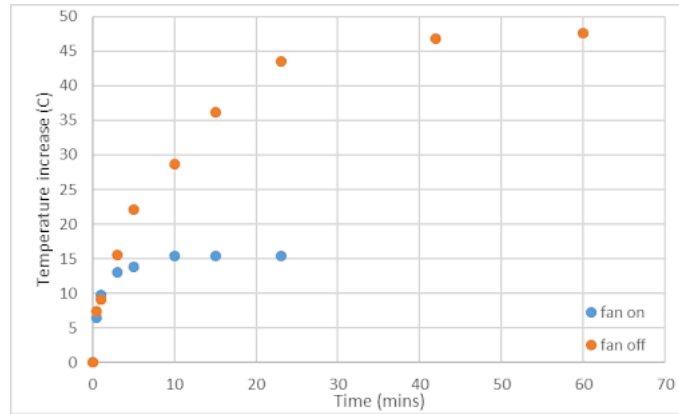


FIGURE 4.16: **Chip heating measurements.** The data shows an increase in temperature from room temperature over the course of several minutes. The orange data points were taken without the external electric fan on and the blue data points were taken with the blue fan on.

on the MOT beam balance, since the beams are generated using polarizing beam splitters. To mitigate this, a polarizer was installed to fix the beam polarization before reaching the beam splitters. The variations in beam power caused by transmission through the polarizer were small enough to neglect. Although this is a straightforward solution to a common problem, it required considerable modification of the optics platform to install the polarizer, since initially there was insufficient space for it. Owing to this, it was not possible to mount the polarizer in its own independently rotating stage. In order to set the orientation of the polarizer it was necessary to repeatedly remove the optic, adjust the mount, and then replace it. Further, the half-wave plate used to set the beam balance required a mount that was too large to bolt directly to the optics breadboard, so the board featured an indentation to accommodate it (see Fig. 4.17). It was necessary to design a mount for the polarizer that worked with the same indentation. Ultimately, the problem was satisfactorily resolved, but what would have been an hour of work in the lab-scale system required roughly a week of effort.

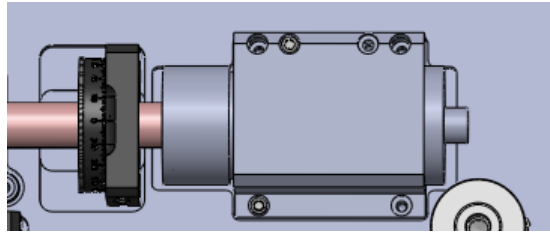


FIGURE 4.17: CAD drawing of the fiber launch and half-waveplate mount. It was necessary to insert a polarizer between these two elements.

### 4.2.3 Beam alignment

In the course of fixing the polarization problem, it became evident that the MOT performance was unusually sensitive to the MOT beam alignment. Adjusting this alignment carefully presented several challenges. First, many of the relevant optics were mounted on the bottom side of the upper breadboard, making them difficult to adjust. Second, the final set of mirrors for the vertical beams was complicated by the coil assembly (see Fig. 4.13). There was no simple way to visualize or evaluate the resulting beam alignment at the location of the atoms. Because of these problems, any time an optics layout change was required, it took an inordinate amount of time to realign the beams to recover the MOT.

The method developed to overcome these alignment challenges consists of removing the top breadboard and flipping it over for better access to all of the relevant optics. To perform this procedure, the vacuum chamber was carefully slid out of the coil assembly so that the breadboard could be removed. Optical posts were mounted to the top of the breadboard to support it while it was inverted. In this configuration, it was straightforward to direct beams into the coil assembly. In order to establish the position of the beams at the MOT, an IR card was first placed on the exposed bottom surface of the atom chip and ensured that both beams reached the card reasonably centered on the center chip spiral. Then the card was replaced with a thin mirror substituting for the silicon membrane mirror of the cell. Finally, the beams were aligned so that the reflections

from the chip mirror exited the coil assembly well overlapped with the corresponding input beams. When the breadboard and chamber were reinstalled, the beam alignment was typically good enough to observe a MOT with minimal adjustments.

When exploring this issue, it was discovered that it was not possible to align the beams centered on the atom chip and have the beams propagate through the coil assembly without clipping on mirrors. This issue is attributed to a small misalignment of the fixed mirrors in the assembly. To correct for it, the forked mount holding the two lower mirrors of the assembly was machined to replace the fixed mounts with adjustable kinematic mounts. This enables the beams to be better centered on the chip and also facilitated the adjustment of the beam alignment to optimize the MOT performance.

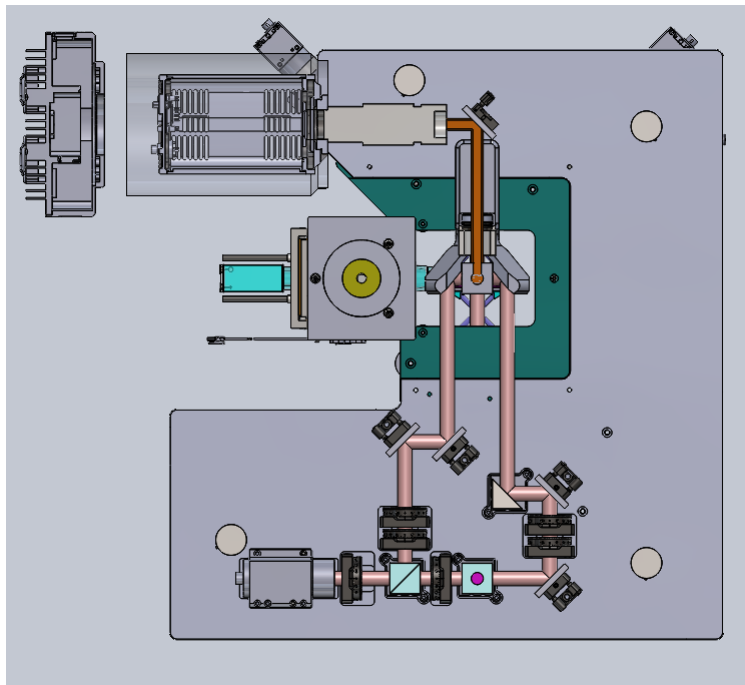
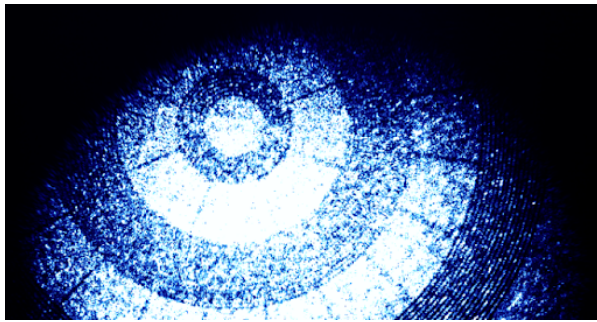
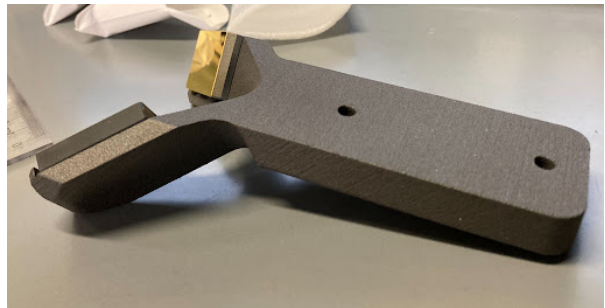


FIGURE 4.18: **Optics mounted on the bottom of the top breadboard.** 3D MOT beams in light pink, probe beam in orange.

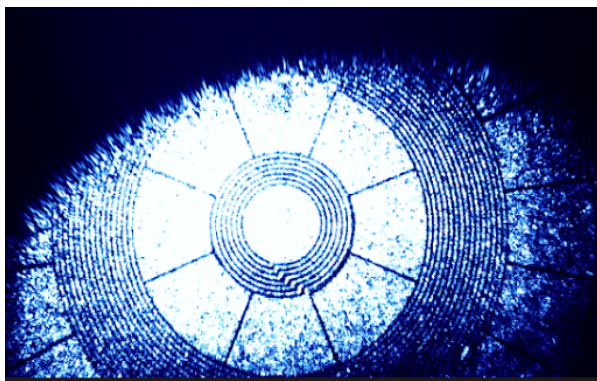


(A) Misalignment of MOT beams on chip with original forked mount. Here the chip is illuminated by the off-center MOT beams.

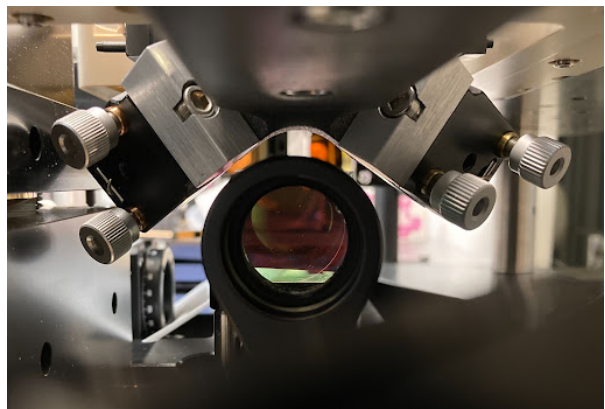


(B) Forked mirror mount with fixed mirrors.

FIGURE 4.19: Fixed mirror mount configuration.



(A) Improved alignment with new mount.



(B) New fold mirror mount, installed.

FIGURE 4.20: New adjustable mount configuration.

#### 4.2.4 MOT Monitoring

Although the improvements discussed above made the mirror MOT more reliable and easier to work with, the atom number remained too low, with a peak observation of  $10^7$  atoms and typical performance of about half of that. A persistent difficulty in addressing this problem was the lack of a usable real-time monitor of the atom number. In the lab-scale system, a monitor is implemented by imaging the MOT fluorescence onto a photodiode, which can then be tracked using a voltmeter or oscilloscope. The compact system was not designed with a fluorescence monitor, and we did not find a suitable way to implement one. Collection lenses placed on the upper breadboard had

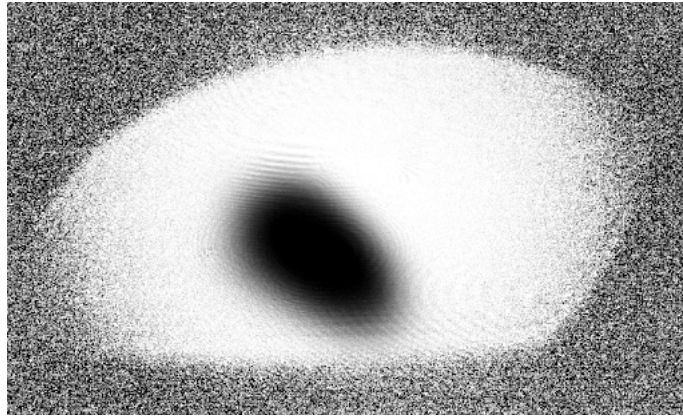


FIGURE 4.21: Absorption image of a 3D MOT.

low efficiency and suffered from a large amount of background light from scatter MOT beams and the pushing beam. A photodiode was added to the vertical imaging beam path using the secondary output of the probe beam splitter, but given the constraints involved, not enough fluorescence signal could be collected to provide a reliable signal. As an alternative to a photodiode, the bottom imaging camera was modified to provide a continuous video update, and a computer program developed to provide a real-time measure of the total light in the image. This monitor was useful, but it was rather slow and could not easily be synchronized to other experimental time controls. For instance, it could not be used to monitor the decay of the fluorescence after the push beam was turned off.

The MOT was quantitatively probed using absorption imaging with the vertical probe (see Fig. 4.21). However, this provides only a snapshot and requires significant image processing time, so it is ineffective to use when optimizing various parameters. Using the horizontal absorption imaging system was attempted as well, which would be useful for determining the distance from the MOT to the atom chip. Unfortunately, the small mirrors affixed to the vacuum chamber provided too limited a field of view for this purpose, and this problem was compounded by a small chip inadvertently

introduced into one mirror when removing the chamber from the coil assembly. Separately from the 3D MOT, the performance of the 2D MOT could not be evaluated. In principle the slow atomic beam could be detected with a transverse absorption probe, but the system lacked sufficient optical access for this measurement.

#### 4.2.5 Magnetic Trapping

Although there was an insufficient number of atoms in the mirror MOT, we attempted to load the atoms into the chip-based magnetic trap. However, the chip circuits were designed to be driven by the NGMS current amplifiers. These amplifiers were unavailable due to delivery delays, so instead a simple switching system using the standard current supplies was developed. The NGMS system will be more effective since it will allow the switching profiles to be controlled precisely to ensure the MOT fields are fully turned off before turning the chip fields on. In addition, it is also important to align the position of the chip trap with that of the MOT (as discussed in Chapter 3). For vertical alignment, this requires the horizontal imaging system which, as noted, did not work well.

When the chip trap loading was attempted, it was generally observed that the atoms were launched by the magnetic force away from the trap center. It is not clear why this happened but it would be expected if the chip fields turned on before the MOT bias fields turned off, since the non-zero bias fields would significantly displace the trap center from the expected location.

In conclusion, the compact system has many possible advantages over the lab-scale system and it could serve as a significant step towards an atom interferometer system suitable for use in a field environment. Unfortunately, it seems to have been too large of a step away from proven techniques and, despite working on it for over

an extensive period, there remain significant shortfalls. In the final chapter of this dissertation, a hybrid lab-scale experiment will be proposed that seeks to address these challenges, along with a discussion of the NGMS amplifiers, and technical improvements necessary to reach navigation and strategic grade gyroscope performance.

## Chapter 5

# Conclusion and Future Work

In this dissertation, two new apparatuses were described: a lab-scale system and a compact system. In the lab-scale system, an atom interferometer was successfully implemented and the stability characterized. In the compact system, the interferometer method bottlenecked at the MOT production stage of cooling and magnetically trapping atoms for BEC production. The major scientific and technical improvements of the compact system do not rely on producing a MOT with the exact production method for the compact system. In this chapter, plans will be outlined for a new hybrid apparatus. This apparatus will use methods that eliminate the bottleneck and allow further exploration using an atom chip and laser trapping techniques that reduce the size of the apparatus and improve the stability of the system. This apparatus will also use new custom current amplifiers from NGMS that will provide an additional tool to eliminate or reduce technical noise due to drifts in the TOP trap currents. Finally, a discussion of the stability of the lab-scale apparatus in the context of inertial navigation systems and an outline of the technical improvements needed to reach sensible sensitivity and stability benchmarks will be considered.

## 5.1 Hybrid Apparatus

As stated above, this apparatus will use existing parts from the compact system in order to implement an atom chip in air. At UVA, the laboratory has on hand the magnetic coil system consisting of an atom chip and bias coils, designed to operate in air with the compact vacuum cell (the same components from Chapter 4). Advantages of the chip-based system include faster evaporative cooling, simplified temperature regulation, the ability to test alternative chip designs, and the availability of extra coils to control trap anharmonicity. Further, the system is designed to minimize eddy currents from the TOP fields, making the magnetic performance more easily analyzed than in our present system.

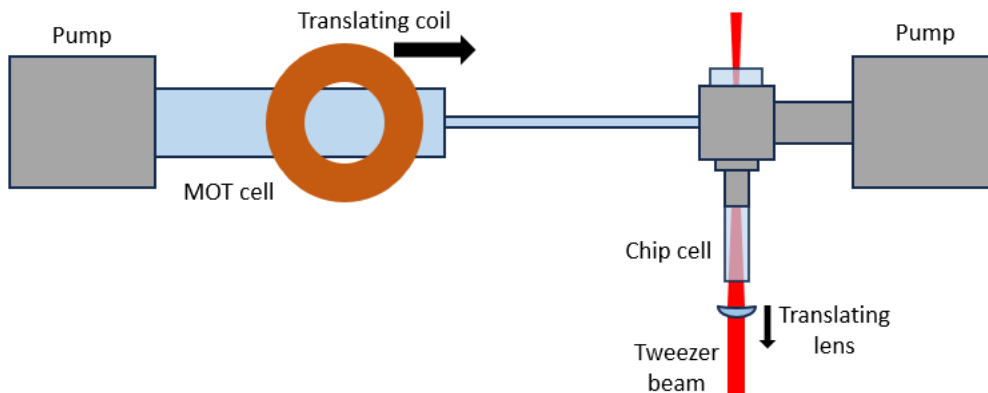


FIGURE 5.1: **Addition of chip cell to apparatus.** The large moving coil carries atoms from the MOT cell to the science chamber, from where an optical tweezer beam carries the atoms to the chip cell.

The four chip spirals (discussed in section 4.1.4) can facilitate loading MOT atoms into a trap produced by the chip and six bias coils. Presently, the plan is to load atoms onto the chip trap using an optical tweezer produced with an existing 30 W fiber laser. The cell will be mounted to the existing lab-scale apparatus (from Chapter 3) as seen in Fig. 5.1. This is designed to take advantage of the large atom number of the MOT and low vacuum pressure the apparatus provides. The optical trap will be loaded with

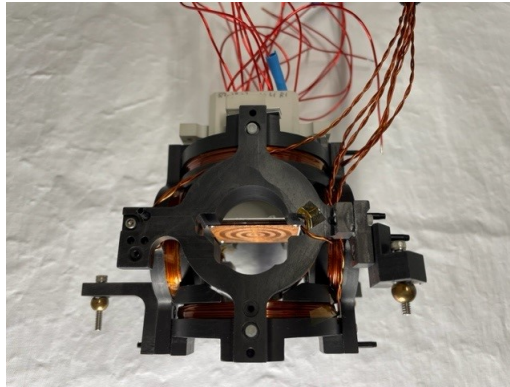


FIGURE 5.2: Coil structure showing six 5-cm diameter bias coils (black forms), the atom chip, and the chip mount (white block).

relatively warm atoms and then displaced approximately 15 cm using a focusing lens on a translation stage. Evaporative cooling to condensation will then be carried out on the chip in the small science cell.

In addition to reducing the evaporative cooling time, using the atom chip to speed up transfer from a tight TOP trap for evaporative cooling to a weak trap for interferometry will be explored. At present, this transfer is done quasi-adiabatically in about 20 s, but by using "shortcut-to-adiabaticity techniques" [51], the transfer could be achieved with good performance in less than 1 s. The low inductance of the chip will facilitate the short field pulses that may be required.

### 5.1.1 High Performance Amplifiers

If the observed phase noise in Chapter 3 is caused by trap imperfections coupled to the trap frequency fluctuations, then improving the trap frequency stability should reduce the phase noise. It is believed that the trap instability is caused by thermal fluctuations in the coil resistance. Currently, a feedback system in the current drivers is used to compensate for load variations, but the stabilization is not perfectly effective. Furthermore, the TOP trap fields oscillate at a frequency of 10 kHz and, if the feedback system

has bandwidth  $B_f$ , then the noise reduction for a signal at 10 kHz will be roughly  $10 \text{ kHz}/B_f$ . The drivers used currently have a noise reduction factor of roughly 0.1.

As part of the A-PhI project, NGMS developed and UVA constructed improved current drivers with a bandwidth of 1 MHz. The new current drivers offer several other advantages. The existing drivers rely on a tuned LC resonance circuit (see Fig. 3.9) to negate the inductive load of the trap coils. This works well but it means that the operating frequency cannot be changed without altering the circuit. The new amplifiers do not rely on any resonance behavior and can operate freely over their full bandwidth. One application of this is to vary the TOP frequency during the experiment. The apparatuses discussed here require a relatively large value of the TOP frequency during evaporative cooling while the atoms are confined in the tight trap, but after adiabatic expansion into a weak trap for interferometry, the TOP frequency could be reduced by a factor of 10 or more. This would in turn improve the current stabilization proportionately.

Another application of the wideband drivers is to use more complex waveforms for the TOP fields. Currently, the fields are sinusoidal, but by introducing additional frequency components, it is possible to alter the anharmonic terms in the trap potential. This could also reduce the interferometer phase noise, since the noise effect depends on a product of trap imperfections and current fluctuations. Through approaches such as these, several orders of magnitude improvement in the interferometer noise performance could be achieved.

## 5.2 Comparison with Modern Day Gyroscopes

Both the ARW and bias stability are important in navigation applications. A typical MEMS gyroscope has an ARW on the order of  $5 \text{ deg}/\sqrt{\text{hr}}$ , while a high-performance

optical gyroscope can achieve  $10^{-3}$  deg/ $\sqrt{\text{hr}}$ . Given the 4000 s measurement time required to take the data of Fig. 3.24, the lab-scale system exhibits an ARW of  $2^\circ/\sqrt{\text{hr}}$ . Potential improvements that can be considered include eliminating technical phase noise, decreasing the cycle time of the experiment from 100 to 5 s using atom-chip or optical trap techniques, increasing the single orbit area to  $1.5 \text{ mm}^2$ , and increasing the number of orbits to 10. All together, these would result in an ARW parameter of  $10^{-4}$  deg/ $\sqrt{\text{hr}}$ , which would be compelling for a compact sensor. Although these improvements are technically challenging, they are compatible with fundamental constraints including collisional losses and dephasing effects from interactions.

Sensor Type	ARW	Bias Stability
MEMS Gyro	$5^\circ/\sqrt{\text{hr}}$	$10\text{s}^\circ/\text{hr}$
UVA Gyro	$2^\circ/\sqrt{\text{hr}}$	$<4^\circ/\text{hr}$
Improvements	$10^{-4}^\circ/\sqrt{\text{hr}}$	$10^{-4}^\circ/\text{hr}$

FIGURE 5.3: **Phase Stability Comparison.** This table compares the typical MEMS gyroscope ARW and bias stability with the UVA gyroscope characterized in Chapter 3. The improvements row of the table represents the calculated ARW and bias stability if we can make the improvements to the system and method outlined in this section.

The bias stability in navigation applications is also important. It ranges from tens of degrees per hour for MEMS devices up to  $10^{-3}$  deg per hour for optical sensors. The observations in the lab-scale apparatus indicate a stability better than 4 deg/hr, but this is likely limited by short-term noise rather than long-term drift. Good stability is typically a feature of atomic devices, since atoms are intrinsically stable and highly effective laser stabilization techniques are available. However, these apparatuses are sensitive to the magnetic trapping frequencies and small drifts in these, coupled with a non-zero cross term,  $\gamma_{xy}$ , leads to phase noise similar to what we have observed.

In this section, feasible changes to the system have been proposed to help address this challenge. Returning to Eq. 3.11, if the parameter  $\gamma$  can be controlled at  $10^{-4}$  through the use of an atom chip to manage other anharmonic terms and long-term variations  $\frac{\delta\omega}{\omega}$  controlled at the  $10^{-6}$  level using better current amplifiers and coils in air, then the expected phase noise would be  $3 \times 10^{-5}$  rad for the single-orbit parameters demonstrated in Chapter 3, and  $5 \times 10^{-3}$  rad in the high-sensitivity system outlined above. The corresponding bias stability would be  $5 \times 10^{-4}$  and  $1 \times 10^{-4}$  deg/hr, respectively. These performance levels seem feasible, if challenging.

### 5.3 Summary

Atom-based sensors offer high performance sensitivity and stability for inertial measurements. These demonstrations have been done traditionally in a laboratory environment with large, complex systems unsuitable for environmental use. Over the past couple of decades, there has been major support at the intersection of academia, industry, and government to create atomic devices with low size, weight, and power consumption requirements that can serve as fieldable components of a future inertial navigation system. In the context of inertial navigation systems, the device that gains the most from more sensitivity and stability is the gyroscope due to the positioning error growing faster than that for an accelerometer. Small drifts in the gyroscope can mean large errors in calculating a user's position if the system is integrated over for long periods of time. This situation corresponds to being GPS denied for extended measurement times.

In this dissertation, a method for using a magnetically trapped BEC atom interferometer that was used previously to measure rotations on the order of the earth rotation rate was summarized. However, this proof of concept measurement was demonstrated

in an apparatus that was thermally unstable and not suitable for characterizing the long-term stability of the apparatus or method. The construction of a new lab-scale apparatus that addressed successfully the instabilities of the previous system was discussed. This new apparatus supported research that has led to improvements on the interferometer area and sensitivity but also allowed for a characterization of the stability of the system. A continuous, 26 hour Allan deviation measurement was performed, leading to a full characterization of the short-term noise in the system. An upper bound was placed on the system bias stability and can reasonably continue to be reduced, along with the ARW, if the interferometer area can be increased, more orbits achieved, the cycle time decreased drastically with the use of an atom chip or laser trapping techniques, and technical phase noise eliminated. This level of reduction would allow this method to achieve navigation and strategic grade sensitivity compatible with current gyroscopes.

In order for this method to continue to be considered for a future inertial navigation system, these technical improvements must be demonstrated in a compact form factor. A novel compact prototype system that uses an atom chip was characterized. However, there were many technical challenges and instabilities related to producing and monitoring a MOT. These were never fully overcome and the system produced a MOT of  $10^7$  atoms (for BEC production  $10^8$  or more atoms is needed). In this final chapter, a hybrid system was proposed. This system uses the lab-scale apparatus MOT production in combination with the compact system. This apparatus includes the technical upgrades needed for improving the stability and can test on-chip atom interferometer performance. This new system uses components that are already on-hand and introduces two new techniques using atom chip trapping and laser trapping. In addition to a new apparatus, the NGMS custom current amplifiers will be implemented. With this hybrid apparatus, it will be possible to implement several of the techniques needed to

achieve the stability and sensitivity required for a high performance INS.

# Bibliography

1. Groves, P. D. *Principles of GNSS, Inertial, and Multisensor Integrated Navigation Systems* (Artech House, 2013).
2. *Inertial Navigation Primer — vectornav.com*. [Accessed 30-01-2024].
3. *Scientific American Supplement*. EN. *Scientific American (1845-1908) XCVI*. Copyright - Copyright American Periodicals Series II Jun 29, 1907; Last updated - 2010-05-27, 531 (June 1907).
4. Albright, J. *Countering incorrect flight data in flight, part 1*. July 2022.
5. *Carousel Navigation Unit, Commercial Airline — airandspace.si.edu*. [Accessed 30-01-2024].
6. Fabio, A. *GPS And ADS-B Problems Cause Cancelled Flights — hackaday.com*. [Accessed 30-01-2024]. 2019.
7. Brewin, B. *University of Texas Team Hijacks \$80 Million Yacht With Cheap GPS Spoofing Gear — nextgov.com*. [Accessed 30-01-2024]. 2013.
8. GNSS, I. *FCC Fines Operator of GPS Jammer That Affected Newark Airport GBAS - Inside GNSS - Global Navigation Satellite Systems Engineering, Policy, and Design — insidegnss.com*. [Accessed 30-01-2024]. 2013.
9. Tino, G. M. & Kasevich, M. A. *Atom Interferometry* (IOS Press, Incorporated, 2014).
10. ArnoldReinhold. *Inertial navigation system - Wikipedia — en.wikipedia.org*. [Accessed 30-01-2024]. 2019.

11. [Inertial Navigation – Forty Years of Evolution](#). *GEC Review* **13**, 140–149 (3 1998).
12. Travagnin, M. [Cold Atom Interferometry for Inertial Navigation Sensors](#). 2020.
13. Landau, L. D. & Lifshitz, E. M. *Mechanics* 3rd ed. (Pergamon, 1960).
14. Sagnac, M. G. in *Comptes Rendus Hebdomadaires des Seances de l'Academie des Sciences* 708–710 (Elsevier, 1913).
15. Gill, W. A., Howard, I., Mazhar, I. & McKee, K. [A Review of MEMS Vibrating Gyroscopes and Their Reliability Issues in Harsh Environments](#). *Sensors* **22**. ISSN: 1424-8220 (2022).
16. Rogoway, T. [This Rare Photo Shows The Most Sensitive Part Of A Combat Aircraft — jalopnik.com](#). [Accessed 16-02-2024]. 2014.
17. Seyve, M. [iXblue officially presents Astrix NS performances at ASS GNC conference - iXblue — ixblue.com](#). [Accessed 16-02-2024].
18. Institution, S. [Housing, Hemispherical Resonator Gyroscope \(HRG\) | Smithsonian Institution — si.edu](#). [Accessed 16-02-2024].
19. Magnenat, S. [Gyroscope - Wikipedia — en.wikipedia.org](#). [Accessed 09-04-2024].
20. [Accessed 09-04-2024].
21. Horne, R. [A Cylindrically Symmetric, Magnetic Trap for Bose-Einstein Condensate Atom Interferometry Applications](#). PhD thesis (University of Virginia, 2015).
22. Arpornthip, T. [Characterizing the Potential Energy of an Atom Trap Through Tomographic Fluorescence Imaging](#). PhD thesis (University of Virginia, 2016).
23. Moan, E. [Rotation Sensing Using Atom Interferometry in a Magnetic Trap](#). PhD thesis (University of Virginia, 2020).
24. Wu, S., Wang, Y.-J., Diot, Q. & Prentiss, M. [Splitting matter waves using an optimized standing-wave light-pulse sequence](#). *Phys. Rev. A* **71**, 043602 (4 Apr. 2005).

25. Hughes, K. J., Deissler, B., Burke, J. H. T. & Sackett, C. A. [High-fidelity manipulation of a Bose-Einstein condensate using an optical standing wave](#). *Phys. Rev. A* **76**, 035601 (3 Sept. 2007).
26. Gustavson, T. L., Landragin, A. & Kasevich, M. A. [Rotation sensing with a dual atom-interferometer Sagnac gyroscope](#). *Classical and Quantum Gravity* **17**, 2385 (June 2000).
27. Gustavson, T. L. *Precision Rotation Sensing Using Atom Interferometry*. PhD thesis (Stanford University, 2000).
28. Durfee, D. S., Shaham, Y. K. & Kasevich, M. A. [Long-Term Stability of an Area-Reversible Atom-Interferometer Sagnac Gyroscope](#). *Phys. Rev. Lett.* **97**, 240801 (24 Dec. 2006).
29. Dunning, H. [Quantum sensor for a future navigation system tested aboard Royal Navy ship](#). 2023.
30. Kaushik, A. *et al.* [A cold atom gyroscope for inertial navigation](#). International Conference on Atomic Physics. 2022.
31. [Vector Atomic Validates Quantum Navigation Sensor at Sea — businesswire.com](#). 2023.
32. [Quantum Sensing Enters the DoD Landscape in First-of-a-Kind Demonstration — diu.mil](#). 2023.
33. Jo, G.-B. *et al.* [Long Phase Coherence Time and Number Squeezing of Two Bose-Einstein Condensates on an Atom Chip](#). *Phys. Rev. Lett.* **98**, 030407 (3 Jan. 2007).
34. Krzyzanowska, K. A., Ferreras, J., Ryu, C., Samson, E. C. & Boshier, M. G. [Matter-wave analog of a fiber-optic gyroscope](#). *Phys. Rev. A* **108**, 043305 (4 Oct. 2023).
35. Wu, S., Su, E. & Prentiss, M. [Demonstration of an Area-Enclosing Guided-Atom Interferometer for Rotation Sensing](#). *Phys. Rev. Lett.* **99**, 173201 (17 Oct. 2007).
36. Burke, J. H. T. & Sackett, C. A. [Scalable Bose-Einstein-condensate Sagnac interferometer in a linear trap](#). *Phys. Rev. A* **80**, 061603 (6 Dec. 2009).

37. Moan, E. R. *et al.* [Quantum Rotation Sensing with Dual Sagnac Interferometers in an Atom-Optical Waveguide](#). *Phys. Rev. Lett.* **124**, 120403 (12 Mar. 2020).
38. Qi, L. *et al.* [Magnetically guided Cesium interferometer for inertial sensing](#). *Applied Physics Letters* **110**, 153502. ISSN: 0003-6951. eprint: [https://pubs.aip.org/aip/apl/article-pdf/doi/10.1063/1.4980066/14496542/153502\\_1\\_online.pdf](https://pubs.aip.org/aip/apl/article-pdf/doi/10.1063/1.4980066/14496542/153502_1_online.pdf) (Apr. 2017).
39. Savoie, D. *et al.* [Interleaved atom interferometry for high-sensitivity inertial measurements](#). *Science Advances* **4**, eaau7948. eprint: <https://www.science.org/doi/pdf/10.1126/sciadv.aau7948> (2018).
40. Horne, R. A. & Sackett, C. A. [A cylindrically symmetric magnetic trap for compact Bose-Einstein condensate atom interferometer gyroscopes](#). *Review of Scientific Instruments* **88**, 013102. ISSN: 0034-6748 (Jan. 2017).
41. Collett, M. J. & Tee, G. J. [Ellipse fitting for interferometry. Part 1: static methods](#). *J. Opt. Soc. Am. A* **31**, 2573–2583 (Dec. 2014).
42. Horne, R. A. & Sackett, C. A. [A cylindrically symmetric magnetic trap for compact Bose-Einstein condensate atom interferometer gyroscopes](#). *Review of Scientific Instruments* **88**, 013102. ISSN: 0034-6748. eprint: [https://pubs.aip.org/aip/rsi/article-pdf/doi/10.1063/1.4973123/16147927/013102\\_1\\_online.pdf](https://pubs.aip.org/aip/rsi/article-pdf/doi/10.1063/1.4973123/16147927/013102_1_online.pdf) (Jan. 2017).
43. Lewandowski, H., Harber, D. & Whitaker, D. e. a. [Simplified System for Creating a Bose-Einstein Condensate](#). *Journal of Low Temperature Physics* **132**, 309–367 (2003).
44. Petrich, W., Anderson, M. H., Ensher, J. R. & Cornell, E. A. [Stable, Tightly Confining Magnetic Trap for Evaporative Cooling of Neutral Atoms](#). *Phys. Rev. Lett.* **74**, 3352–3355 (17 Apr. 1995).
45. Luo, Z., Moan, E. R. & Sackett, C. A. [Semiclassical Phase Analysis for a Trapped-Atom Sagnac Interferometer](#). *Atoms* **9**. ISSN: 2218-2004 (2021).

46. Baranowski, K. L. & Sackett, C. A. *A stable ac current source for magnetic traps*. *Journal of Physics B: Atomic, Molecular and Optical Physics* **39**, 2949 (June 2006).
47. Beydler, M. M., Moan, E. R., Luo, Z., Chu, Z. & Sackett, C. A. *Guided-wave Sagnac atom interferometer with large area and multiple orbits*. *AVS Quantum Science* **6**, 014401. ISSN: 2639-0213. eprint: [https://pubs.aip.org/avs/aqs/article-pdf/doi/10.1116/5.0173769/18292053/014401\\_1\\_5.0173769.pdf](https://pubs.aip.org/avs/aqs/article-pdf/doi/10.1116/5.0173769/18292053/014401_1_5.0173769.pdf) (Jan. 2024).
48. *CQ RuBECi System*. <https://www.infleqtion.com/rubeci>.
49. *CQ Photonically Integrated Cold Atom Source (PICAS) Datasheet*. <https://static1.squarespace.com/static/63de94661981f84d0e1b9fc5/t/6441631b8e99bc54ed5341ca/1682006813412/Photonically-Integrated-Cold-Atom-Source-PICAS-Datasheet+%281%29.pdf>.
50. Squires, M. B. *et al.* *Atom chips on direct bonded copper substrates*. *Review of Scientific Instruments* **82**, 023101. ISSN: 0034-6748. eprint: [https://pubs.aip.org/aip/rsi/article-pdf/doi/10.1063/1.3529434/15618765/023101\\_1\\_online.pdf](https://pubs.aip.org/aip/rsi/article-pdf/doi/10.1063/1.3529434/15618765/023101_1_online.pdf) (Feb. 2011).
51. Gaaloul, N. *et al.* *A space-based quantum gas laboratory at picokelvin energy scales*. *Nature Communications* **13**, 7889. ISSN: 2041-1723 (1 Dec. 2022).

## Appendix A

# Feedthrough Schematic

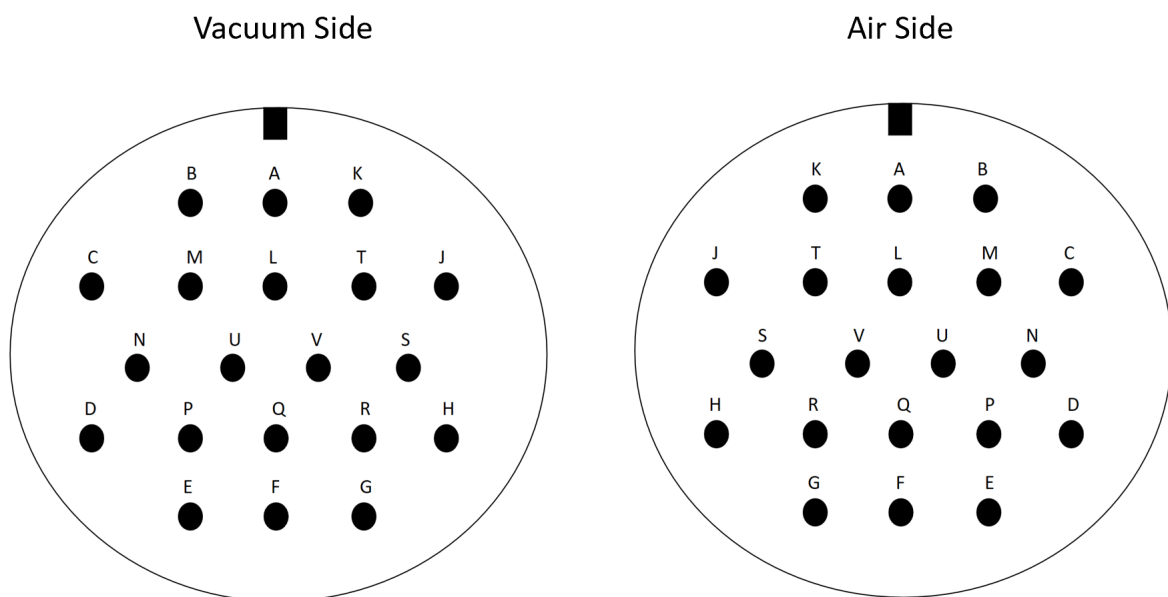


FIGURE A.1: Feedthrough schematic for the lab-scale system.

6 COILS + CHIP

PIN	LABEL	CURRENT
A	A+	I > 0 -> +Y
B	A-	
C	B+	I > 0 -> +Y
D	B-	
E	C+	I > 0 -> +X
F	C-	
G	D+	I > 0 -> +X
H	D-	
J	TOP+	I > 0 -> +Z
K	TOP-	
L	BOT+	I > 0 -> +Z
M	BOT-	
N	S1+	I > 0 -> +Z
P	S1-	
Q	S2+	I > 0 -> +Z
R	S2-	
S	S3+	I > 0 -> +Z
T	S3-	
U	W+	I > 0 -> X+Y
V	W-	

6 COILS ONLY

PIN	LABEL	CURRENT
A	A-	
B	A+	I > 0 -> +Y
C	B+	I > 0 -> +Y
D	B-	
E	C+	I > 0 -> +X
F	C-	
G	D+	I > 0 -> +X
H	D-	
J	TOP+	I > 0 -> +Z
K	TOP-	
L	BOT+	I > 0 -> +Z
M	BOT-	

FIGURE A.2: A list of the coils and chip current directions with feedthrough and experimental labeling. The left table is for the lab-scale apparatus when a chip was tested in vacuum. The right table is after the chip was removed.

## Appendix B

### Bias Coil Information

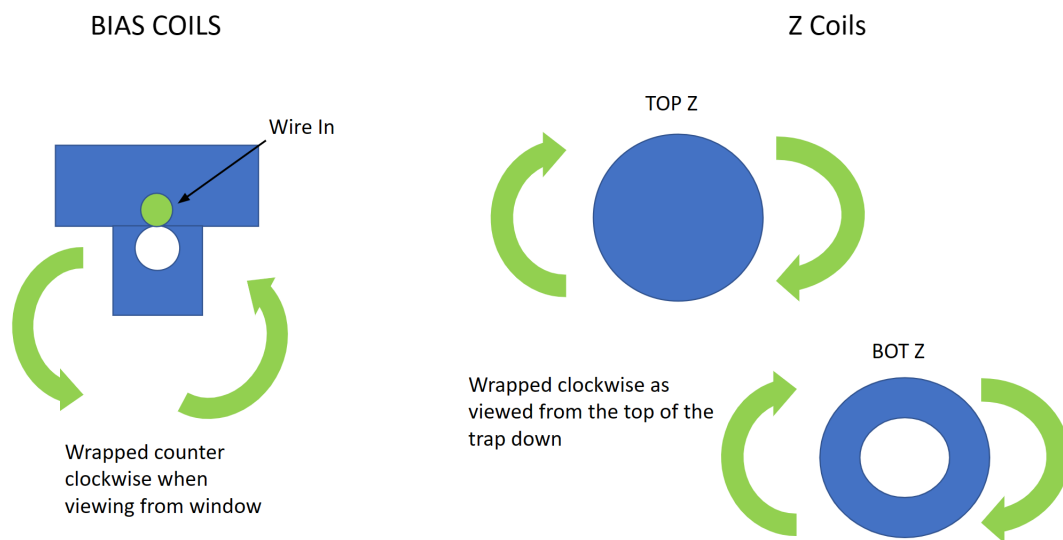


FIGURE B.1: Cartoon of coil winding directions pre-vacuum bake in the lab-scale apparatus science chamber.

Calculations:				
Parameter:	Z coils	X coils	Y coils	Units
r_inner =	13.05	8	8	mm
r_outer =	17.15	20.5	20.5	mm
s_inner =	11.3	23.15	23.15	mm
s_outer =	16.1	29.55	29.55	mm
N =	26	64	63	turns
AWG =	22	20	20	
conductor diameter =	0.59	0.81	0.81	mm
insulation diameter =	0.86	1.04	1.04	mm
Length =	2.47	5.73	5.64	m
Copper resistivity =	1.68E-05	1.68E-05	1.68E-05	Ohm-mm
Calculated resistance =	0.15	0.19	0.18	Ohm
Solenoid inductance =	51	267	259	uH
Loop inductance =	84	395	383	uH
Winding fill factor =	77.4	68	66.9	%
Copper fill factor =	36.1	41.5	40.9	%

FIGURE B.2: Calculated resistance and inductance with measured parameters.

Measurments:							
Coil:	A	B	C	D	Zt	Zb	Units
resistance (dc) =	0.238	0.241	0.231	0.229	0.243	0.229	Ohm
inductance (10 kHz) =	105.2	110.1	108.4	106.8	25.5	31.9	uH

FIGURE B.3: Measured coil resistance and inductance. A, B, C, and D are the horizontal bias coil labeled individually.

More Measurements:	R (Ohms)
Straight 22 Kapton Wire:	0.149
Coiled 22 Kapton Wire:	0.149

FIGURE B.4: Measured coil resistance for straight Kapton wire vs. coiled Kapton wire of the same length.